Technical University of Denmark

DTU

# deNOx catalysts for biomass combustion

**Kristensen, Steffen Buus; Riisager, Anders; Fehrmann, Rasmus; Nørklit Jensen, Jørgen**

*Publication date:*
2013

*Document Version*
Publisher's PDF, also known as Version of record

[Link back to DTU Orbit](#)

**DTU Library**
Technical Information Center of Denmark

# deNO$_x$ catalysts for biomass combustion

Ph.D. Thesis
Steffen Buus Kristensen
April 2013

*Cover illustrations:*
Top left: Aqueous solutions of vanadium in the four oxidation states +2, +3, +4 and +5
Lower right: From the left, powdered 20 wt.% V$_2$O$_5$/TiO$_2$ catalyst, extruded catalyst comprising 20 wt.% sepiolite and nano-catalyst, a plate composite catalyst.
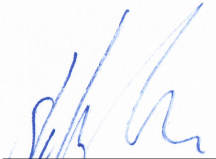
# Preface

This thesis has been submitted in candidacy for the Ph.D. degree in chemistry from the Technical University of Denmark (DTU). The work summarised herein was mostly carried out at the Department of Chemistry in the Centre for Catalysis and Sustainable Chemistry (CSC), from July 2009 to February 2013 under the joint supervision of Assoc. Prof. Anders Riisager, Jørgen Nørklit Jensen and Prof. Rasmus Fehrmann. This project was financed through the industrial Ph.D. programme via the Danish Agency for Science, Technology and Innovation with DONG Energy and Vattenfall.

First and foremost I would like to thank my family, for putting up with me in the busy times during the Ph.D.

I would further like to thank my three supervisors for the opportunity and the collaboration during the thesis. Then I would like to thank Andreas Jonas Kunov-Kruse for productive collaboration and many interesting discussions. I am also very grateful for the lab-collaboration and feedback from Johannes Due-Hansen and Søren Birk Rasmussen at CSC.

Thanks to Bodil Holten (DTU Chemistry) and Prof. Soghomon Boghosian (University of Patras, Greece) for sample analysis, surface area measurements and Raman respectively.

Finally I would like to thank all the people at the Centre for Catalysis and Sustainable Chemistry.

Steffen Buus Kristensen
Lyngby, April 15, 2013

# Abstract

The present thesis revolves around the challenges involved in removal of nitrogen oxides in biomass fired power plants. Nitrogen oxides are unwanted byproducts formed to some extent during almost any combustion. In coal fired plants these byproducts are removed by selective catalytic reduction, however the alkali in biomass complicate matters. Alkali in biomass severely deactivates the catalyst used for the selective catalytic reduction in matter of weeks, hence a more alkali resistant catalyst is needed.

In the thesis a solution to the problem is presented, the nano particle deNO$_x$ catalyst. Through the thesis the one-pot sol-gel synthesis of this nano particle catalyst, have been optimised by evaluation of each synthesis step. Resulting in a highly active catalyst comprising amorphous vanadia on a high surface area crystalline anatase carrier. Due to the high surface area, loadings of 20 wt.% vanadia could be obtained without exceeding the $V_2O_5$ monolayer coverage. Explaining the very high activity corresponding to a factor of 2, compared to an industrial reference. Even at high vanadia loadings the catalyst did not show any sign of increased $SO_2$ oxidation, compared with a low vanadia industrial reference catalyst. Furthermore long-term activity measurements at normal operating temperature revealed that the catalyst did not display any sign of deactivation.

The catalyst showed very high resistance towards potassium poisoning maintaining a 16 times higher activity than the equally poisoned industrial reference catalyst, after impregnation of $225 \, ^{\mu\text{mole potassium}}/_{\text{g of catalyst}}$.

A catalyst plate was synthesised using 20 wt.% sepiolite mixed with nano catalyst, supported by a $SiO_2$-fibre mesh. Realistic potassium poisoning was performed on the catalyst plate, by exposure in a potassium aerosol for 632 hours at 350 °C. Owing to physical blocking of potassium by sepiolite fibres the composite catalyst showed a further increase in potassium resistance compared with the unsupported catalyst.

Finally a refined mechanism was proposed for the nano particle SCR catalyst explaining in-situ FTIR observation done on the system. Most importantly it indicated that the V=O bond did not break during the SCR reaction, suggesting that another oxygen is responsible for the activity of the active vanadia site.

# Dansk Resumé

Denne afhandling omhandler de udfordringer, der er involveret i fjernelse af nitrogenoxider på biomassefyrede kraftværker. Nitrogenoxider er uønskede biprodukter, der dannes under næsten enhver forbrænding. I kulfyrede anlæg fjernes disse biprodukter ved selektiv katalytisk reduktion, men alkali i biomassen komplicerer denne proces. I løbet af få uger deaktiveres katalysatoren der bruges i selektiv katalytisk reduktion af den alkali der er bundet i biomassen, derfor er en mere alkali resistent katalysator en nødvendighed.

Nano partikel deNO$_x$ katalysatoren er en mulig løsning på problemet. Igennem denne afhandling er sol-gel syntesen af nano partikel katalysatoren blevet optimeret og hvert syntesetrin evalueret. Dette har resulteret i en meget aktiv katalysator, der består af amorft vanadiumoxid på en højt overflade krystallinsk anatas bærer. På grund af bærerens høje overfladeareal kunne 20 wt.% vanadiumoxid opnås uden at V$_2$O$_5$ monolaget blev overskredet. Dette forklarer den meget høje aktivitet, svarende til en faktor 2 i forhold til en industriel reference katalysator. Selv med den høje mængde vanadiumoxid på katalysatoren var der ingen tegn på øget SO$_2$ oxidation, sammenlignet med en industriel katalysator med lavt vanadiumoxid indhold. Langtids-aktivitetsmålinger udført ved normal drifttemperatur, viste ingen tegn på termisk deaktivering af katalysatoren.

Katalysatoren udviste også meget høj resistens mod kalium forgiftning, efter imprægnering af 225 $^{\mu\text{mol kalium}}/_{\text{g katalysator}}$ kunne nano partikel katalysatoren opretholde en 16 gange højere aktivitet end den lige så forgiftede industrielle katalysator.

En katalysator plade blev fremstillet af 20 wt.% sepiolit, blandet med nano katalysatoren på et SiO$_2$-fiber support. Denne katalysator plade blev udsat for en mere realistisk kalium deaktivering, ved at eksponere den i en kalium holdig aerosol røggas i 632 timer ved 350 °C. Grundet sepiolit fibrens fysiske blokering af kalium, udviste katalysatoren yderligere forøgelse af kalium resistens.

Til slut blev en fornyet mekanisme foreslået for nano partiklen SCR-katalysatoren, som forklarer in-situ FTIR observationer udført på systemet. Den vigtigste observation var at V=O bindingen ikke blev brudt under SCR reaktionen, hvilket antyder at et andet oxygen er ansvarlig for aktiviteten af det aktive vanadiumoxid site.

# Contents

**1**

## Nitrogen oxides

In this chapter the environmental concerns of nitrogen oxides will be discussed, and some of the possible solutions to the emission problems will be described. The formation process of nitrogen oxides are also explained, and the possible mechanisms to lower the emitted amount of $NO_x$ are highlighted. Finally the concept of non-catalytic removal of nitrogen oxides will be described in detail.

## 1.1. Nitrogen oxides and the sources

Nitrogen oxides or $NO_x$ are a group of atmospheric pollutants, comprising seven nitrogen oxides, NO, $NO_2$, $NO_3$, $N_2O$, $N_2O_3$, $N_2O_4$ and $N_2O_5$. But emissions consist mainly of NO and $NO_2$, with NO as the major $NO_x$ specie representing 90-95% of the total amount of emitted nitrogen oxides [2]. The focus will primarily be on those two species.

The major source of emitted $NO_x$ is from combustion of fossil fuels and burning of biomass. Industrial and domestic burning of these fuels are important stationary sources of $NO_x$, but also combustion of fossil fuels in vehicles, airplanes and ships are great contributors to the total amount of emitted $NO_x$. There are also natural processes contributing to the $NO_x$ emissions such as fixation by lightning, volcanic activities, the oxidation of ammonia in the troposphere and ammonia oxidation from the decomposition of proteins. However man-made $NO_x$ emissions are the major source, responsible for three quarters of the total amount released into the atmosphere [2,3].

Burning of fossil fuels for transportation is responsible for the major part of the man-made nitrogen oxides, an estimated 45-60% of the total amount produced in industrialised countries. Stationary sources such as burning of coal, oil or biomass in power plants are the second

**Table 1.1.:** *Composition of flue gas from coal-fired power plants* [1].

| NO (ppm) | $NO_2$ (ppm) | $SO_2$ (ppm) | $SO_3$ (ppm) | $H_2O$ (%) | $O_2$ (%) | $CO_2$ (%) | Dust(low) ($\frac{mg}{m^3}$) | Dust(high) ($\frac{g}{m^3}$) |
|---|---|---|---|---|---|---|---|---|
| 400-700 | 2-5 | 500-2000 | 2-20 | 6-8 | 4-5 | 10-12 | 5-20 | 10-20 |

largest contributor. The average flue gas composition from a coal fired plan can be seen in Table 1.1, illustrating the high contents of $NO_x$ in a untreated flue gas.

Nitrogen oxides are major atmospheric pollutants, responsible for acid rain and town smog, and not at least depletion of the ozone in the ozone-layer. NO and $NO_2$ react with ozone in the troposphere and stratosphere removing the ozone-layer. These reactions are largely responsible for the ozone decline, resulting in increased radiation of UV-C and UV-B causing DNA damage in living tissues in both plants and animals [2–4].

## 1.2. Legislations

Due to the ecological and health hazards of nitrogen oxides, many regulations have been proposed and some adopted to control $NO_x$ emissions. There is a wide variety of different regulations among many countries, which differ in type and extent.

In November 1999 the Gothenburg protocol was established, hereby setting emission ceilings for four pollutants in 2010: sulphur, $NO_x$, VOCs[a] and ammonia. Canada, USA and 29 European countries signed this protocol and each of the countries has set goals. Europe's $NO_x$ emissions should be cut by at least 41% compared to a 1990 level within 2010 [3,5].

To reach this goal the government in Denmark has increased the $NO_x$ tax from 5 Dkr pr. kg $NO_x$ to a whopping 25 Dkr pr. kg, although only for stationary $NO_x$ sources [6]. This current development has increased the incitement for cleaning the flue gas even more, decreasing the emitted $NO_x$ to the lowest possible amount.

In 2007 the protocol was reviewed and it was concluded at a meeting in Geneva 2012 that more stringent emission reduction was necessary and commitments for 2020 was agreed.

Furthermore the current energy policies in Denmark regarding $CO_2$ neutral fuels requires new catalysts to be developed. This is due to the deactivation of the current catalysts for $NO_x$ cleaning in Biomass boilers [7]. This problem will be discussed later in detail.

---

[a]VOC volatile organic compounds
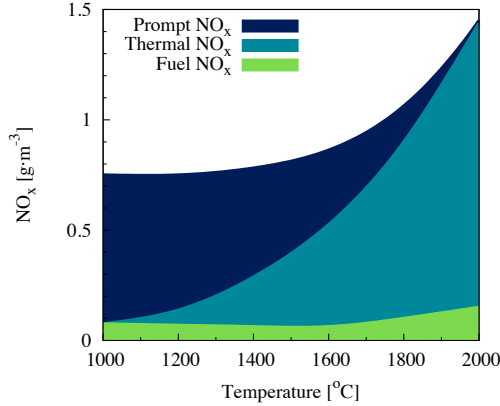
**Figure 1.1.:** *The temperature dependence of the three sources of NO$_x$ for a coal-fired furnace, thermal, fuel and prompt NO$_x$. Adapted from Bosch et al.* [2].

## 1.3. Formation of NO$_x$

Nitrogen oxides formed by combustion in power plants can be divided into three types, *thermal* NO$_x$, *fuel* NO$_x$ and *prompt* NO$_x$, categorised depending on the formation mechanism.

The first type of nitrogen oxides are *thermal* NO$_x$, this type are formed by oxidation of atmospheric nitrogen at very high temperatures during combustion according to the simple equation, see Equation (1.1).

$$N_2 + O_2 \longrightarrow 2\,NO \tag{1.1}$$

The rate of this reaction is highly dependent on temperature, hence *thermal* NO$_x$ is only observed in large quantities at high temperatures, see Figure 1.1. But due to the high temperatures of industrial boilers this type of NO$_x$ is responsible for the largest emissions [2–4].

*Fuel* NO$_x$ is formed from the gas-phase oxidation of volatilised fuel nitrogen. The amount of *fuel* NO$_x$ is contrary to *thermal* NO$_x$ independent of combustion temperature and is likewise insensitive to the nature of the organic nitrogen compound in the fuel, see Figure 1.1. A mechanism has been proposed for the formation of fuel NO$_x$, where nitrogen compounds form a complex that can be attacked by OH-radicals and NO molecules forming either NO or N$_2$ respectively. A reducing environment can suppress formation of NO by this reaction, where the OH-radicals will react with hydrogen forming water instead [2].

The third type of nitrogen oxides are called *Prompt* NO$_x$ and is formed by the reaction of

hydrocarbon fragments with atmospheric nitrogen forming HCN intermediates, that can subsequently oxidise to NO in the lean zone of the flame. The temperature dependence of *prompt* $NO_x$ is the opposite as for *thermal* $NO_x$, i.e. it is only formed at low temperatures and fuel rich flames, see Figure 1.1 on the previous page.

## 1.4. Non-catalytic removal and other control technologies

Many types of $NO_x$ emission control technologies are available overall these technologies can be divided into two main groups. A group of combustion control measures called clean techniques, and a group of post-combustion control measures called clean-up techniques or flue-gas treatment.

All the clean techniques involve changes in the combustion environment, such as controlling the nitrogen content of the fuel, modification of the burner and oxygen content in the combustion chamber. It is also the most cost-effective and energy-efficient technology; hence the clean technologies are always the first approach to control $NO_x$ emissions. The major objectives for combustion control in order to reduce the $NO_x$ emissions are, decreasing of the oxygen level at peak temperatures, reducing the peak temperature and the residence time in the combustion zone (lowering the *thermal* and *prompt* $NO_x$). Further a reduction of fuel nitrogen can be realised by choosing better low nitrogen containing fuels[8].

One way of achieving some of these objectives is to lower the flame temperature either by FGR (Flue-gas Recirculation) or injection of steam or water lowering $NO_x$ by 20-50%. A reduction of available oxygen can also reduce the amount of emitted $NO_x$, but the downside is CO formation, low flame stability and smoke. Much more effective is the staged combustion burners also called low-$NO_x$ Burners, where a specially designed burner is used with an oxygen- or fuel-deficient core flame. Remaining air or fuel is introduced close to the burner in a cylindrical zone around the core flame. Using this technique multiple stages are formed, e.g. there are four injection zones one primary with a fuel-rich air/fuel mixture, next a secondary air and then a tertiary air injection. Forming three different zones one fuel rich, one with a 1:1 ratio and one fuel-deficient zone, reducing the $NO_x$ emissions by 25-60%[8].

However it is not possible to prevent the formation of $NO_x$, for this reason some after treatment is a necessity. Direct decomposition of $NO_x$ would be the dream reaction, where $NO_x$ is decomposed into $N_2$ and $O_2$ over a catalyst. But all studies have showed that the direct decomposition of NO, is not effective enough and requires very high temperatures above 800 °C[9–11]. Other catalyst systems have been developed that are active at as low temperatures as 300 °C[12,13], but no catalysts to the authors knowledge has been developed that are efficient enough for industrial applications.

The remaining post-combustion techniques can be divided into two groups catalytic and non-

catalytic. The most used non-catalytic technique is the selective non-catalytic reduction (SNCR). Here a selective reduction of NO, with a reduction agent such as $NH_3$, urea or cyanuric acid [14] is used. The reduction agent is introduced into the upper part of the boiler, where the temperature is 850-1050 °C C. The main reactions are:

$$6\,NO + 4\,NH_3 \longrightarrow 5\,N_2 + 6\,H_2O \tag{1.2}$$

$$6\,NO_2 + 8\,NH_3 \longrightarrow 7\,N_2 + 12\,H_2O \tag{1.3}$$
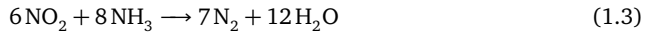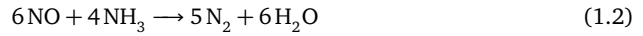
Reduction levels up to 50% can be achieved, but there are major drawbacks. A narrow temperature range and problems with ammonia slip can occur and ammonium salt formation can cause plugging and corrosion [8,14]. A much more effective alternative is the catalytic post-combustion process, this process will be discussed later in detail, see Chapter 2 on page 9. Usually both the combustion and post-combustion processes are used together to obtain lowest emissions of $NO_x$.

# 2

## Selective catalytic reduction (SCR)

This chapter is an introduction to the most widely used post-combustion process, selective catalytic reduction (SCR). It will be described in terms of a literature review of the typical types of commercial catalysts. Furthermore the currently most accepted SCR reaction mechanisms will be discussed. Finally the more recent challenge of biomass combustion and the resulting deactivation of the catalyst will be investigated in another literature review. Key conclusions of each section will be used in the discussions in chapter 6 and 7.

## 2.1. Introduction

As described in the previous chapter, the direct decomposition of $NO_x$ over a catalyst is very slow and a sufficiently effective catalyst is still to be discovered. Consequently in order to make the decomposition of $NO_x$ effective enough a reduction agent has to be used. The most commonly used reduction agent used for removal of $NO_x$ is ammonia, but also other agents such as urea, CO, $H_2$, $CH_4$ or hydrocarbons can be used. The catalytic process where nitrogen oxides are reduced selectively by ammonia over a catalyst is called Selective Catalytic Reduction (SCR). This process lowers the reaction temperature from 850-1050 °C of SNCR to 150-450 °C, making it possible to convert $NO_x$ in several different stages in the power plant.

The SCR catalyst unit can be implemented at three different stages, called clean-gas, high-dust or low-dust modification. Clean-gas configuration or end-of-pipe is a solution where the catalyst is placed as the last step after the FGD (Flue-Gas Desulphurisation unit) and the ESP (Electro-Static Filter). Catalysts used in this configuration have a long lifetime, because there are no deactivation effects from $SO_3$, $SO_2$, HCl and other more or less poisonous species and
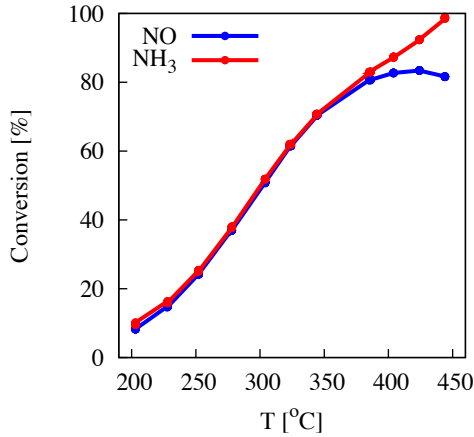
**Figure 2.1.:** *A activity measurement of SCR catalyst, Conversion of NO is marked with* **blue** *and conversion of NH$_3$ is marked with* **red**.

the flue gas are nearly dust free. The disadvantage of low-dust configuration is the energy loss when the flue gases are preheated after the FGD, before the SCR unit. This is avoided in the low-dust configuration, where the SCR unit is placed just after a hot ESP. The drawback of this placement, is that the hot ESP is very expensive and deposition of $NH_4HSO_4$ on the Air Pre-Heater (APH) after the catalyst is a common problem. The last position and by far predominantly used is the high dust configuration, where the SCR unit is placed just after the boiler. This position is preferred because of the cleaning effect of fly ash attracting $NH_4HSO_4$ preventing deposition on the APH unit, but in this configuration the SCR unit has a considerable shorter lifetime[8,15].

Catalysts for the SCR reaction are numerous, many different catalyst compositions have been tested for this reaction and many are active but only a few different systems are effective enough to be applied industrially[15]. The most widely used catalysts will be mentioned later in the next section. The main reactions for the SCR process are identically regardless of the catalyst, see Reaction scheme (2.1) and (2.2).

$$4\,NO + 4\,NH_3 + O_2 \longrightarrow 4\,N_2 + 6\,H_2O \tag{2.1}$$

$$2\,NO + 2\,NO_2 + 4\,NH_3 \longrightarrow 4\,N_2 + 6\,H_2O \tag{2.2}$$
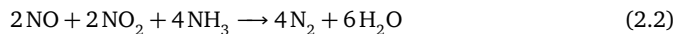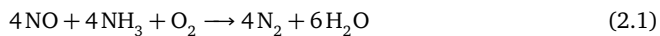
Reaction scheme (2.1) is describing the normal SCR reaction, where NO is reacting with $NH_3$ in the presence of $O_2$. In general, authors agree that under typical SCR conditions, with $NH_3/NO$ near 1, few percent oxygen and temperature below 400 °C the above reaction scheme accounts for the overall stoichiometry[8,16,17]. To enhance the reaction rate, $NO_2$ can be introduced by an oxidation catalyst e.g. a platinum catalyst or by addition of urea. This results in a faster

reaction rate due to the *fast SCR* reaction, see Reaction scheme (2.2) [4,18,19].

But also unwanted secondary reactions take place as a result of the type of catalyst, temperature, oxygen content and $SO_2$ content.

$$4\,NH_3 + 3\,O_2 \longrightarrow 2\,N_2 + 6\,H_2O \tag{2.3}$$

$$4\,NH_3 + 5\,O_2 \longrightarrow 4\,NO + 6\,H_2O \tag{2.4}$$
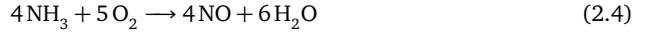
One of the unwanted secondary reactions is the oxidation of $NH_3$, this reaction can take place according to several reaction schemes, one of them is the simple oxidation of $NH_3$ using $O_2$ see Reaction scheme (2.3) and (2.4). This reaction is responsible for the decrease in activity at high temperatures, where the oxidation of $NH_3$ becomes more and more pronounced competing with the SCR reaction, see Figure 2.1 on the preceding page.

$$2\,SO_2 + O_2 \longrightarrow 2\,SO_3 \tag{2.5}$$

$$NH_3 + SO_3 + H_2O \longrightarrow NH_4HSO_4 \tag{2.6}$$

$$SO_3 + H_2O \longrightarrow H_2SO_4 \tag{2.7}$$
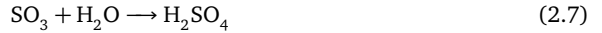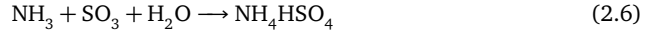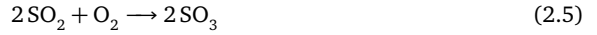
Another unwanted reaction is the oxidation of $SO_2$, which in turn reacts with $NH_3$ forming solid $NH_4HSO_4$ or with water forming $H_2SO_4$, see reaction schemes (2.5-2.7). $NH_4HSO_4$ and $H_2SO_4$ are both corrosive and very undesirable products, causing fouling and corrosion [4,8]. Hence, it is very important to have an effective catalyst for the SCR reaction that are not oxidising $NH_3$ or $SO_2$.

## 2.2. Reaction Kinetics

NO reaction rate for the SCR process, see Reaction scheme (2.1), depends on the concentrations of the reactants, NO, $NH_3$ and $O_2$, but also the concentration of $H_2O$. The reaction rate can be expressed as a power kinetic equation, where the reaction order with respect to the reactants can be found empirically, see Equation (2.8).

$$r_{NO} = k_c C_{NO}^{\alpha} C_{NH_3}^{\beta} C_{O_2}^{\gamma} C_{H_2O}^{\delta} \tag{2.8}$$

According to Inomata et al. and Wong et al. [20,21] the reaction order of $O_2$ is 0 ($\gamma$=0) when oxygen is in excess according the SCR reaction equation. Working in excess of $O_2$ and in absence of water vapour or with water contents above 5% the rate dependencies can be neglected of $O_2$ and $H_2O$ [20,21]. Furthermore working in excess of $NH_3$ reduces the above rate

equation to, see Equation (2.9).

$$r_{NO} = k_c C_{NO}^{\alpha} \tag{2.9}$$

The reaction order with respect to NO ($\alpha$) has been measured by many authors to be one on $V_2O_5/TiO_2$ catalysts [20–23]. Later this rate equation can be used to express a pseudo-first-order rate equation, which in turn can be applied to evaluate the activity regardless of mass, flow and type of catalyst, see Section 3.2.1 on page 29 for further information.

## 2.3. SCR catalyst systems

As earlier mentioned many different catalysts can be used for the SCR reaction and some have been proven very effective, in this section the most common catalysts will be reviewed.

Supported noble metals or metal oxides and zeolites with an active metal are the most common and active catalyst systems developed for commercial SCR [8,16].

Noble metal catalysts were developed in the 1970's as exhaust catalysts, these catalysts are very active in SCR, but unfortunately simultaneously very effective $NH_3$ oxidation catalysts. This makes the supported noble metal catalysts unsuitable for industrial application and they were soon replaced by supported metal oxide catalysts [17]. Of the many different metal oxide catalyst systems, those based on vanadia supported on titania in anatase form have been found most active.

Deposition of metal oxides on supports gives the advantage of a larger surface area and higher catalytic activities the latter due to support-metal oxide interactions. Regarding undesired reactions the support also plays a major role, e.g. supports containing $Al_2O_3$ react strongly with $SO_2$ forming metal sulphates deactivating the catalyst. $TiO_2$ has the advantage that it is only weakly and reversibly sulphated, hence not deactivated. Furthermore the weak sulphation is increasing the activity of the supported catalyst, hereby increasing the potassium resistance [16].

Vanadia is responsible for the SCR activity of a vanadia supported anatase catalyst, as well as the undesired oxidation of $SO_2$ as described earlier. The ability to oxidise $SO_2$, the $NH_3$ oxidation and the SCR reaction is dependent on the nature of vanadia. Wachs et al. [24] investigated the optimal loading of vanadia on anatase, and found that the optimal loading was achieved at one monolayer vanadia dispersed on the titania surface. At low loadings with less than one monolayer of vanadia on the surface, the isolated and monomeric vanadia species dominate. With increasing loading dimeric and polymeric species are formed and at even higher loadings above the monolayer coverage crystalline vanadia will dominate [25], the different vanadium species are depicted in Figure 2.2 on the next page.

Also the activity pr. vanadium atom will change with increasing coverage this is seen, as poly-
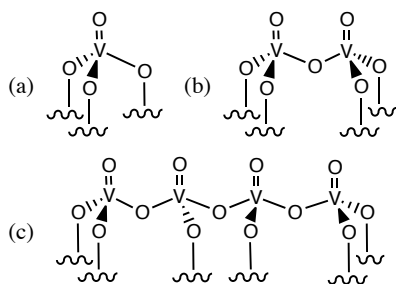
**Figure 2.2.:** *Schematic representation of (a) monomeric (b) dimeric and (c) polymeric species of vanadia. Adapted from Busca et al.* [16] *and Wachs et al.* [24]
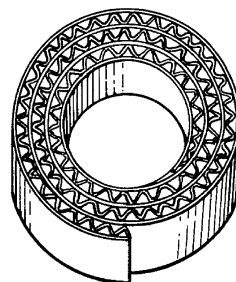


**Figure 2.3.:** *Schematic representation of corrugated monolith adapted from Avila et al.* [26].

meric species are 10 times more active than monomeric. But more important the selectivity of NO oxidation decreases dramatically when crystalline vanadia is observed on the surface [27]. As a result catalysts containing vanadia should always have a loading corresponding to just below a monolayer. The amount of vanadia on commercial catalysts is often very low this is done to minimise the oxidation of $SO_2$ and maximise the selectivity [28].

Commercial catalysts are not only containing vanadia and titania, but also different promoters such as tungsten and molybdenum oxides. These oxides are added to stabilise the metastable anatase crystal phase of $TiO_2$. In addition this stabilisation is important for the $V_2O_5/TiO_2$ system, due to a destabilisation effect of $V_2O_5$ on anatase [29]. However Gao et al. [30] showed that $Fe_2O_3$ could be used as a promoter with the $V_2O_5-WO_3-TiO_2$ catalyst system increasing the activity.

Different catalysts based on zeolites have proven to be very active, already in 1991 Sato et al. showed that a copper exchanged ZSM-5 zeolite exhibited great potential for hydrocarbon SCR [31]. Recently other zeolites have been tested for SCR activity using ammonia as a reductant, especially the copper doped zeolite mineral mordenite showed high potential for high temperature applications and biomass firing due to high potassium resistance [32].

Other advantages of the copper or iron-exchanged zeolites are the high selectivity and higher temperature stability of the exchanged metal compared to the volatile vanadium species above 650 °C [33]. However as mentioned earlier catalysts with alumina supports suffer from severe $SO_2$ deactivation, due to irreversible sulphation leading to severe deactivation even at low $SO_2$ concentrations.

Catalysts based on $ZrO_2$ are getting more popular as well, because of the strong acidity. After sulphation of the carrier [34,35]. Kustov et al. showed that the acidity of the support is very important for the potassium resistance, after sulphation of different supports and tests of potassium deactivation they showed that by using an acidic carrier the potassium resistance could be enhanced noticeably [7].

But even with the recent developments, the most widely type of catalyst used is $V_2O_5-WO_3-TiO_2$ systems, because of the high activity of this system.

Commercial catalysts are typically used in the form of honeycomb monoliths or coated metal plates stacked as monoliths with parallel channels, and normally not as packed beds, due to two main advantages of honeycomb structured monoliths. Honeycomb monoliths exhibit superior resistance to fly ash plugging and the pressure drop over the catalyst bed is much lower[17,26]. Honeycombs are obtained by extrusion, where powdered catalyst material is mixed with binders and water forming a paste extruded into the desired shape. Many catalyst companies are also using corrugation of a flexible support, where powdered ceramic materials are deposited with a binder, see Figure 2.3 on the preceding page.

## 2.4. SCR reaction mechanism for vanadium-based catalysts.

Even though the vanadium-based catalysts are and have been widely used for many years a definite reaction mechanism has not yet been agreed upon. In the literature different mechanisms have been proposed and there are still a great deal of uncertainty and disagreement whether it is one or the other mechanism, which describe the process the best[4,16,20,36,37]. Hence it is not possible to describe a definite mechanism, but only a selection of the most accepted mechanisms.

Adsorption-desorption studies of reactants were the first tool used to develop a reaction mechanism. All studies of ammonium adsorption on $V_2O_5/TiO_2$ , pure $V_2O_5$ and $TiO_2$ show that ammonium adsorbs strongly on the surface[36,38–43].

Figure 2.4 shows the different adsorption sites on a $V_2O_5/TiO_2$ catalyst, the majority of $NH_3$ is adsorbed on vanadyl sites through a Lewis interaction or at Brønsted acidic sites. Furthermore
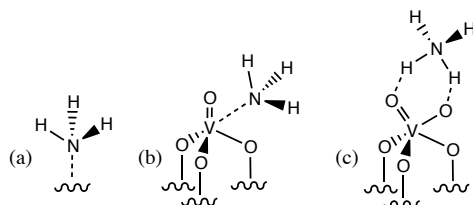


**Figure 2.4.:** *Different ammonia adsorption sites on a $V_2O_5/TiO_2$ catalyst. (a) Lewis coordinated ammonia to a Ti atom, (b) Lewis bonded $NH_3$ at vanadyl site, (c) $NH_3$ coordinated to a Brønsted site. Adopted from Busca et al.[16]*
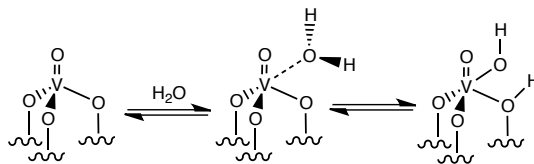
**Figure 2.5.:** *Water interaction with $V_2O_5/TiO_2$ catalyst generating a Brønsted site from a Lewis site. Adopted from Busca et al.* [16]

$NH_3$ can also be adsorbed on the $TiO_2$ carrier, but only at Lewis sites due to the chemical nature of the carrier[44]. If the catalyst is sulphated these groups can also adsorb $NH_3$ on new sulphate Brønsted and Lewis sites[45]. In dry conditions $NH_3$ predominately adsorb as Lewis coordinated ammonia[46], but in wet conditions the Brønsted/Lewis ratio can be shifted to a ratio of 1:1, see Figure 2.5[16].

Adsorption of the other SCR reactant NO has additionally been extensively investigated in the literature[16,20,36,40,47]. In recent studies authors agree that NO does not adsorb on an oxidised $V_2O_5/TiO_2$ catalyst surface. Transient-response experiments by Lietti et al. supported the adsorption studies, confirming that NO does not adsorb on the catalyst surface, contrary to ammonia which is adsorbed[47–49]. Due to this fact all early Langmuir-Hinselwood mechanisms can be disregarded. This applies for instance to the mechanism proposed by Takagi et al.[50], where NO is oxidised and adsorbed as $NO_2$ and reacts with $NH_3$ on the surface; as well as the straight forward Langmuir-Hinselwood mechanism proposed by Odriozola et al.[51] where adsorbed $NH_3$ and NO react on the catalyst surface.

Today it is widely accepted that the SCR mechanism is an Eley-Rideal mechanism, where ammonia is adsorbed on the catalyst surface and react with NO from the gas phase or from a weakly bound state[20,36,37,41,52–55].

Inomata et al. proposed a mechanism already in 1980, see Figure 2.6(a) on the following page, that founded and inspired many other mechanisms years after[20]. This mechanism was based on FTIR, ESR and activity data on pure $V_2O_5$, and later Inomata et al. justified that the mechanism also applied to a $V_2O_5/TiO_2$ catalyst or other supported $V_2O_5$ catalysts[56,57]. Inomata et al. based the mechanism on the findings of a observed proportionality between activity and the concentration of $V^{5+}=O$, concluding that this site had to be the active centre. In this mechanism ammonia is adsorbed on a dual Lewis/Brønsted site, subsequently NO reacts with the surface $NH_4^+$ group forming an activated complex. The activated complex then decomposes into $N_2$ and $H_2O$ leaving a $V^{4+}-OH$ and a $V^{5+}-OH$ group. In the last step $V^{4+}-OH$ is oxidised back to $V^{5+}=O$ and the catalytic cycle is closed. Later Janssen et al. confirmed this mechanism and modified it a little using transient tracing studies with $^{15}NH_3$ and $^{18}O_2$[58,59]. Later great effort has been given into identifying the surface species of adsorbed $NH_3$ by the means of FTIR[40,42,50,60–62]. All these studies conclude as expected that ammonia adsorb on
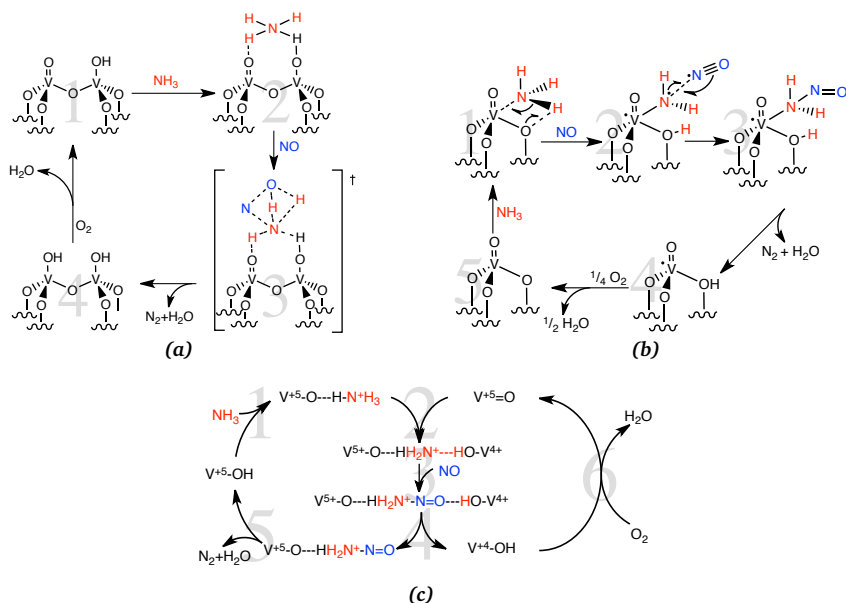
**Figure 2.6.:** *Three different Eley-Rideal mechanisms for the SCR reaction adapted from, (a) Inomata et al. 1980 [20,56], (b) Ramis et al. 1990 [16,36], (c) Topsøe 1994 [37]*

two different sites, Lewis and Brønsted, forming coordinated $NH_3$ and protonated $NH_3$. Coordinated Lewis bonded $NH_3$ has a characteristic symmetric and antisymmetric bending mode $(\delta_s NH_3)$[a] and $(\delta_{as} NH_3)$ respectively at 1230-1260 cm$^{-1}$ and 1602-1620 cm$^{-1}$ respectively. And adsorbed $NH_4^+$ also has two distinct peaks one at 1664-1665 cm$^{-1}$ $(\delta_s NH_4^+)$ and another at 1425-1428 cm$^{-1}$ $(\delta_{as} NH_4^+)$ [40,42,62]. Since these discoveries, there have been a discussion between several research groups on whether it is the Lewis coordinated $NH_3$ that are active or the Brønsted acid bonded ammonia that are the active specie.

One party in the discussion was Ramis et al. [40] who proposed a mechanism, known as the "amide-nitrosamide" mechanism, see Figure 2.6(b). Based on FTIR investigations of a 5 wt.% $V_2O_5/TiO_2$ catalyst, they argued that the active centres of the catalyst was Lewis acid sites. They performed experiments where conducted using a conventional evacuation/gas-manipulation cell, the catalyst was pressed into a self-supporting disk and exposed to SCR gasses followed by evacuation at different temperatures. This Confirmed that $NH_3$ is much stronger adsorbed on the surface than NO and co-adsorption of neither NO nor $NO_2$ was not observed due to the stronger basicity of $NH_3$ [40]. $NH_3$ adsorption experiments showed that Brønsted coordinated ammonia desorbed rapidly at increasing temperatures, where the concentration of Lewis coordinated ammonia only changed slightly. This observation was used to conclude that the Lewis centres were the preferred adsorption sites, and adsorption at Brøn-

---

[a]Notation describing the mode either bending or vibration, $\delta_{as}$ and $\nu_{as}$. "$_{as}$","$_s$" and "$_{sic}$" denotes symmetric, antisymmetric and scissoring.

sted sites would result in a migration to Lewis sites when vacant. Upon further heating and evacuation a new specie was observed at 1535 cm$^{-1}$, which they assigned to an amide specie ($\delta_{sci}NH_2$). Ramis et al. observed that this new specie was not present when exposed to SCR gas, and concluded that it reacted fast with NO. These observations were the base for a new mechanism referred to as the "amide-nitrosamide" mechanism. Furthermore they observed that the peak corresponding to Lewis coordinated $NH_3$ decreased faster than that of Brønsted coordinated $NH_3$ when exposed to NO and $O_2$. They concluded that this supported that the active centre was indeed a Lewis acid centre.

These observations were used to formulate the "amide-nitrosamide" mechanism, see Figure 2.6(b) on the facing page for a schematic representation of the mechanism. In the first step of the mechanism ammonia is adsorbed on a Lewis acid site that activates the ammonia and forms a radical amide $NH_2$ specie, resulting in a reduction of vanadium. Then the activated ammonia reacts with gas-phase NO forming a nitrosamide intermediate, that rapidly decomposes to nitrogen and water leaving a reduced vanadium site, and is then oxidised closing the catalytic circle [40]. Early support for the nitrosamide route is found in the kinetic study made by Farber et al. [63], where the authors concluded that nitrosamide was the primary step leading to $N_2$ and $H_2O$. This is the earliest mechanism proposing an activation of ammonia and explaining the formation of nitrosamide.

Later Topsøe et al. [37,41,54] investigated the SCR reaction further again using FTIR, in a flow cell and with reaction conditions similar to a working catalyst. They combined temperature programmed in-situ FTIR measurements with on-line mass spectroscopy measurements on a 6wt.% $V_2O_5/TiO_2$ catalyst. By doing so they observed that after adsorption of $NH_3$ at room temperature followed by heating and a flow of NO and $O_2$ the amount of V-OH on the surface increased and the resulting band was shifted upwards compared to a normal V-OH group. Hereby they concluded that reduced V-OH groups were formed in the SCR mechanism, which explained the shift and increase of intensity.

The V=O overtone at ∼2044 cm$^{-1}$ and the V-OH band at 3600 cm$^{-1}$ were also studied upon ammonia adsorption. A decrease of both bands were observed but V-OH much more distinct than V=O, which only decreased a little and a shift of the remaining V=O overtone was observed. Both peaks could be regenerated upon oxidation of the catalyst in $O_2$ or NO+$O_2$. These observations led to the conclusion that both V-OH and V=O sites played an important role in the mechanism [54].

But before a conclusion could be made, the nature of adsorbed $NH_3$ had to be investigated to determine the active site. Like countless other investigations two different types of adsorbed ammonia were observed, ammonia adsorbed on Lewis and Brønsted acid sites. Quantifying the amount adsorbed on each site was done by integration of the usual $\delta_{as}NH_4^+$ peak at 1430 cm$^{-1}$ and the $\delta_{as}NH_3$ peak at 1606 cm$^{-1}$. The choice of the $\delta_{as}NH_3$ peak instead of the more common used $\delta_s NH_3$ peak, has been criticised by several authors [4,16,17]. The $\delta_{as}NH_3$ peak is

difficult to used due to a overlapping $H_2O$ peak at 1609 cm$^{-1}$, see Figure 7.3 on page 83. The measurements showed that the amount of $NH_4^+$ (Brønsted adsorbed ammonia) was proportional to the NO conversion and there were no correlation to Lewis coordinated $NH_3$ on the surface. This indicated that only Brønsted acid adsorbed ammonia played an important role in the mechanism, as opposed to the earlier proposed mechanisms [20,36].

In Figure 2.6(c) on page 16 the schematic representation of the Topsøe et al. mechanism is shown [54]. The mechanism is divided in to 6 steps, in step 1 $NH_3$ is adsorbed on a $V^{+5}$-OH Brønsted acid centre, next the adsorbed ammonia is activated via a partial transfer of an H atom to an adjacent $V^{+5}$=O site leading to a reduction of vanadium. Gaseous or more likely weakly adsorbed NO reacts with the activated ammonia forming an activated intermediate, that decomposes rapidly forming $N_2$ and $H_2O$ (step 4 and 5) leaving a $V^{+5}$-OH and a $V^{+4}$-OH group. The catalytic cycle is then completed with an oxidation of the formed $V^{+4}$-OH group back to $V^{+5}$=O in step 6. Later Dumesic et al. modified the catalytic circle to match a kinetic model, describing the SCR reaction kinetics of an industrial $V_2O_5/TiO_2$ catalyst [55].

Many authors support this mechanism [52,64–66], but it is also widely criticised, this is due to the fact that Topsøe et al. was not able to follow the precise behaviour of Lewis coordinated $NH_3$, as the spectral region below 1300 cm$^{-1}$ was cut out [16,17]. Topsøe et al. have never answered this criticism with experimental evidence. Use of the $\delta_{as}NH_3$ peak at 1606 cm$^{-1}$ as a measure of the total Lewis adsorbed ammonia is inadequate. Thus is due to the fact that, the two peaks originating from Lewis coordinated ammonia $\delta_{as}NH_3$ and $\delta_s NH_3$ are not proportional as functions of temperature, suggesting that the two peaks originate from two different types of Lewis coordinated ammonia [67]. Furthermore in a review Busca et al. [16] stated that the formation of a $NH_3^+$ species is very unlikely and the possibility that it is an intermediate involved in a slow step is even more unlikely.

Later Anstrom, Topsøe and Dumesic [68,69] answered this criticism with two computational studies on a modified mechanism, where the intermediate in step 3-4 resulted in the formation of nitrosamide. They used a $V_4O_6H_{12}$ cluster as a base for the DFT$^a$ calculations, resulting in an estimation of the rate determining step to be the decomposition of the $NH_3NHO$ intermediate as earlier proposed. Soyer et al. [71] made the same calculations resulting in another more likely conclusion that the rate-determining step, was the formation of the $NH_3NHO$ intermediate. Interesting in these two studies was that it was shown that the decomposition of nitrosamide must take place on the surface of the catalyst, and not in gas phase as earlier presumed.

Vittadini et al. [72] have made a recent computational study on two separate clusters one monomeric and one polymeric, showing that $NH_3$ only can be protonated at polymeric vanadia species and not at a single V-OH group. They also found that the reaction towards nitrosamide could occur both at Lewis and Brønsted sites. But the Brønsted mechanism did not contain

---

$^a$DFT Density functional theory is a quantum mechanical modelling method, used in physics and chemistry to investigate the electronic structure [70]

**Table 2.1.:** *Amount of Na, S, Cl and K in different fuels wt.% on dry basis - only an estimate because the amounts can vary in a high degree. MSW (Municipal Solid Waste).*

| | Coal | | Brown coal | | MSW[a] | | Wood chips | | Forrest Residues | | Straw | |
|---|---|---|---|---|---|---|---|---|---|---|---|---|
| | ppm. | Ref. | wt.% | Ref. | wt.% | Ref. | wt.% | Ref. | wt.% | Ref. | wt.% | Ref. |
| Na | 0.015-0.055 | [73] | <0.23 | [74] | 0.16-0.39 | [75] | 0.04-0.1 | [76,77] | 0.01-0.05 | [77] | <0.3 | [76] |
| S | 0.17-2.2 | [73,78] | 0.2-0.48 | [74] | 0.07-0.3 | [75,78] | 0.8-0.18 | [76,77] | 0.02-0.05 | [77] | 0.1-0.2 | [76] |
| Cl | 0.04-0.23 | [73,78] | <0.031 | [74] | 0.36-1.9 | [75,78] | 0.06-0.12 | [76,77] | 0.01-0.03 | [77] | 0.1-1.1 | [76] |
| K | 0.006-0.06 | [73] | <0.085 | [74] | **0.11-0.5** | [75] | **0.05-0.4** | [76,77] | **0.1-0.2** | [77] | **0.2-1.9** | [76] |

[a] Calculated from ash data.

a NH$_3$NO intermediate as proposed by Topsøe et al. [37,41,54]. Furthermore they showed that the reduction of vanadium take place through the bridging V-O-Ti oxygen, matching another study done by Calatayud et al. [64] and not involving a breaking of the strong V=O bond as proposed by Inomata et al. and Topsøe et al. in their mechanisms [20,37,41,54].

In summary resent studies show that the SCR reaction can occur both at Lewis and Brønsted sites and that the reaction involve a formation of nitrosamide. Furthermore it has been shown that the V=O bond is not broken and that the active oxygen of the vanadate species are the bridging V-O-Ti oxygen. These new conclusions do not fit any of the three conventional mechanisms and therefore calls for a new reaction mechanism.

## 2.5. Deactivation and biomass

There are generally three different mechanisms responsible for SCR catalyst deactivation, fouling/coking, sintering and chemical deactivation/poisoning. Fouling will not be discussed in the following, because it is only a physical problem and is resolved by monolith design and air purging in the power plant [79].

### 2.5.1. Fuel composition

The rate of the catalyst deactivation is to a very great extent determined by the type of fuel combusted in the power plant. Depending on the fuel, the SCR catalyst is exposed to many different gaseous or aerosol species. Natural gas is one of the cleanest fuels in this context and therefore deactivates the catalyst very slowly. Whereas combustion of waste or straw deactivates the catalyst much faster, due to the composition of the fuel. Composition of various fuels and the resulting ash have been analysed and all studies show a significant increase in the quantity of alkali and alkaline-earth elements in biomass fuels [74–76,78]. In Table 2.1 the composition of different fuels are listed, only the four most important elements Cl, K, Na and

S responsible for the majority of catalyst deactivation are noted. Sulphur in the flue gas is of concern, due to the potential oxidation of $SO_2$, which readily reacts with $NH_3$ and water forming ammonium bisulphate or ammonium sulphate. That may cause corrosion of materials downstream the SCR reactor and deactivate of the catalyst due to plugging[80]. This is an issue especially when burning coal, because of the high sulphur content. This issue can be resolved by lowering the vanadium content on the catalyst, hereby lowering the $SO_2$ oxidation activity of the catalyst. On the other hand, the sulphur content in biomass is typically lower compared to coal, so by firing or co-firing with biomass the $SO_2$ concerns are dramatically reduced. Also chloride is a major concern due to severe enhancing of sintering of Cu based catalysts and erosion and fouling[79]. But also vanadium based catalysts show sign of deactivation due to high chloride concentrations. Lisi et al.[81] investigated the deactivation of vanadium-based catalysts and showed a slight decrease in activity upon HCl exposure. On the other hand the surface acidity increased slightly, and this had a positive effect the potassium resistance increasing the acidity of the catalyst.

Alkali metals are responsible for the highest deactivation rate. Combustion of wood chips, MSW and especially straw exposes the catalyst to high concentrations of K and Na[76], see Table 2.1 on the preceding page.

### 2.5.2. Chemical deactivation

Even though the alkali metal content in coal is very low, a deactivation has been noticed by Chen and Yang[82]. They observed that the strength of the alkali metal poison, was directly related to its basicity, following the order $Cs_2O > Rb_2O > K_2O > Na_2O > Li_2O$. This trend has been confirmed several times afterwards[83,84]. But with potassium and sodium representing 99% of the alkali metal content of the fuel, they are the only real concern. Furthermore Chen and Yang[82] showed that $SO_2$ suppressed the deactivation, this is due to the sulphation of the catalyst surface, which increase the acidity. This finding indicates that the acidity of the catalyst is very important in terms of potassium resistance.

With the increasing combustion of biomass, due to the political pressure for $CO_2$ neutral fuels the concern about alkali metal deactivation has increased. As a reaction to the increased awareness of the subject a number of publications on the effect of alkali species on vanadia-titania based SCR catalyst have been published in the last decade[7,29,81,85–92].

One of the more recent studies was done by Wieck-Hansen et al.[93] where they studied the deactivation of multiple types of commercial SCR catalysts used in a power plant co-combusting 20 wt.% straw with coal in a high dust configuration. The activity of the catalysts decrease very fast and at the same rate for all manufacturers resulting in a deactivation of ca. 35% after only 2860 hours. As for comparison a normal SCR catalyst has a life span of about 3-5 years. Firing only with biomass this deactivation rate would be much faster, due to the lack

of fly ash adsorbing great amounts of potassium before exposing the catalyst. Strege et al.[94] showed that this deactivation rate is even higher for an 80 wt.% wood 20 wt.% coal mixture deactivating the catalyst 50% in 2800 hours.

As a consequence of the increased use of biomass and the severe catalyst deactivation that potassium causes the interest for an understanding of the deactivation mechanisms has increased. Numerous spectroscopic and acidity studies show that the deactivation is directly related to the reduction of the number of $V_2O_5$ Brønsted acid sites on the catalyst[76,77,81,87–89]. But the redox capability of the catalyst is also greatly reduced, because the alkali metal stabilises the vanadium in oxidation state +5[82,95].

Chen et al.[82] and Zheng et al.[96] showed by chemisorption of $NH_3$ on gradually deactivated catalysts that the ability to adsorb $NH_3$ decreased with increasing potassium doping. Chen et al.[82] also showed that the Lewis sites were unaffected by the potassium deactivation supporting the Topsøe et al. mechanism[37,41,54]. But like Topsøe et al. they used the peak at 1605 $cm^{-1}$ to represent Lewis acid sites, which is a poor choice due to the earlier stated reasons.

On the basis of Chen et al.[82] and Zheng et al.[96] a simple deactivation mechanism, where Brønsted acid sites are removed after reaction with potassium, can be stated:

$$V-OH + KCl \longrightarrow V-OK + HCl \qquad (2.10)$$

Hangstum et al.[95] and later Lietti et al.[86] proposed that potassium reacts with the active sites altering the reactivity by decreasing the reducibility of the active vanadium site - in accordance with the Ramis et al. mechanism[36]. Lietti et al. showed that the potassium deactivation also reduces the Brønsted acidity of the catalyst[86]. Again this shows that both Lewis and Brønsted sites are very important in the SCR reaction mechanism, and not one or the other.

Several of the groups investigating the deactivation as a function of potassium have observed an almost complete loss of activity already at a K/V mole to mole ratio of 0.5[7,76,82,88]. This disagrees with the simple mechanism in Equation (2.10) and suggests that polymeric vanadia species can be deactivated by only one K to two vanadia sites.

Recent DFT studies on the deactivation mechanism suggest models in better agreement with the experimental findings stated above. Two studies propose that the deactivating potassium preferentially occupy holes between four $V_2O_5$ centres and thereby shield potential Lewis and Brønsted sites. One drawback of these studies are that both DFT studies are carried out using $V_2O_5$ clusters and left our the $TiO_2$ carrier[97,98]. Still they supply an explanation for the fast deactivation.

Calatayud et al.[83] used a better model, a small $V_2O_5$ cluster with added anatase substrate. They showed that at a K/V ratio of 0.5, potassium would interact with two neighbouring vanadia units coordinating to a V-O-Ti on one and a terminal V=O on the other, but also to the support. Hence also explaining the fast deactivation rate.

Another more simple model was proposed by Due-Hansen et al.[85] based on quantum me-
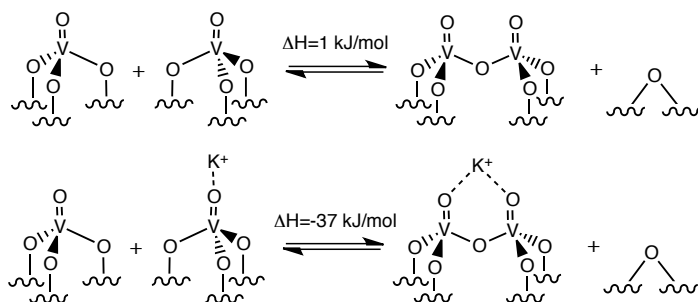
**Figure 2.7.:** *Potassium deactivation model proposed by Due-Hansen et al.* [85].

chanical calculations, see Figure 2.7. This mechanism can also explain the total deactivation at K/V=0.5 by a condensation of two neighbouring vanadia sites.

But this model contradicts the findings of Kiwi-Minsker et al. [99] that report an increase of momeric species upon potassium doping. Lewandowska et al. [100] supports this with observations of alkali doping that appears to minimise vanadia polymerisation. They state that it is due to the strong interaction with the support and alkali sites at the interface.

So the potassium deactivation mechanism is today not fully understood but it implicates a reaction between potassium and the active vanadate site that deactivates two sites per. potassium atom. This deactivation is correlated with a drop in both Lewis and Brønsted acidity of the catalyst.

### 2.5.3. Alkali resistant SCR catalysts.

As previously described, the state of the art commercial catalysts are severely deactivated by potassium, even catalysts doped with $WO_3$ to increase the resistance, have a very short life cycle [89,93,94].

Several methods for increasing the potassium resistance of a catalyst are available. One approach is to protect the active centres by using a more acidic support. The support then reacts with the potassium making stable potassium compounds, before a deactivation of the active centres occurs [7,101]. A more acidic support can be obtained either by increasing the support by sulphation or by using a more acidic support such as sulphated $ZrO_2$. Yet another approach is to substitute the active metal with a metal less prone to deactivation by potassium, such as CuO, $Fe_2O_5$ or a Ce-based active metal [32,102]. However these catalyst systems are not as active as the commercial $V_2O_5/TiO_2$ catalysts and they are still deactivated by potassium, although at a slower rate. The advantage of slow deactivation is not big enough to compensate for the low activity of the fresh catalyst.

A third alternative approach is to increase the active metal content, by increasing the surface

area of the support, making a more active and potassium resistant catalyst, due to the increased number of active sites [103–105].

A more recent solution to the potassium deactivation of the industrial catalyst is a new type of catalyst. Hollandite manganese oxide, which combines two types of active sites, one type of catalytically active sites on the external surface and another type of alkali-trapping sites in the internal tunnels of the support. Alkali will then accumulate on the catalytically active surface sites and under normal reaction conditions spontaneously migrate into the support hereby the catalyst regains the lost activity. This is a very elegant solution to the problem, but the drawback is that the activity of the catalyst is very low and despite it is not deactivated it is not usable under industrial conditions [106]. Furthermore several authors have shown that $MnO_2$ deactivates severely in flue gasses containing $SO_2$. Until this problem is solved the use of $MnO_2$ as active component is not feasible, not even in flue gases containing very low concentrations of $SO_2$ [107,108].

### 2.5.4. Sintering

Sintering is the last type of deactivation described here. It is generally a temperature induced chemical transformation, which is responsible for the deactivation of catalysts. Especially nano-based catalysts are prone to sintering [109,110]. Sintering is loss of catalyst surface area due to crystallite growth of either the support or the active phase forming big less active clusters [111].

Pore collapse and chemical transformation are also problems, that deactivate the catalyst, an example is the transformation of a promoting phase to a non-promoting phase e.g. anatase to brokelite [112,113].

Sintering takes place at high temperatures and is normally accelerated by water vapour. Supports such as zeolites are very prone to this type of deactivation [33].

The SCR catalyst is also thermally deactivated due to sintering of the active phase $V_2O_5$ at very high temperatures (>450 °C). There are three mechanisms of metal oxide growth namely crystallite migration, atomic migration and vapour transport. These processes are very temperature dependent, as the mobility of the surface metal oxide increases with increasing temperatures.

Tamman and Hütting temperatures are empirical correlations between mobility and the melting point of the metal oxide, see Equation (2.11) and (2.12). The Hütting temperature is the temperature where the atoms at defects become mobile and the Tamman temperature is where the atoms from the bulk are mobile [111].

$$T_{Hütting} = 0.3 T_m \qquad (2.11)$$

$$T_{Tamman} = 0.5 T_m \tag{2.12}$$

For $V_2O_5$ with a melting point of $T_m$=681°C[114] the Tamman temperature is 477°C and for this reason higher temperatures should be avoided.

Sintering of a $V_2O_5/TiO_2$ catalyst can be avoided to some degree by adding $WO_3$ to the catalyst. $WO_3$ acts like big islands separating the vanadia on the surface hindering sintering of the active centres[4,16,29]. The Tamman and Hütting temperatures are also very important when a catalyst is potassium poisoned. Because even at low temperatures the potassium will be mobile and evenly distributed with time, hereby deactivating the catalyst due to the reaction between potassium and the active sites on the catalyst[85].

# 3

## Experimental

The present chapter is a short introduction to all the experimental setups used in this thesis, however some very specific measurements are introduced in the chapter where the results are presented and discussed. Sol-gel synthesis of the catalysts is likewise not described in detail, since a whole chapter is devoted to this subject. The first section is describing the characterisation methods used to get an insight of the composition, acidity and morphology of the catalysts. The second section is devoted to a description of the "home made" test setups, used to measure activity of the catalysts throughout the thesis. Finally follows a description of the potassium deactivation methods and the method used to make the clay extrudates and at last a description of the industrial reference catalyst.

## 3.1. Characterisation methods.

### 3.1.1. X-ray powder diffraction (XRPD)

X-ray powder diffraction were performed using a Huber G670 Guinier camera and $CuK_{\alpha 1}$ radiation, $\lambda = 1.5406$Å. Sample preparation was done by placing a thin powdered sample layer on tape in a plate sample holder that is rotated during data collection. Exposure time was 60 minutes and the data was collected in the range 3-100° 2$\Theta$ in steps of 0.005° 2$\Theta$.

The crystallite size was calculated using the Scherrer equation[115], using the 101 reflection at 25° 2$\Theta$. The calculation was done by using the program `win-prep`[116], which fits a spline to the chosen reflection, and then performs the calculation based on the generated spline.

### 3.1.2. Scanning Electron Microscopy (SEM)

Scanning electron microscopy of catalysts was performed using a Quanta 200 ESEM FEG, and images were typically obtained with acceleration voltage between 5 and 10 kV using the secondary electron Everhart-Thornley detector. When using the Solid State Backscattered Electron (SSBE) detector the acceleration voltage was increased to 10-20 kV, during mapping the acceleration voltage was set to 20 kV and a spot size of 5 to ensure a faster measurement using EDX (Energy-Dispersive X-ray).

Specimens were prepared by dry dispersing of the catalyst powder on carbon tape without further carbon coating. The catalyst plate measurements was done by placing a small cut out of the catalyst plate on carbon tape with silver paint gluing it stuck on carbon tape and ensuring low charging.

### 3.1.3. Transmission Electron Microscopy (TEM)

High-resolution transmission electron microscopy images of the catalysts were carried out using a Tecnai T20 G2 at an acceleration voltage of 200 kV.

Powder samples were deposited on copper grids, simply by applying the powder directly on the grid and removing excess by tilting the sample holder.

### 3.1.4. Temperature Programmed Desorption (TPD)

Temperature programmed desorption of $NH_3$ was carried out on a Micromeretics AutoChem II 2920. The measurement procedure was the same for all measurements throughout the thesis. Approximately 150 mg sample was dried at 400 °C in helium for 60 minutes, then the sample was saturated with 50 $^{ml}/_{min}$ 1% $NH_3$ in He for 120 minutes at 100 °C. To ensure removal of loosely bound ammonia the sample was purged with 50 $^{ml}/_{min}$ He for 20 minutes, before performing the TPD at a heating rate of 10 $^{°C}/_{min}$ from 100 °C to 700 °C in 50 $^{ml}/_{min}$ He.

### 3.1.5. Nitrogen physisorption (BET)

BET surface area measurements and $N_2$ adsorption measurements, were performed at liquid nitrogen temperature on a Micromeretics ASAP 2020. Prior to the measurement the samples were degassed at 200 °C under vacuum for 6 hours.
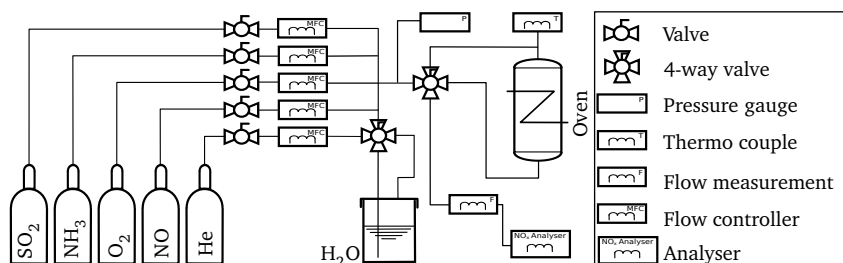
**Figure 3.1.:** *Schematic drawing of the flow setup for catalytic activity measurements.*

### 3.1.6. Mercury Intrusion Porosimetry (MIP)

Pore distribution above 10 nm was determined by mercury intrusion porosimetry on a CE Instruments Pascal 140/240 porosimeter. Samples were dried at 150 °C overnight prior to the measurement.

### 3.1.7. Thermo Gravimetric Analysis (TGA)

Thermo gravimetric analysis performed on seeds and uncalcined catalysts were executed on a Mettler Toledo TGA/DSC 1 SF instrument equipped with a single differential thermal analysis sensor. About 25 mg sample were placed in a 70 $\mu$l alumina container, and was subsequently heated to 500 °C with a heating rate of 10 $^{\circ}$C$/_{min}$ under 20 $^{ml}/_{min}$ $N_2$ flow, and the change in mass was measured.

### 3.1.8. Nuclear magnetic resonance spectroscopy (NMR)

The vanadium precursor, ethyl orthovanadate, were characterised using $^1$H-NMR, recorded on a Varian Mercury - 300 Mhz. Using $CDCl_3$ solvent.

### 3.1.9. Inductively Coupled Plasma - Mass Spectrometry (ICP-MS)

ICP-MS measurements of the vanadium precursor, ethyl orthovanadate, was carried out on a Perkin Elmer ELAN 6000 with cross-flow nebulizer and argon plasma and the amount of vanadium was quantified using 4 different ammonium vanadate solutions.

**Figure 3.2.:** *Picture of setup for catalytic testing at various temperatures, NO$_x$ analyser is located beneath the table.*



**Figure 3.3.:** *Quartz reactor with a loaded sample fixed between two layers of quartz wool and diluted in SiO$_2$.*

## 3.2. Activity measurements

All activity measurements of SCR catalysts in the thesis is performed on the same setup, which is schematically illustrated in Figure 3.1 on the preceding page and a picture of the actual setup is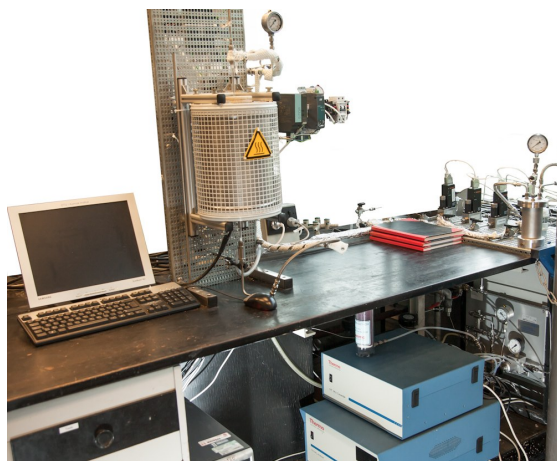 depicted in Figure 3.2. The setup is controlled by a specially designed `Labview` program, monitoring the gas flows through the four mass flow controllers and one mass flow meter measuring the total flow. The oven temperature and the catalyst temperature was also monitored and logged with the other data every 60 seconds. SCR activities were measured by a Thermo Environmental Chemiluminesence analyser model 17C NH$_3$ analyser, equipped with a delusion unit, monitoring the NO, NO$_2$ and NH$_3$ concentrations.

A typical activity measurement was carried out using 8 mg catalyst fractionated to a particle size of 150-300$\mu$m fixed in a quartz plug-flow reactor with quartz wool and diluted in SiO$_2$ of same fraction, see Figure 3.3. The flow was held constant at 730 $^{ml}/_{min}$ for all measurements, containing 1000ppm NO, 1100ppm NH$_3$, 3% O$_2$ and He as carrier. In some cases H$_2$O was introduced by saturation of the He flow by passing it through H$_2$O in a bubble flask, but for the majority of the measurements H$_2$O was not added. The water was left out due to false peaks originating from H$_2$O interacting with the detector and to ensure that the SCR reaction was first order in respect to NO.

Typically the catalyst was heated to 420 °C and activated for 20 minutes, followed by cooling to 200 °C. Then the activity was measured from 200 to 440 °C and back in 11 and 8 steps respectively, steady state was ensured by measuring at each temperature for 20 minutes. At

each temperature the `Labview` program logged the temperature of the oven at the catalyst, and furthermore the concentration of NO, $NO_2$ and $NH_3$.

In some cases $SO_2$ was added to investigate whether the catalyst did deactivate under these conditions, in this case a Perkin Elmer Lambda 1000 UV/VIS spectrophotometer was used as NO detector.

### 3.2.1. Rate expression

A convenient method to evaluate the catalyst activity is by using the pseudo first order rate constant. By doing so, catalysts can be compared regardless of mass or flow used during the activity measurement. This rate constant for species "A" can be derived from the mole balance equation for a packed-bed reactor [117].

$$\frac{dF_A}{dW} = r'_A \tag{3.1}$$

Where $W$ is the catalyst weight, $F_A$ is the molar flow rate and $r_A$ is the rate constant for species "A". For a flow system, $F_A$ can be given in terms of start molar flow rate $F_A0$ and NO conversion. By substituting $(F_A = F_{A0}(1-X))$ we obtain.

$$F_{A0}\frac{dX}{dW} = -r'_A \tag{3.2}$$

After the assumption of no pressure drop we can integrate with the limits W=0, W and X=0, X obtaining the following:

$$W = F_{A0}\int_0^X \frac{dX}{-r_A} \tag{3.3}$$

According to several authors [20,82,118,119] the rate equation can be expressed as Equation (3.4).

$$r_{NO} = k[NO]^1 \cdot [NH_3]^0 \tag{3.4}$$

Substituting Equation (3.4) into Equation (3.3) we get.

$$W = F_{NO0}\int_0^X \frac{dX}{-k[NO]} \tag{3.5}$$

Then the concentration of NO can be expressed by the initial concentration $([NO] = [NO]_0 \cdot (1-X))$ and the degree of conversion X, and after some rearrangement we obtain:

$$k = -\frac{F_{NO0}}{W[NO]_0}\int_0^X \frac{dX}{(1-X)} = -\frac{F_{NO0}}{W[NO]_0}ln(1-X) \tag{3.6}$$

Hereby we have a rate expression, which can be used to express the catalytic activity depended on catalyst mass and molar flow. All activity measurements are carried out using 8 mg catalyst and the flow was held constant throughout the thesis for the sake of easy comparison, so both the rate and the conversion can be used for comparing all the catalysts. In most activity plots the activity constant is used as y-axis, due to ease of comparison between different studies done by other authors. Some plots also contain the conversion on the y2-axis to show the conversion.

## 3.3. Catalysts

Many different catalysts have been synthesised for this study, the synthesis of sol-gel catalysts are described in Section 4.1 on page 33 and Section 4.10 on page 51. The synthesis details of all other synthesis are listed in the following.

### 3.3.1. Synthesis and potassium deactivation.

Synthesis of catalysts with tungsten metal doping were done by Incipient Wetness Impregnation (IWI) of 15wt.% $V_2O_5/TiO_2$ catalysts, synthesised as described in Section 4.10 on page 51, with Ammonium metatungstate hydrate (Fluca 99%).

Synthesis of catalysts with molybdenum metal doping were done by adding an ethanol solution of bis(acetylacetonato)dioxomolybdenum(VI) (99% Sigma Aldrich) in step ⑥ of the synthesis, see Figure 4.1 on page 34.

Potassium doping was also done by IWI with a solution of $KNO_3$ (Merck,>99%) on the powder catalysts to obtain a specific potassium loading pr. g of catalyst. After drying at 100 °C the samples was calcined at 250 °C for 2 hours and further heated in the activity setup at 420 °C for 20 minutes before activity measurements.

### 3.3.2. Sepiolite and bentonite extrudates.

The sepiolite (Sigma-Aldrich Lot:BCBB5518) and bentonite (Sigma-Aldrich Lot:MKBD2446) extrudates was prepared by mixing with 20 wt.% $V_2O_5/TiO_2$ catalyst powder and water with different amounts of $H_2SO_4$. The acidic water was added until a homogeneous paste was obtained with an adequate viscosity for extrusion, ca. 1 g pr. 1.8 g of catalyst clay mixture. The paste was then extruded from a 5 ml syringe with a 2 mm orifice, and then dried for 3 hours at ambient conditions. The extrudates were then dried at 100 °C for another 3 hours
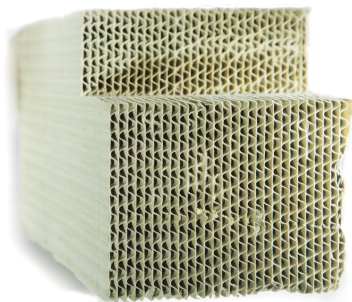
**Figure 3.4.:** *Commercial 3wt.% 7wt.% $WO_3$ on $TiO_2$ anatase a SCR catalyst monolith based on a $SiO_2$-fibre framework.*



**Figure 3.5.:** *Crushed and fractionated sample, where all the $SiO_2$ fibres have been removed.*

and calcined at 400 °C for 2 hours. Optimisation of $H_2SO_4$ concentration and amount of used clay is discussed in Chapter 5 on page 53

### 3.3.3. Reference Catalyst

In this study two different reference catalysts have been used, a commercial $V_2O_5-WO_3-TiO_2$ monolith with a vanadia loading of 3 wt.% and tungtenoxide of 7 wt.% on $TiO_2$ anatase. The monolith, a $SiO_2$-fibre framework with active catalyst distributed on it, see Figure 3.4, was crushed into a powder $SiO_2$-fibre catalyst mixture. $SiO_2$-fibres were separated and the remaining catalyst powder was pressed at 2 tons and fractionated to a particle size of 150-300 $\mu$m, see Figure 3.5. This fractionated powder was then tested for activity and compared to the synthesised catalysts.

The second reference catalyst was a commercial plate catalyst comprising 3 wt.% $V_2O_5$ and $TiO_2$ on a $SiO_2$-fibre plate. This catalyst was used only for the potassium exposure described in Section 6.4 on page 71.

# 4

## Synthesis optimisations

This chapter shows the route to understanding and optimisation of the sol-gel synthesis of the nano-particle SCR catalysts. The optimisation goal is, to be able to produce large amounts of catalyst that are as active as possible and have the highest potassium resistance. This can be achieved by identifying the important synthesis steps, optimise them and simplify the process.

## 4.1. First proposed synthesis procedure

The novel synthesis procedure of the nano-particular vanadia/anatase catalyst was based on the discoveries of Hari Bala et al. [120,121]. They showed that nano crystalline anatase could be synthesised using a titanium isopropoxide precursor with a substrate directing agent. Adding a vanadium precursor to this synthesis procedure was the starting point for the preparation of the nano particle $V_2O_5/TiO_2$ catalyst.

The unoptimised synthesis of the nano-particular vanadia/anatase catalysts were prepared by hydrolysis of an acetous ethanol solution, containing titanium(IV) isopropoxide (97%, Lancaster) and vanadium(V) oxytriethoxide (95%, Aldrich), with an aqueous solution of ammonium nitrate (99.0%, Aldrich) forming solid seed crystals.
A typical preparation of the nano-$V_2O_5/TiO_2$ catalyst, the $Ti(OCH(CH_3)_2)_4$, $VO(OCH_2CH_3)_3$ and acetic acid mixture was first diluted in absolute ethanol and then cooled to 0 °C in an ice bath. The aqueous ammonium nitrate solution was then added drop wise to the ethanolic solution under magnetic stirring to forming a sol-gel. The molar ratio of the reactants were
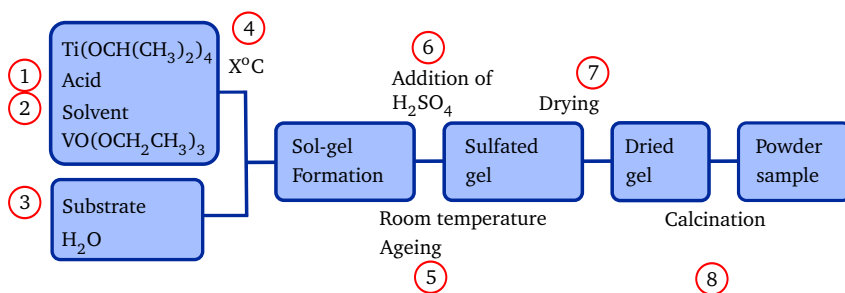
**Figure 4.1.:** *Procedure used to prepare titanium based nano-deNO$_x$ catalysts. Important synthesis steps and elements has been enumerated.*

adjusted to Ti:V:acetic acid:water:ethanol:ammonium nitrate = 1:x:2:15:30:2, where x was varied according to the desired amount of vanadium required to obtain catalysts with vanadia loadings between 5-25 wt.%. Subsequently, the sol-gel was aged at room temperature for 72 hours under stirring. Sulphuric acid was added to sulphate the titania and simultaneously remove acetic acid by esterification. Next, excess ethanol, water, acetic acid and liberated iso-propanol were removed under reduced pressure (12 mbar, 70 °C).

Finally, the remaining powder was calcined at 380 °C in an air stream (300 mL min$^{-1}$) to decompose the ammonium template and convert amorphous titania into crystalline anatase[103–105].

Through this chapter the optimisation of the synthesis will be described and each step will be evaluated by the impact it has on the synthesis. The general synthesis is illustrated in Figure 4.1 with each optimised step marked by encircled numbers .

In the following chapter the steps and elements of the synthesis that are listed below is evaluated and optimised:

①  Type of acid and amount

②  Different solvents

③  Amount and type of NH$_4^+$ salt: NH$_4$NO$_3$, NH$_4$Cl, (NH$_4$)$_2$SO$_4$ or (NH$_4$)$_2$CO$_3$

④  Gelation temperature

⑤  Ageing time

⑥  Influence of additional H$_2$SO$_4$

⑦  Method of drying and temperature
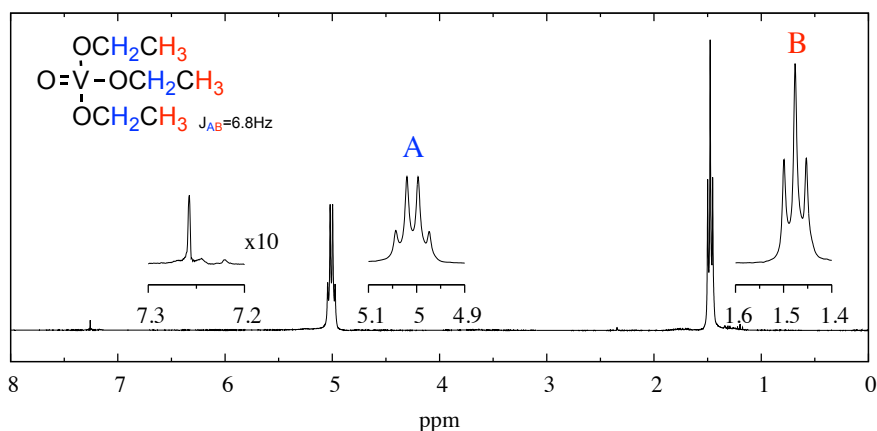
⑧  Calcination temperature and heating rate

**Figure 4.2.:** *300 Mhz $^1$H-NMR of synthesised ethyl vanadate in deuterated chloroform, with three key features highlighted. Solvent peak at 7.36 and trace amounts of ethanol and toluene respectively at 1.2-1.4 ppm and 2.35 ; 7.25 ppm.*

## 4.2. Vanadium precursor synthesis

Of all the chemicals used in the synthesis of the nano structured SCR catalysts, ethyl ortho-vanadate is the most expensive and the most difficult to obtain. In order to save money and increase the industrial value of the synthesis path, great effort has been put into synthesis of the vanadium precursor. Prandtl et al. showed in the early 1900 that compounds of the formula $R_3VO_4$, could be prepared from $V_2O_5$ and the appropriate alcohols [122], according the simple equation see 4.1 below.

$$V_2O_5 + 6ROH \longrightarrow 2R_3VO_4 + 3H_2O \qquad (4.1)$$
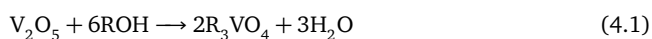
Other alkyl orthovanadates have not been tested for synthesis suitability in the thesis. Because Gilinski has shown that the ethyl orthovanadate is this most reactive precursor forming the most reactive monolayer. Lengthening of the n-alkyl chains leads to gradual decrease of its reactivity and the methyl derivate is not suitable, because it is a solid at room temperature and even less reactive [123].

The normal procedure for synthesis of ethyl orthovanadate, 600 ml ethanol and 600 ml toluene was mixed with 123 g of powdered $V_2O_5$ and distilled slowly through a 100 cm long vigreux column under a water free atmosphere at 1 atm. Water was removed as the ternary azeotrope (water-ethanol-toluene) boiling at 74.4 °C [114]. After 12 h of destination the mixture was cooled and vacuum distilled at room temperature to remove excess ethanol and toluene. To obtain pure ethyl orthovanadate the remaining $V_2O_5$ and product was distilled at 60 °C and 2 mbar, obtaining a typical yield around 20% or 55 g. The $V_2O_5$ powder can easily be reused in

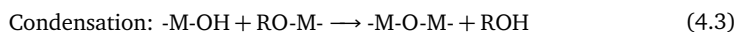another synthesis using fresh ethanol and toluene.

Purity was tested by ICP-MS and later by a simple reaction with water followed by calcination and weighing of the remaining $V_2O_5$. Both methods showed purities ranging from 96 to 100%. Complementary ^{1}H-NMR spectra of the synthesised ethyl orthovanadate showed one triplet (1.48 ppm) originating from the first three hydrogen on the ethyl chain (see **B** in Figure 4.2 on the preceding page) and a quartet (5.05 ppm) originating from the hydrogen on the second carbon (see **A** in Figure 4.2 on the previous page). The quartet is longer upfield compared to ethanol, due to the more negatively charged oxygen next to the vanadium(V) atom, which is to be expected matching Lachowics et al. ^{1}H-NMR observations [124]. This shows that the only species in the sample is ethyl orthovanadate with only trace amounts of ethanol (see 1.2-1.4 ppm) and toluene (see 2.35 and 7.25 ppm Figure 4.2), matching the results of the purity measurements.

This synthesis is very cheap and very easy to upscale, the only concern is safety due to the expected carcinogenic nature of vanadium pentoxide. However there are some disagreement of the toxisity of $V_2O_5$. The NTP[a] found the chemical carcinogenic [125], but the IARC[b] did not find sufficient evidence to label the chemical carcinogenic [126]. Depending on which report is relied on this has to be taken into consideration.

Ethyl orthovanadate can be stored in a closed container for up to 1 year before the chemical is notable polymerised. After polymerisation the vanadium precursor can still be used for synthesis of the nano SCR catalysts, only a very small decrease in activity has been observed.

## 4.3. Influence of acid in first step and solvent ① and ②

As earlier described titanium and vanadium alkoxides were used as precursors in the synthesis, reacting with water forming a mixed sol-gel of titanium- and vanadium- species. These reactions can be described as a hydrolysis followed by a condensation of a metal alkoxide precursor, see Equation (4.2) and (4.3), where M denotes a metal atom [127].

$$\text{Hydrolysis:} \quad \text{-M-OR} + H_2O \longrightarrow \text{-M-OH} + \text{ROH} \tag{4.2}$$

$$\text{Condensation:} \text{-M-OH} + \text{RO-M-} \longrightarrow \text{-M-O-M-} + \text{ROH} \tag{4.3}$$

Chemical additives such as solvent or acids have a huge impact on these reactions and the resulting sol-gel, but their role is not fully understood [128]. Likewise not much is known about the structure of alkoxides in the liquid state, only the structure of vanadium methoxide, which is a solid at room temperature has been solved [129]. Vanadium or titanium alkoxides of small primary alkoxides form oligomeric species via alkoxy bridging, but alkoxides of bigger and

---

[a]NTP National Toxicology Program in America

[b]IARC International Agency for Research on Cancer intergovernmental agency part of the World Health Organisation
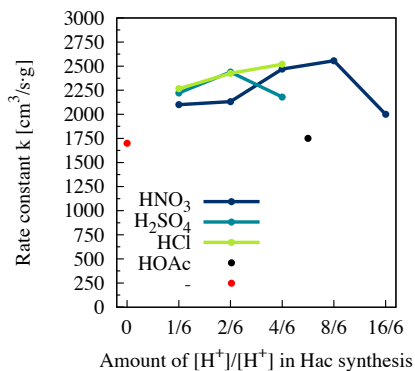
**Figure 4.3.:** *Activity measurements of 20 wt.% $V_2O_5/TiO_2$ catalysts at 380 °C synthesised with $NH_4Cl$ as seed and ethanol as solvent, without further sulphation, see step ⑥ and drying at 85 °C at atm. pressure step ⑦. The type of acid and the concentration has been varied to optimise the activity and surface area. The acid concentration is expressed as amount of [$H^+$] (this concentration is assumed equal to the amount of acid for strong acids) divided by the amount of [$H^+$] in a normal synthesis using acetic acid, described in Section 4.1 on page 33*
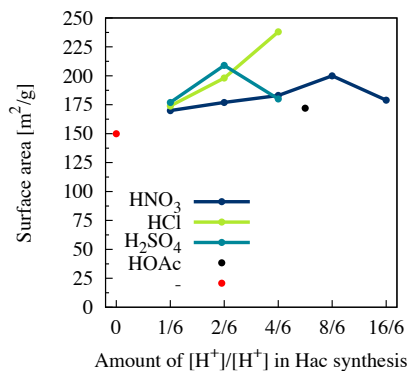
**Figure 4.4.:** *BET surface area as a function of the acid concentration expressed in amount of [$H^+$] divided by the amount of [$H^+$] in a normal synthesis using acetic acid. Each of the acids are denoted with a colour.*

more bulky alkoxy groups gives rise to monomeric species [124,127]. The bond is not very strong and can be cleaved when dissolved in a solvent changing the reaction time.

Consequently alkoxide reactivity can easily be modified by changing of a suitable solvent, nucleophilic molecules such as DMF, DMSO or even ROH can coordinate to the electrophilic metal, however other solvents have also proven to coordinate [128]. Furthermore alcohol interchange reactions also occur readily when vanadium or titanium alkoxides are diluted in a non-parent alcohol. In the latter case such solutions gives rise to mixtures of $[VO(OR)_{3-x}(OR')_x]$ species ( $VO(OR)_3$ dissolved in R'OH ). And by interchanging the alkoxy groups the steric hindrance can be decreased or increased leading to either faster or slower growth rate of crystallites [128,129]. Not only the growth rate is affected, but also the agglomeration tendency and crystallite size of the resulting crystals. Harris et al. [130] showed that hydrolysis of titanium ethoxide in tert-butyl alcohol yielded small, but agglomerated particles with high surface area. Whereas hydrolysis in methanol yielded big monodispersed particles.

Hung-Jen et al. [131] have shown that this knowledge can be used to choose a solvent to modify the crystallite size of the resulting anatase crystals using titanium isopropoxide as precursor. It was found that the resulting particle size varied in the following order depending on the solvent THF < Acetone < Butanol < Chloroform < Toluene < Hexane yielding anatase crystallites from 2.2 nm to 15915nm in diameter.

Gelation time can been controlled by adding a catalyst either acetic acid, hydrochloric acid or nitric acid, which decreases precipitation and thereby increases gelation time, thus changing the particle size[127,132].

Thus by changing the solvent and the amount of acid in the sol-gel the particle size and crystallite size can be optimised to maximise the surface area. Not only the anatase particle size has to be optimised, also the gelation time of vanadium ethoxide is of great importance. If the gelation time of the vanadium precursor is much faster than that of the titanium precursor, vanadium oxide particles can be formed first and then titanium will precipitate encapsulating them, hence giving a low activity due to the low amount of available vanadium sites.

After reviewing the importance of acid and solvent on a sol-gel and the resulting crystallites. The acid content was optimised in the ethanolic precursor solution or in case of $HNO_3$ and HCl the substrate solution. This was done by changing the type and concentration of the acids, see Figure 4.3 on the preceding page. In the figure acid concentration is expressed as $H^+$ availability (the three strong acids is assumed fully dissociated). Catalysts synthesised with 1 HOAc and 1 $HNO_3$ in the sol-gel have the same amount of $H^+$, but is added in a 46:1 molar ratio due to the weak nature of acetic acid. Originally the acid to metal precursor molar ratio of 2:1 were used for the sample with acetic acid, using $H_2SO_4$ this molar ratio is reduced to 1:69 at the optimum (see Figure 4.3 on the previous page at x=$^2/_6$). From Figure 4.3 it is clear that the amount and type of acid has a huge impact on activity. No addition of acid yielded a catalyst with low activity and just with small amounts of acid the activity was increased with up to 47%. From this optimisation it can be concluded that the optimum is at $^2/_6$, $^4/_6$ and $^8/_6$ respectively $H_2SO_4$, HCl and $HNO_3$. Regarding the poor performance of the catalysts synthesised with acetic acid it is a problem that the type of drying process influences the activity, for further information see Section 4.7 on page 48 and later in this chapter.

From the BET surface area as a function of amount of acid added it is clear that the surface area show approximately the same trend as the activity, see Figure 4.4 on the previous page. Indicating that an increase of acid concentration reduces the gelation time forming smaller crystallites, but also exhibits a negative effect when the acid is in great excess. This matches the observations of Livage et al.[127] concluding that acid can increase the gelation rates significantly.

In Figure 4.5 on the facing page several different measurements of catalysts synthesised with 8 different solvents and four acids adding up to 19 catalysts are depicted. Acid content was chosen on the basis of earlier described acid optimisations of a catalyst synthesised with ethanol, see Figure 4.3 on the previous page. The amount of solvent was held constant at a metal precursor to molar solvent ratio of 1:30 ($Ti_{pre}+V_{pre}$ : Solvent).

Only two catalysts were synthesised with acetic acid (HOAc) due to poor results, see Figure 4.5(a) on the facing page. This can be explained by the ability of the acetate ion to stick to
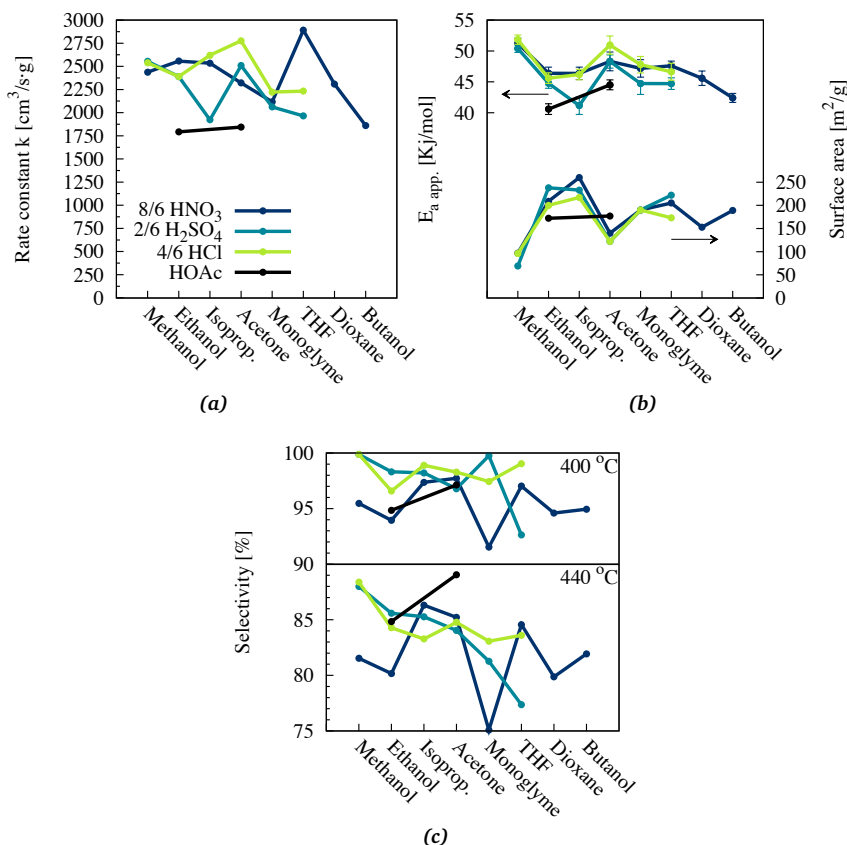
**Figure 4.5.:** *(a) Activity of catalysts at 380 °C, synthesised with four different acids $HNO_3$, $H_2SO_4$, acetic acid (HOAc) and HCl, and furthermore eight different solvents are used. All catalysts have been prepared with $NH_4Cl$ as the seed. Acid concentration is again expressed as $H^+$ availability. (b) Apparent activation energy of the catalysts are calculated from activity measurements. (c) $NO/NH_3$ selectivity of the catalysts at 400 and 440 °C.*

the surface of the catalyst. This results in a catalyst with acetate on the active centres after the drying step (see Figure 4.1 step ⑦). In the calcination step ⑧ acetate will then be oxidised resulting in reduced and carbon covered active centres. This can be observed by a change in catalyst colour from orange to brown and most important a low activity. This is further described in Section 4.7 on page 48.

From the surface area as a function of solvent it is clear that the solvent has a big impact on surface area and the choice of acid is less important in this regard. SEM images of the two extremes, the catalyst with the lowest and the highest surface area, the catalysts synthesised with methanol and tetrahydrofuran (THF) respectively. From these images it is obvious that the methanol sample is much more agglomerated than the THF sample. The TEM images of the same catalysts, see Figure 4.6 (c) and (d), show that the crystallite size is approximately
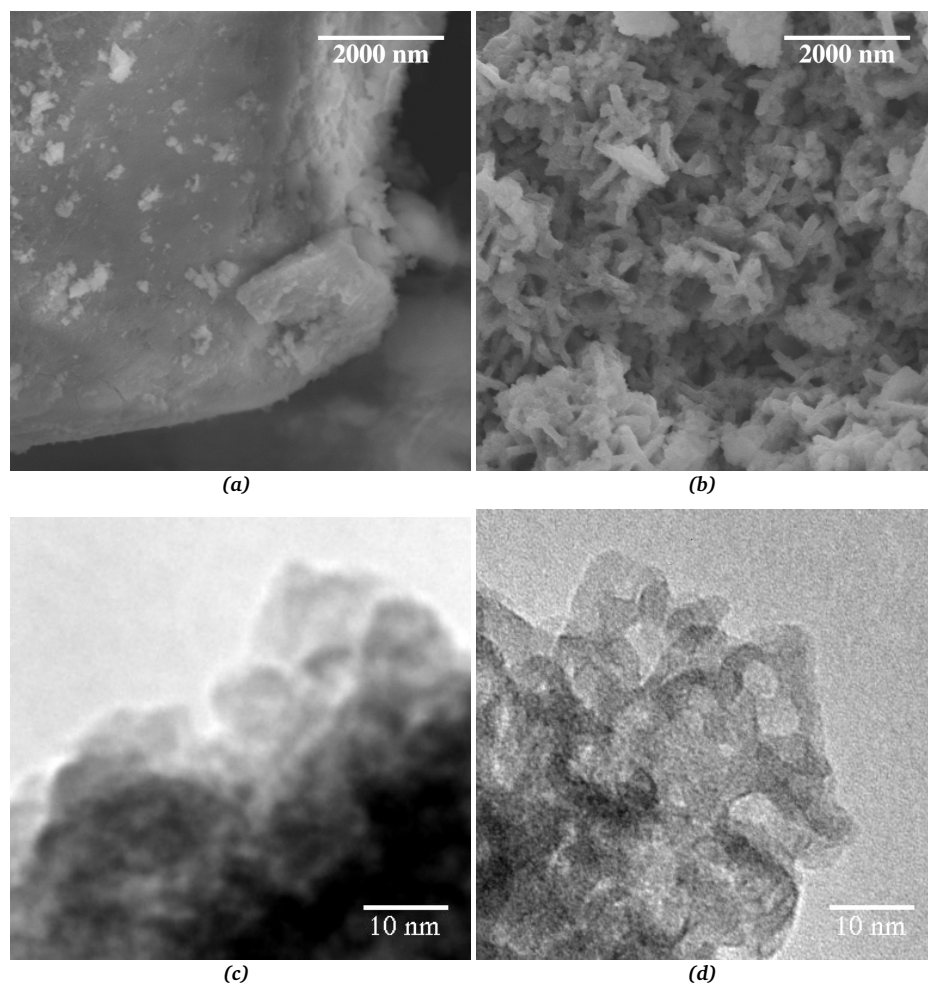
**Figure 4.6.:** *(a)* and *(c)* is respectively a SEM image and a TEM image of a catalyst synthesised with methanol and $H_2SO_4$. *(b)* and *(d)* is respectively a SEM image and a TEM image of a catalyst synthesised with THF and $HNO_3$

the same. So the agglomeration is on a macroscopic scale, like the earlier mentioned observation of Harris et al. using other solvents[130].

Even with much lower surface area of samples synthesised with methanol the activity is still very high, suggesting that the site distribution has changed. Assuming that there is only two types of sites A and B, A with low relative activity at 380 °C, low activation energy and low selectivity and active site B is then the opposite of A, see Figure 4.5 (a) ,(b) and (c). With B being polymeric overlayer species and A monomeric as suggested by Raman investigations that showed a change in vanadia sites depending of solvent, this is further discussed in Section 7.5 on page 97.

**Figure 4.7.:** *SEM image of a 20 wt.% $V_2O_5$/$TiO_2$ particle with EDX measurements highlighted, to the left Ti is marked with red and to the right V is marked with green.*

This can explain the behaviour of the methanol-synthesised catalysts, having higher activation energy, higher selectivity and higher activity relative to surface area, pointing to an increase of B. But unfortunately it is not that simple and all the catalysts; behaviours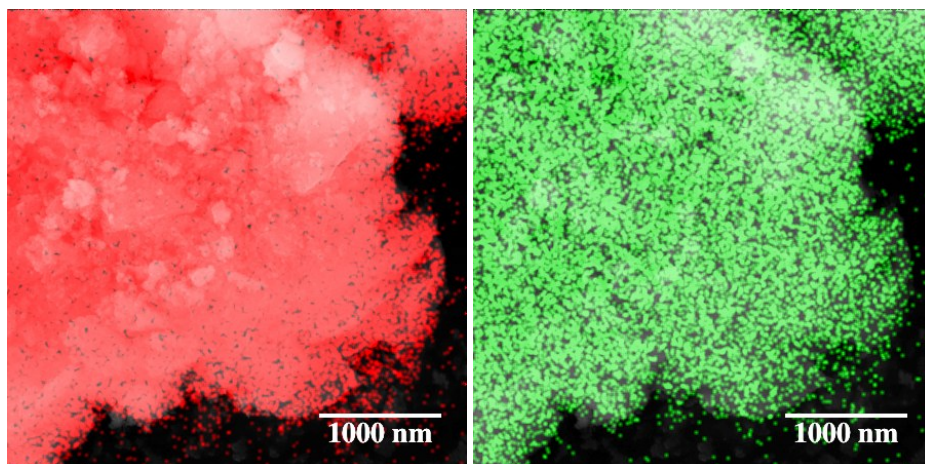 can not be explained by this assumption. Though looking at Figure 4.5(b) on page 39, there is a clear link between the surface area and the apparent activation energy. At low areas a high activation energy is observed, so low surface areas promote active sites with high activation energy.

Catalysts show no apparent correlation between, selectivity and activation energy or surface area. It can be argued that there is a tendency that at high activation energies a high selectivity is observed.

After these investigations it can be concluded that the solvent has an influence on both the surface area of the support and the type of active sites. This fits with earlier mentioned studies indicating that vanadium and titanium alkoxides easily can substitute and/or coordinate with solvents[128]. This can also be illustrated by liquid FTIR ATR of methanol and tetrahydrofuran mixed with vanadium ethoxide, respectively substituting and coordinating to the vanadium precursor, see appendix Figure B.1 on page 109. One could also argue that an explanation for the variation of activity, could be due to formation of large clusters of $V_2O_5$. But SEM/EDX measurements show an even distribution of vanadium throughout the sample, see Figure 4.7, but small clusters are not visible with the resolution of SEM/EDX.

Another important property of the solvent is the chemical stability, looking at THF it is obvious that the strong acids interact with the solvent changing it. It is well known that THF polymerises with strong acids[133], thus changing the solvent and hereby the synthesis con-

ditions. The calcination step ⑧ will then oxidise the formed polytetrahydrofuran resulting in reduced and carbon covered active centres, this is also described further for an ethanol / acetic acid catalyst in Section 4.7 on page 48. But this tendency is not as pronounced with easy evaporating solvents.

## 4.4. Structure directing substrate ③

Using different structure directing substrates yields different crystal sizes, hence different activities. Hari-Bala et al. showed that nano crystalline anatase ($TiO_2$) could be synthesised using $NH_4Cl$ and $NH_4NO_3$ as seeds[120,121]. Using $NH_4Cl$ yielded an average crystallite size of 7 nm, and use of $NH_4NO_3$ resulted in needle shaped crystals of 16-20 x 6-9 nm after calcination at 250 °C.

In Figure 4.8 on the next page 15 different catalysts synthesised with four different seeds, have been tested for SCR activity. Surface area and crystallite size is showed for catalysts synthesised with $NH_4Cl$ and $NH_4NO_3$ on Figure 4.9 on the facing page. All catalysts have been calcined at 380 °C and the syntheses have been performed using acetic acid and ethanol. From the change of crystallite size it is apparent that the apposite trend is observed compared to Hari-Bala et al.[120,121], $NH_4Cl$ yields bigger crystals than $NH_4NO_3$. But comparing SCR activity of $NH_4NO_3$ and $NH_4Cl$ catalysts with crystallite size show a direct correlation, lower crystal size yielding lower activity. This is very surprising, because normally smaller crystals produce higher activities, due to higher surface area. But surface measurements also show, that small crystals does not necessary lead to high surface areas. This can be explained by either, the lack of catalyst crystallinity throughout the sample and that the amorphous part changes particle size. Or that the zeta potential is lowered due to the change in substrate concentration, making agglomeration more pronounced, lowering the surface area.

Jiang et al.[134] observed a similar trend, the NaCl concentration of a $TiO_2$ nano particle dispersion in water changed the zeta potential, hence the stability of the particles resulting in agglomeration. But also the pH had a big influence on particle agglomeration, by bringing the pH close to the nano particle isoelectric point, which was shown to enhance agglomeration (pH = 7). This can explain the low activity of catalysts synthesised with $(NH_4)_2CO_3$, because $CO_3^{2-}$ is reacting with the available acid making the solution neutral enhancing agglomeration. The activity dependence of $(NH_4)_2CO_3$ can be explained by a reduction of pH to a neutral level and by addition of more $(NH_4)_2CO_3$ the pH increases, lowering the agglomeration. Due to this reduction of pH the catalysts synthesised with $(NH_4)_2CO_3$ performs even worse than catalysts synthesised without substrate, which have an activity of 1720 $cm^3$/s g, see Figure 4.3 on page 37.
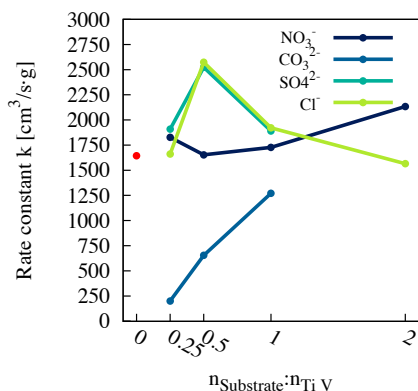
**Figure 4.8.:** *Activity of different 15 catalysts synthesised with four different ammonium salts and alternating amounts, the red dot represents a catalyst synthesised with out seed. The amount of ammonium salts are displayed as mole substrate divided by mole titanium and vanadium precursor.*
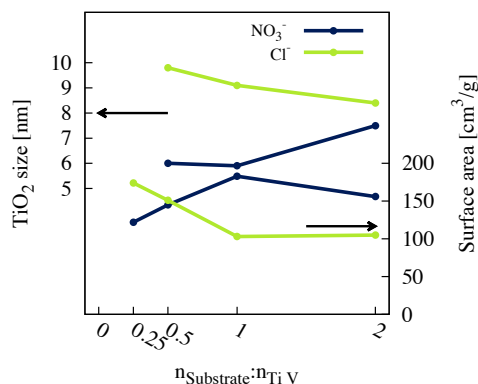
**Figure 4.9.:** *Change in crystallite size and surface area is depicted as a function of seed amount for the catalysts with $NH_4Cl$ and $NH_4NO_3$ from the plot on the left. All catalysts are synthesised as 20 wt.% $V_2O_5/TiO_2$ with acetic acid, ethanol and a second sulphation step.*

From the change in crystallite size in Figure 4.9 it can be concluded that $NH_4NO_3$ is stabilising the particles and decreasing crystal growth and $NH_4Cl$ is doing the opposite, but there is no apparent explanation for this behaviour.

$NH_4Cl$ and $(NH_4)_2SO_4$ are showing the same activity trends and have the highest activity maxima, hence either of the two substrates are preferred.

TGA measurements of the pure substrates and catalysts synthesised with different substrates, see Figure 4.10 and Figure 4.11 on the next page, show that the substrates tend to decompose at higher temperatures when added to the catalyst mixture. This makes the calcination more difficult for catalysts containing $(NH_4)_2SO_4$, because the high required calcination temperature (above 450 °C). At these temperatures the catalyst tends to agglomerate, loose the surface $SO_4^{2-}$ sites and form crystalline $V_2O_5$ due to lowered surface area. Resulting in a less selective and less potassium resistive catalyst. In order to make $(NH_4)_2SO_4$ catalysts work a careful activation at 440 °C in SCR gas had to be performed, prior to the activity measurements.

This "synthesis" step should be avoided, due to the cumbersome process. Mixing of substrates did not lower the required activation temperature. Because of this only $NH_4NO_3$ and $NH_4Cl$ can be used as substrates, in Figure 4.12 on the following page a optimisation of vanadium content is depicted. From the activity measurements it is clear that the optimum for both $NH_4NO_3$ and $NH_4Cl$ catalysts is at 20 wt.% $V_2O_5$. When choosing one substrate over another the potassium resistance has to be considered. The fresh $NH_4Cl$ catalyst is a little better overall, however looking at the potassium resistance there is a bigger difference between the two. The $NH_4Cl$ catalyst is approximately 1.5 times as good as the $NH_4NO_3$ counterpart.
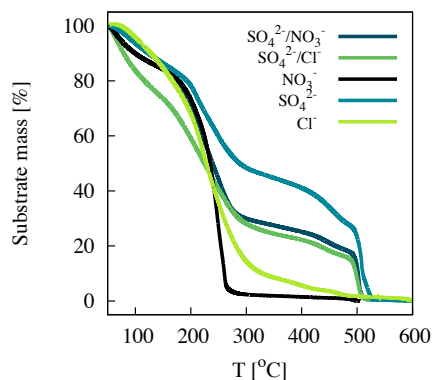
**Figure 4.10.:** *TGA of catalyst with different ammonium salts used as seeds prior to calcination.*
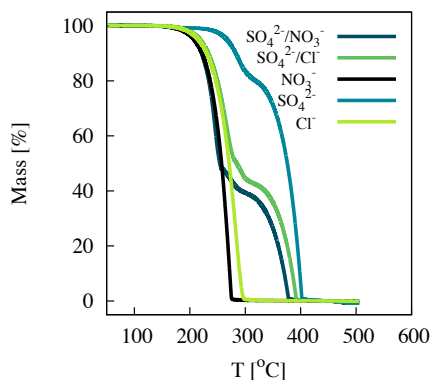
**Figure 4.11.:** *TGA analysis of the calcination of different catalysts synthesised with different ammonium salts.*
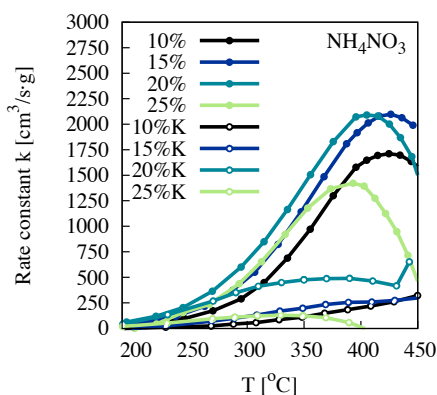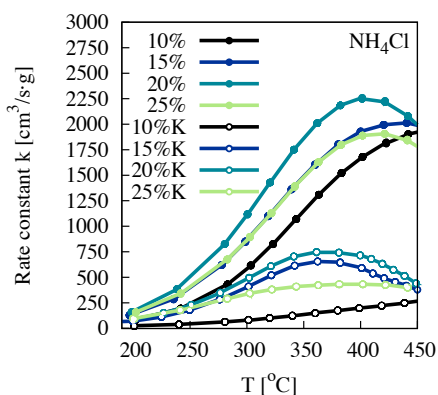


**Figure 4.12.:** *Activity measurements of a catalysts with different amounts of $V_2O_5$ synthesised with two seed salts $NH_4Cl$ **(left)** and $NH_4NO_3$ **(right)**. Catalysts denoted with a K is deactivated by 280 $\mu$mole/g $KNO_3$. All catalysts are synthesised with acetic acid, ethanol and a second sulphation step. The amount of $NH_4NO_3$ and $NH_4Cl$ seed is respectively 1 and 4 ($M_{Ti\ V}/M_{Substrate}$).*

From this it is clear that the best substrate is $NH_4Cl$ at a $n_{Substrate}$:$n_{Ti\ V}$ ratio of 1:4, yielding the most active catalyst. Though not the catalyst with highest surface area or lowest crystal size, which is surprising. The thermal stability of the two catalysts synthesised with $NH_4NO_3$ and $NH_4Cl$ are very different, see Section 6.3 on page 69, showing that the $NH_4Cl$ is much more stable at high temperatures. The higher thermal resistance of the $NH_4Cl$ catalyst can be explained by an increase in zeta potential due to adsorption of $Cl^-$-ions increasing the agglomeration temperature [135].
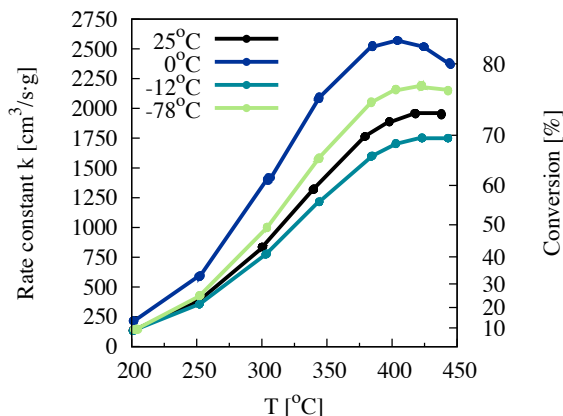
**Figure 4.13.:** *Activity dependence of gelation temperature* ④*. All catalysts are synthesised as 20 wt.% $V_2O_5/TiO_2$ with acetic acid, ethanol and a second sulphation step.*

After evaluating four different ammonium substrates it can be concluded that the choice of substrate is very important for the performance of the catalyst. Through evaluation of the four different structure directing substrates it was showed that using $NH_4Cl$ as substrate yields a more active catalyst and a catalyst with higher potassium and thermal resistance.

## 4.5. Temperature dependence of sol-gel formation ④

The sol-gel formation rate could have a strong temperature dependence, hence optimising the temperature at synthesis step ④ could have a big impact of the resulting catalyst. A change of the temperature will either make the gelation faster or slower, yielding smaller or bigger crystallites. In Figure 4.13 activity measurements of four catalysts synthesised with different sol-gel formation temperature is depicted. Activity of the four catalysts changes quite substantially when alternating the temperature. Yielding in an activity minimum synthesised at -12 °C and a maxima at 0 °C. This temperature dependence can be explained by a difference in gelation rate dependence of temperature of the two precursors and a difference between the melting points of the precursors. But there is no clear trend to explain the observed activities. From this investigation of the temperature dependence of the sol-gel formation it can be concluded that a gelation temperature of 0 °C is the optimum.

## 4.6. Ageing and addition of sulphuric acid - ⑤ and ⑥

Ageing of the sol-gel is important for the crystallite size, hence the surface area. Sharhini et al.[136] have shown that ageing after sol-gel formation enhances crystallite growth and decreases the surface area.

In Figure 4.14 on the next page activity measurements of four different catalysts obtained after ageing at 25 °C for different durations (step ⑤) are presented. The activity measurements show a decrease in activity with longer ageing, matching the observations of Sharihini et al., while assuming a lower surface area causes lower activity. Gelation time is therefore reduced to 4 hours instead of the original 72 hours, which increases the activity and decreases the waiting time during synthesis.

Another important step in the synthesis of the nano particle SCR catalyst is the second sulphation step (step ⑥). This step is increasing the acidity of the catalyst and thereby increasing the potassium resistance. Because sulphate acid centres will trap potassium and reduce the deactivation[7]. In Figure 4.15 on the facing page, the activity at 380 °C of 10 different catalysts are depicted. Each catalyst has been deactivated by incipient wetness impregnation to a potassium concentration of 280 $\mu$mole potassium chloride pr. gram of catalyst (the blue bar). Catalysts denoted with a S were synthesised with the second sulphation step ⑥ (optimised to 4.4 wt.% $H_2SO_4$).

From the initial activity of the second and third catalyst synthesised with $H_2SO_4$ in ethanol and with a second sulphation step, it is clear that the catalyst benefits from the additional sulphate. Resulting in an increase in activity from 2389 to 2550 cm$^3$/s·g , but it had an even bigger impact on potassium resistance. Here an increase of 15% in activity is observed, comparing with a catalyst synthesised without $H_2SO_4$ the benefits are even more pronounced, e.g. the ethanol catalysts exhibit very different potassium resistance depending on acid: $_{HNO_3}^{Ethanol}$ = 353 cm$^3$/s·g and $_{H_2SO_4}^{Ethanol\,S}$ = 589 cm$^3$/s·g - Figure 4.15. The only catalyst that did not benefit from additional $H_2SO_4$ in terms of increased potassium resistance, is the catalyst synthesised with methanol. This can be explained by the low surface area of the catalyst making the amount of $H_2SO_4$ it can accommodate much lower, resulting in a deactivation due to a sulphation of the active centres yielding lower activity and potassium resistance.

On the contrary the only fresh catalyst benefiting from the sulphation was the catalyst synthesised with ethanol, as the catalysts synthesised with acetone, THF and methanol deactivated. This can be explained by the instability of the solvents reacting with the added $H_2SO_4$, e.g. THF can polymerise as earlier described in Section 4.3 on page 36. In strong acids acetone also exhibit the ability to auto condensate[137]. The deactivation was also observed using only one acid step as earlier described and it was further enhanced by additional $H_2SO_4$, like it is observed with $_{H_2SO_4}^{THF}$ and $_{HNO_3}^{THF}$.
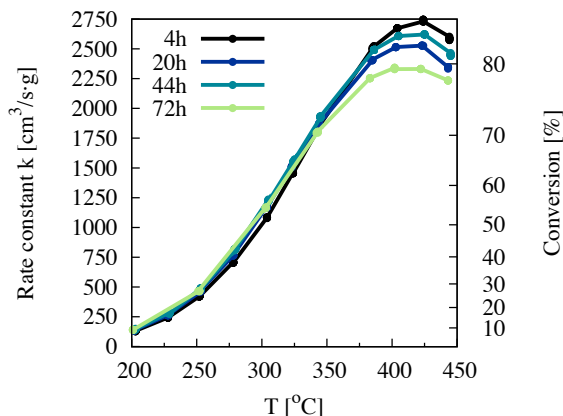
**Figure 4.14.:** *Ageing of gel before drying and calcination. All catalysts are synthesised as 20 wt.% $V_2O_5/TiO_2$ with $H_2SO_4$, ethanol and a second sulphation step.*
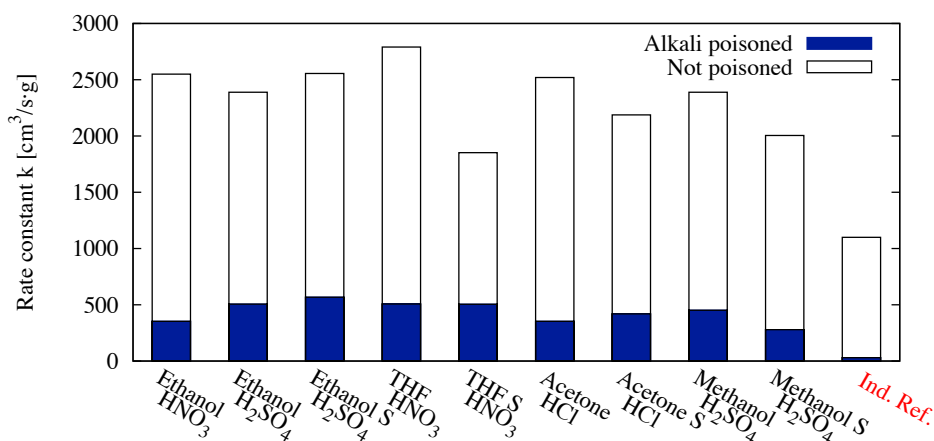


**Figure 4.15.:** *Activity at 380 °C of catalysts synthesised with different solvents with and without the sulphation step* ⑥ *(a S after the solvent denote that the catalyst are synthesised with the sulphation step) the white box represents the activity of a fresh catalyst and the blue box shows activity after an incipient wetness impregnation with 280 μmole/g of catalyst.*

Compared with the industrial reference catalyst all the catalysts were more active, between 1.6 and 2.5 times as active. This difference is further increased after deactivation, between 12 to 30 times as active. The most potassium resistant catalyst is the $^{\text{Ethanol S}}_{\text{H}_2\text{SO}_4}$ catalyst and are the second most active fresh after the $^{\text{THF}}_{\text{HNO}_3}$ catalyst. Due to the importance of potassium resistance, the $^{\text{Ethanol S}}_{\text{H}_2\text{SO}_4}$ catalyst is the optimal choice, while the $^{\text{THF}}_{\text{HNO}_3}$ catalyst would be the catalyst of choice in a coal fired plant. Furthermore THF is a much more expensive solvent compared with ethanol and when the catalyst is upscaled to industrial scale this is very important.

47
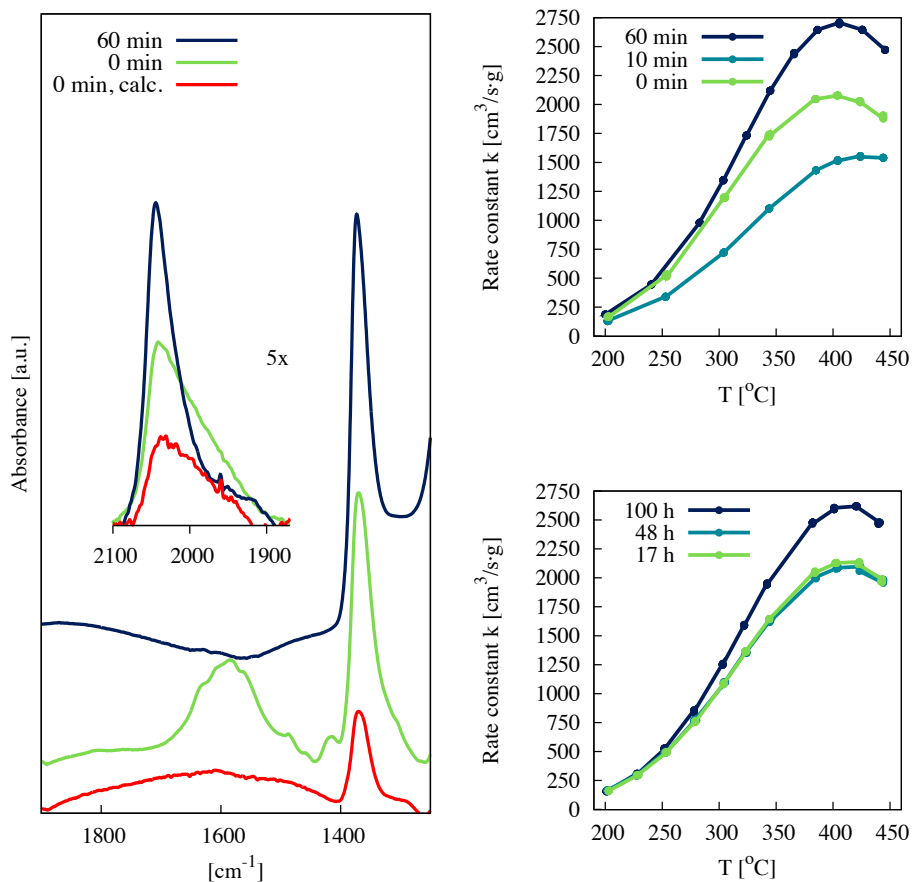
**Figure 4.16.:** *(Left) in-situ FTIR at 250 °C of catalyst exposed to a gas mixture (1000ppm NO, 3.5 % O₂ and He as carrier) one catalysts has been dried in vacuum for 60 minutes, and the other has not before calcination. The red line represents a catalyst calcined at 500 °C. (Top right) Three catalysts dried in vacuum for x minutes. (Lower right) Three catalysts dried in oven at 85 °C for x hours.*

## 4.7. Drying procedure ⑦.

Drying of the catalysts before calcination is an extremely important step, due to the possible deposition of organic chemicals on the catalyst surface. The organic residues will then deactivate the active centres occupying the surface, where ammonia otherwise would adsorb. Upon calcination the organic residue will be oxidised leaving a reduced and carbon covered catalyst surface. This has a big influence on the catalysts activity, see Figure 4.16 **(top right)**, three catalysts have been prepared with different degrees of drying, before the calcination step. At 60 minutes of drying in vacuum at 80 °C the optimum is observed, hence all the organic solvent and precursor residues are removed. Surprisingly the least active catalyst is the catalyst

dried for 10 minutes and not the undried catalyst. This could be due to up-concentration of the heavy organic residues, enhancing the reduction of the surface at calcination.

FTIR measurements of two catalysts illustrate the adsorbance of organics on the surface, one dried for 60 minutes and one calcined without drying, see Figure 4.16 on the preceding page **(left)**. The catalyst without drying showed several species on the surface in the C=O region. These vibrations are due to chelating acetic acid, as previously shown[131]. Active vanadyl species also show sign of deactivation due to adsorption of organic species. This is indicated by a downshift of the vanadyl stretch at 1900 to 2100 $cm^{-1}$, which is also observed when the catalyst is potassium deactivated, see Section 6.4 on page 71. One of the means to remove the organic residues is calcination, but it is first at 500 °C that the organic species are oxidised and removed. Calcination at these temperatures reduced the amount of observed vanadyl, due to the agglomeration of $V_2O_5$ forming clusters, in turn reducing the amount of surface vanadyl sites deactivating the catalyst.

Vacuum drying will be a very tedious and inconvenient way of drying in an upscaled process for the production of the catalyst. Therefore it is interesting to investigate different means of drying. A similar result to the vacuum drying could be obtained by drying in a ventilated oven at 85 °C for at least 100 hours, see Figure 4.16 on the preceding page **(lower right)**. This will make the production of large amounts of catalyst much easier, if the process is industrialised the drying step could be optimised further with more effective drying methods e.g. spray drying or drying in a rotary oven[138].

## 4.8. Calcination ⑧.

Another method to ensure the removal of organic residues before it is oxidised and the catalyst is deactivated, is to change the calcination temperature or heating rate. A calcination with a slow heating rate will allow the organic residues to evaporate before it is oxidised reducing the catalyst surface covering it with carbon, see Figure 4.17 on the following page. A calcination with fast heating rate (approx. 20 °C/min) results in a catalyst with lower activity compared with calcination with a slow heating rate. Which supports the idea of a deactivation due to carbon residues and organic species on the catalyst surface, as described in Section 4.7 on the preceding page.

This show that the optimal calcination was slow heating up to a desired temperature followed by calcination at this temperature, in this case 400 °C.

Figure 4.18 illustrates the importance of choosing a calcination temperature, too low and the catalyst was not crystalline and too high the crystal growth and agglomeration was too severe. At 380 °C the catalyst was still amorphous and not active. So this calcination temperature was too low if the catalyst was upscaled and there is no option to activate the catalyst at a higher
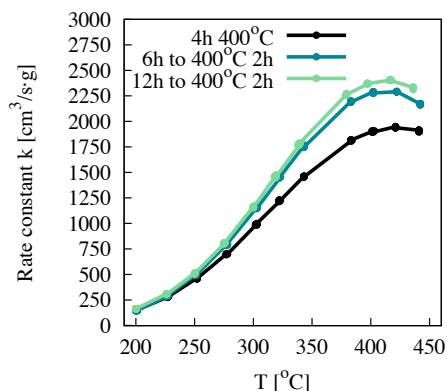
**Figure 4.17.:** *Different calcination methods quench heating to 400 °C and slow heating for 6 and 12 hours to 400 °C followed by a calcination of 4 or 2 hours.*
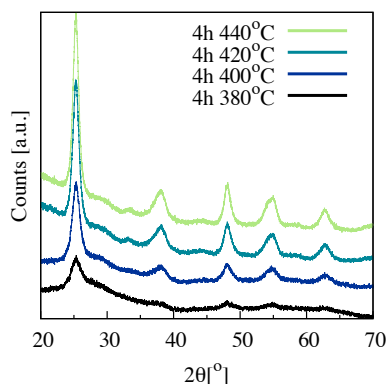
**Figure 4.18.:** *XRD of four catalysts calcined at different temperatures.*

temperature in SCR gas. At 400 °C the catalyst is more crystalline and comprises very small crystals, increasing the calcination temperature further increases the crystallite size. Temperature stability measurements showed that the increase in crystallite size did not deactivate the catalyst, see Figure Figure 4.17, but long calcination times at high temperatures is expected to deactivate the catalyst.

Thus from the activity measurements and XRPD data it can be concluded that the minimum calcination temperature ensuring a crystalline and active catalyst is 400 °C and a slow heating rate is preferred.

## 4.9. Alternative metal doping

The most widely used commercial SCR catalysts is based on vanadia/titania systems promoted with either molybdenum or tungsten - $V_2O_5-WO_3/TiO_2$ or $V_2O_5-MoO_3/TiO_2$. According to Chen et al.[29] there are several advantages of the tungsten promoter. Stabilising of the metastable anatase phase of $TiO_2$, increasing the temperature stability is one important effect. However also broadening of the operation temperature interval, increase of potassium resistance, decreasing the $NH_3$ oxidation activity and decreasing $SO_2$ oxidation are very important enhancements. Molybdenum exhibit some of the same promoting effects, but is less $N_2$ selective thus oxidising more $NH_3$, while on the contrary it is promoting the SCR activity more[139]. A catalyst with a $V_2O_5$ monolayer covered surface e.g. 20 wt.% $V_2O_5/TiO_2$ cannot accommodate a promoter, since all carrier surface sites are occupied. Therefore a 15 wt.% $V_2O_5/TiO_2$ catalyst was promoted with 15 wt.% $WO_3$ or $MoO_3$, see Figure 4.19 on the next page. Synthe-
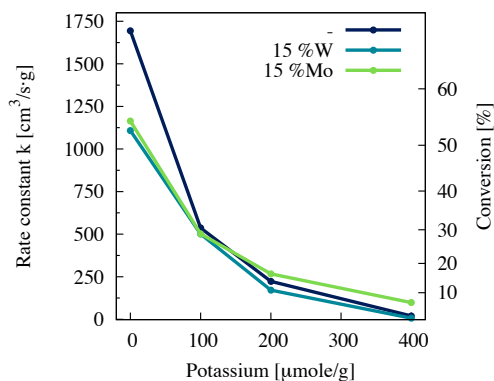
**Figure 4.19.:** *Potassium resistance of 15 wt.% Molebnium (Mo) or Tungsten (W) doped 15 wt.% $V_2O_5$/$TiO_2$ catalysts. Activity measurements are carried out at 380 °C.*

sis descriptions can be found in Appendix A.2 on page 107.

The promoted catalyst showed lower activity compared with an unpromoted catalyst, which is due to the formation of less active W or Mo centres and $V_2O_5$ clusters, caused by the lack of surface space. After deactivation by 100 $\mu$mole/g $KNO_3$ the three catalyst showed comparable activities with the unpromoted catalyst being slightly more active. At 200 $\mu$mole/g $KNO_3$ the $MoO_3$ promoted catalyst perform a little better than the unpromoted catalyst and at 400 $\mu$mole/g $KNO_3$ this is further pronounced.

The drop in activity of the fresh after the promotion is to high and the slight increase in potassium resistance is not big enough to compensate for the lost activity. So even at fairly low $V_2O_5$ concentrations the tungsten and molybdenum metals deactivate active surface centres. Therefore metal promotion of the final optimised catalyst are not used.

## 4.10. Concise conclusion

After optimisation of the 8 most important synthesis steps, a final procedure used to prepare the seed assisted sol-gel nano SCR catalyst can be formulated. The schematic of the synthesis can be seen in Figure 4.20 on the next page.

Sulphuric acid was chosen on the basis of activity measurements and potassium resistance. Ethanol was chosen over THF as solvent, due to price issues and that one-pot sulphation of the THF catalysts yielded worse catalysts. Without sulphation the potassium resistance was too low. After evaluating different structure directing substrates, $NH_4Cl$ was selected over the other three, due to higher thermal stability of the resulting catalyst and a low decomposition temperature of $NH_4Cl$. The optimal sol-gel formation temperature was 0 °C based on activ-
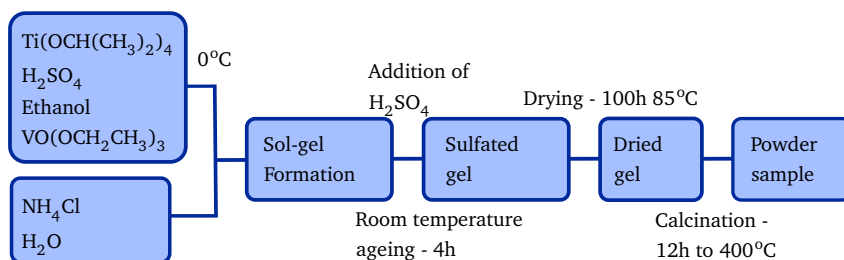
**Figure 4.20.:** *The final procedure used to prepare optimised titanium based nano-deNO$_x$ catalysts.*

ity evaluations. A short room temperature ageing of 4 hours showed highest activity and the potassium resistance could be enhanced with a second sulphation step. Drying was performed at 85 °C for 100 hours and followed by a slow calcination with a heating rate of 33 °C pr. hour to 400 °C, to ensure evaporation and not oxidation of organic residues. The optimised synthesis is performed as follows and the schematic representation of the synthesis can be seen in Figure 4.20.

The optimised catalysts were prepared by hydrolysis of an ethanol solution, containing $H_2SO_4$, titanium(IV) isopropoxide (97%, Aldrich) and vanadium(V) oxytriethoxide (95-100%), with an aqueous solution of ammonium chloride (99.0%, Aldrich). In a typical preparation the $Ti(OCH(CH_3)_2)_4$, $VO(OCCH_2CH_3)_3$ and $H_2SO_4$ mixture was first diluted in absolute ethanol and then cooled to 0 °C in an ice bath. The aqueous ammonium chloride solution was then added dropwise to the ethanolic solution under magnetic stirring to form a sol-gel. Molar ratio of the reactants was adjusted to Ti:V:$H_2SO_4$:water:ethanol:ammonium chloride = 1:0.22:0.17:15:30:0.5. Subsequently, the sol-gel was aged at room temperature for 4 hours under stirring. Sulphuric acid was added to further sulphate the titania (4.4 wt.% $H_2SO_4$). Next, excess ethanol, water and liberated isopropanol were removed by heating in a ventilated oven at 85 °C for 100 hours. Finally, the remaining powder was heated to 400 °C and held for 4 hours, at a heating rate of 33 °C pr. hour in stagnant air to decompose the ammonium template and convert amorphous titania into crystalline anatase. Calcination temperature was chosen to match normal maximum operating temperature of the SCR unit in a power plant (400 °C).

For a detailed description of a catalyst synthesis yielding 1.5 g catalyst, see appendix Section A.1 on page 107.

# 5

## Composite catalyst

In pervious chapters the catalyst investigations were done on small particles. Utilising these small catalyst particles under industrial conditions will result in a massive pressure drop and fly ash plugging. Therefore it is necessary to shape the catalyst into a monolith with honeycomb structure to avoid these problems. Due to the nature of the synthesis it is not possible to make a monolith using the sol-gel in a dip coating process. Alternatively, the dried catalyst powder can be mixed with a binder and shaped by extrusion or other methods. Such a binder can be clays like bentonite or sepiolite with adequate rheological properties and with pores providing a open structure. This chapter is devoted to the development of a clay catalyst mixture that can be used for making extrudates, going a step further towards industrial manufacturing.

## 5.1. Introduction

Extrusion of monolithic ceramic catalysts is a widely used technology in both the automotive and power plant industries to control $NO_x$ emissions [8,26,140]. Monolithic shaped catalysts are also used for other environmental applications, even chemical processing e.g. formaldehyde production [141,142].

Honeycomb catalysts used for control of $NO_x$ emissions from stationary sources consist of the catalyst, as described earlier ($V_2O_5$ on $TiO_2$), mixed with silica-aluminates and glass fibres as mechanical stabilisers. Wash coating of a silica framework with a suspension of a vanadium precursor, $TiO_2$ and a clay is one option to make the monolith. It can also be made by a dry mixing of the solid raw materials followed by addition of water and organic additives and finally extrusion of the monolith. After extrusion the monolith is dried uniformly to ensure that

**Table 5.1.:** *EDX measurements of powdered sepiolite and bentonite clays. The two samples denoted "washed" have been washed 2 times and dried at 200 °C prior to the measurement.*

|  | Bentonite [$wt.\%$] | Bentonite washed [$wt.\%$] | Sepiolite [$wt.\%$] | Sepiolite washed [$wt.\%$] |
|---|---|---|---|---|
| Na | 1.21 | 0.94 | - | - |
| K | 0.16 | 0.17 | 0.20 | 0.20 |

no cracks are formed and then calcined afterwards at 400-600 °C. In some cases $V_2O_5$ is added after the calcination by impregnation of the extruded monolith[140]. Each of the production steps are crucial and influence the quality of the final monolith. The solid components of the paste used to make a monolithic ceramic SCR catalyst are vanadia/tungsta/titania (90 wt.%), clays (6.5 wt.%) and glass fibres (3.5 wt.%) mixed with water and small amounts of methyl-hydroxy-ethyl-cellulose and poly-ethylen-glycol as organic additives[140].

Clays and glass fibres are used as inorganic binders that increase the mechanical strength of the monolith. Clays normally used are bentonite and sepiolite[140,143–148].

## 5.2. Sepiolite and bentonite materials

In this study both sepiolite and bentonite are used as binders. These clays are good binders for making extrudates.

Sepiolite is a hydrated magnesium phyllosilicate[a] with a fibrous morphology due to the molecular organisation of the sheets. The MgO sheets are terminated by hydroxyl groups and the tetrahedral silicate is linked by Si-O-Si bonds to an inverse unit. This structure induces needle shaped particles with large channels running parallel between the phyllosilicate ribbons. In hydrated form these channels are occupied by zeolitic $H_2O$, which upon heating can be removed. The dehydration is reversible when heating until 350 °C. Above 380 °C the sepiolite structure collapses and loses half of the structural water, and at 600 °C the anhydrous structure is obtained after a complete loss of zeolitic water. These phase transformations can vary for naturally occurring sepiolite[149–152].

Bentonite is an aluminium phyllosilicate, consisting mostly of montmorillonite with small impurities of e.g. potassium, sodium or calcium. Like sepiolite, bentonite consists of a layered structure with parallel sheets of tetrahedral silicate sandwiching a central octahedral sheet of aluminium. In this case the sheets of tetrahedral silicate are not linked to an inverse unit, but are continuous and the layers are only held together by Van der Waals forces. This makes the clay very brittle and water easily enters between the layers expanding the structure. The

---

[a]Phyllosilicate are sheet silicate minerals formed by parallel sheets of tetrahedral silicate. In the case of sepiolite octahedral MgO unit lie between the two sheets.
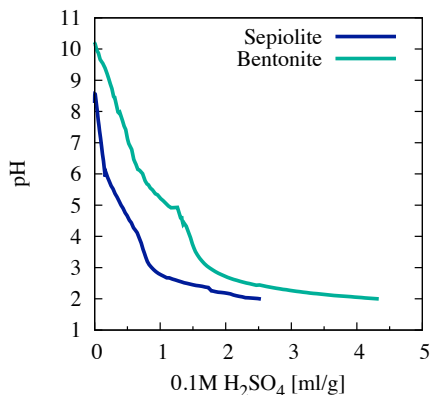
**Figure 5.1.:** *Titration of 1 g of bentonite and sepiolite clay suspended in water, using 0.1 M of $H_2SO_4$.*

bentonite easily dehydrates above 400 °C[153,154].

Both clays are naturally occurring and like many other clays they both contain considerable amounts of alkali metals. This also includes the clays used in these studies, see EDX measurements of sepiolite and bentonite in Table 5.1 on the facing page. Bentonite contains both potassium and sodium and sepiolite only potassium. Both clays were washed to investigate whether the alkali could be dissolved and deactivate the catalyst in the extrusion process. The sodium in bentonite is quite dissolvable, whereas the potassium in both clays showed no sign of any loss. This will be further discussed in the section below.

## 5.3. Sepiolite and bentonite extrudates and the effect of acid

Both sepiolite and bentonite are basic clays having a pH of 9 and 10 respectively when suspended in water, see (Figure 5.1). Because of the acidic nature of the catalyst mechanism it is important not to remove any acidic sites during shaping, which can be avoided by using acidified water used to make the extrusion paste. Furthermore, acidifying clays have other advantages; Knapp et al.[145] showed that it is possible to control the amount of $TiO_2$ at the surface of the resulting extrudate of a mixture of sepiolite and $TiO_2$ by changing the amount of acid in the water used for extrusion. They showed that the amount of surface $TiO_2$ would increase, by adding more HCl. This can be used to increase the activity of an extruded catalyst by increasing the amount of active catalyst surface. From these studies it can be concluded that it is beneficial to ensure a pH of at least 3. In order to determine the required amount of acid, the basicity of each clay must be determined.

By titration of sepiolite and bentonite, see Figure 5.1, it can be concluded that only a small amount of acid is necessary to change the pH of the extrusion paste. This acid could either be
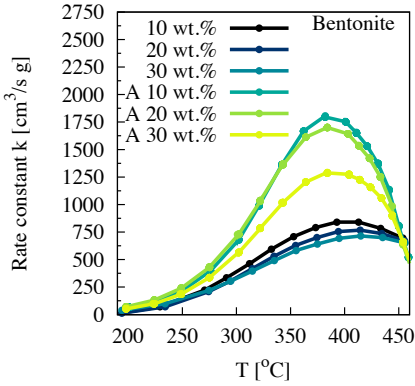
**Figure 5.2.:** *Activity measurements of bentonite extrudates comprising 10, 20, 30 wt.% bentonite and 20 wt.% $V_2O_5/TiO_2$ (synthesised without sulphation step ⑥, $NH_4NO_3$ and acetic acid) extruded with or without 0.05M acid, denoted A for 0.05M $H_2SO_4$.*

**Figure 5.3.:** *Activity measurements of sepiolite extrudates comprising 10, 20, 30 wt.% sepiolite and 20 wt.% $V_2O_5/TiO_2$ (synthesised without sulphation step ⑥, $NH_4NO_3$ and acetic acid) extruded with or without 0.05M acid, denoted A for 0.05M $H_2SO_4$.*

added to the catalyst prior to the mixing or in the water used for the extrusion paste. If the catalyst is acidic enough additional acid in the extrusion water is not required.

In Figure 5.2 and 5.3 activity measurements of extruded catalysts comprising either 10, 20, 30 wt.% sepiolite or 10, 20, 30 wt.% bentonite, respectively, and a 20 wt.% $V_2O_5/TiO_2$ synthesised with acetic acid, $NH_4NO_3$ and without the extra sulphation step, extruded with or without added acid. From these measurements it is evident that it is key to ensure acidic conditions when making a sepiolite or bentonite mixed catalyst. This observation can be explained by the earlier described mechanism of acid addition, whereby the acid increases the amount of catalyst at the surface, thus increasing activity of the catalyst. The amount of acid will be optimised in the preceding section, where a fully sulphated and optimised catalyst is used. Sulphation was obtained by synthesising with $H_2SO_4$ in the paste.

When comparing the activity of the bentonite composite catalysts with the sepiolite extrudates a slight advantage of using sepiolite is evident, which could be due to the lack of sodium in the clay as shown in Table 5.1 on page 54. Due to these observations sepiolite was chosen as the inorganic binder for further synthesis and for the making of the plate catalyst.

**Figure 5.4.:** *Extrudates made using the optimised 20 wt.% $V_2O_5$/$TiO_2$ catalyst and 0, 10, 20, 30, 50 wt.% and pure sepiolite (from the left).*

## 5.4. Catalytic performance and acidity and clay content

A series of extruded catalysts with mixed ratios of sepiolite and a optimised (see Section 4.10 on page 51) 20 wt.% $V_2O_5$/$TiO_2$ catalyst were synthesised with different concentrations of $H_2SO_4$ (0M, 0.05M and 0.25M) in the water used for making the paste. The extrusion process and synthesis is described more detailed in Section 3.3.2 on page 30, and a selected segment of the extrudates are depicted in Figure 5.4. The powder sample to the left is the pure nano-$V_2O_5$/$TiO_2$ catalyst and moving to the right the amount of sepiolite increases until 100 wt.% sepiolite at the right.

In Figure 5.5, Figure 5.6 and Figure 5.7 on page 59 are the activity of fractionated extrudates, respectively synthesised using 0M, 0.05M and 0.25 M $H_2SO_4$ in the water used to make the paste, are shown. These activity measurements show that the catalyst is not deactivated by 10 wt.% sepiolite in any of the cases, which is quite remarkable, since a drop of the activity of at least 10 % would be expected due to the increased mass. But the sepiolite is apparently increasing the activity by alteration of the pore size and thereby lowering of mass transport restrictions. Another explanations could be that some excess $V_2O_5$ is distributed on the new added sepiolite and thereby lowering the $NH_3$ oxidation, but selectivity measurements show no change of catalysts containing 10, 20 and 30 wt.% sepiolite. Only the 50 wt.% catalyst has higher selectivity, as seen in Figure B.9 on page 114 in the Appendix. The activity measurements also only show a slight change in $T_{max}$ (where the conversion has its maximum). The greater selectivity of the catalyst extruded with 50 wt.% sepiolite is observed by a higher activity maximum, which is above 440 °C because of the lower $NH_3$ oxidation.

By comparing the activities of the extrudates it can be concluded that using pure water with no added $H_2SO_4$ yields the best results contrasting the results from the previous section. This
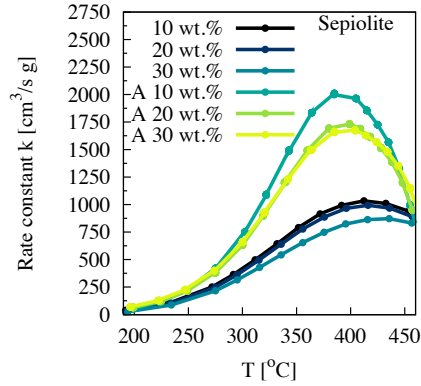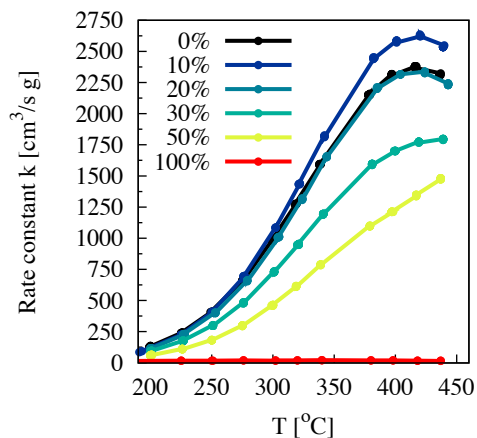
**Figure 5.5.:** *Activity measurements of sepiolite extrudates comprising 10, 20, 30, 50, 100 wt.% sepiolite and 20 wt.% $V_2O_5$/$TiO_2$ (optimised) extruded using water.*
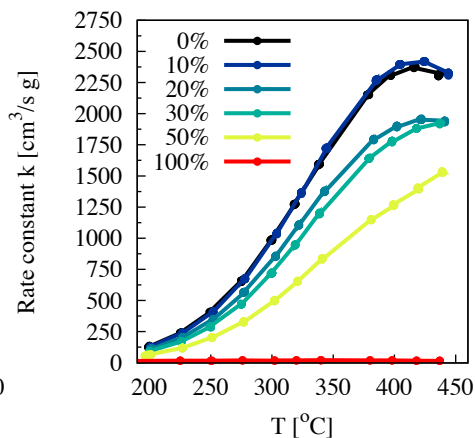
**Figure 5.6.:** *Activity measurements of extrudates with same ratio and synthesis method only 0.05M $H_2SO_4$.*

can be explained by the increased amount of $H_2SO_4$ present on the catalyst lowering the pH of the paste. At 30 wt.% the catalysts synthesised with 0.05M show better activities than those without additional acid, but only by a small margin. The activity gained by 10 and 20 wt.% sepiolite is again lost using 30 or 50 wt.%. The activity decreases faster than expected compared with the estimated activity calculated from the change in mass, illustrated by the redline in Figure 5.8 on the facing page.

This can be further investigated by $NH_3$-TPD, due to the basic nature of sepiolite it could be expected that sepiolite is decreasing the catalysts ability to adsorb and activate $NH_3$. The surface acidities of the composite catalysts were measured by $NH_3$-TPD and are depicted in Figure 5.9 on page 60. The $NH_3$-TPD measurements show several $NH_3$ desorption peaks below 400 °C. The first peak at 100 °C corresponds to physisorbed ammonia to weakly bound to be active in the SCR reaction under industrial conditions (320-380 °C). Peaks at 300 and 400 °C originate from desorption of chemically bonded and probably active $NH_3$ on acid sites. The change in acidity of the composite catalysts extruded using pure water resembles a potassium deactivated catalyst (compared within Figure 6.16 on page 73). A quite big decrease of the peak at 400 °C and a smaller decrease of the peaks below 400 °C are observed. The peak at 550 °C decreases and shifts to lower temperatures, which is interpreted as a small destabilisation of the sulphate on the surface, but not in the same degree as was observed when exposed to potassium. A broad peak at 510 °C is observed for the pure sepiolite sample, likely due to the desorption of strongly bound $H_2O$. This peak is observed in all the composite catalyst samples, and is increasing with increasing amount of sepiolite.

Increasing the amount of $H_2SO_4$ on the surface of the catalyst increases the acidity resulting

**Figure 5.7.:** *Activity measurements of sepiolite extrudates comprising 10, 20, 30, 50, 100 wt.% sepiolite and 20 wt.% $V_2O_5/TiO_2$ (optimised) extruded using a 0.25M $H_2SO_4$ aqueous solution.*
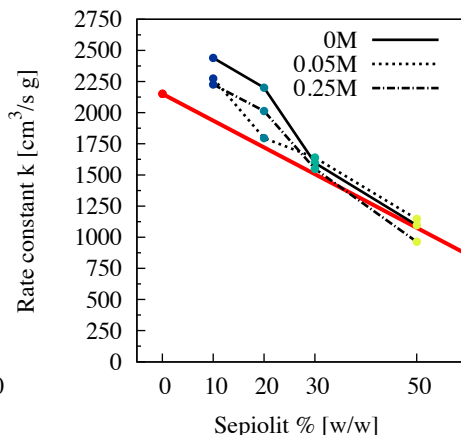
**Figure 5.8.:** *Activity at 380 °C of all sepiolite/20 wt.% $V_2O_5/TiO_2$ catalysts. The red-line denote the expected activity due to change in mass.*

in a lower decrease of the adsorbed $NH_3$. The adsorption peak at 400 °C is greatly increased, however the activity is not affected, as seen in Figure 5.8. This suggests that not all desorbed $NH_3$ at 400 °C is active in the SCR reaction or that the new sulphate acid sites are not active in the SCR reaction. But the increased acidity might increase the potassium resistance by attracting potassium lowering the amount of potassium reacting with the active acid sites. This is further investigated and discussed in Section 6.4.2 on page 74.

After evaluation of the composite catalysts a choice can be made on what composition exhibits the best qualities. A high amount of sepiolite will yield a catalyst with high durability due to the strength of the clay, but too much will lower the amount of active component and the resulting monolith will have a low activity. Based on the activity measurements the monolith should be made with 20 wt.% sepiolite and pure water, maintaining a high activity and a durable extrudate.

### 5.4.1. Plate catalyst

A plate catalyst was synthesised using the above formulation 20 wt.% sepiolite mixed with 20 wt.% $V_2O_5/TiO_2$ catalyst powder. The sepiolite and catalyst powder was thoroughly dry mixed prior to addition of water. To ensure a stable structure of the plate a base quartz mesh was
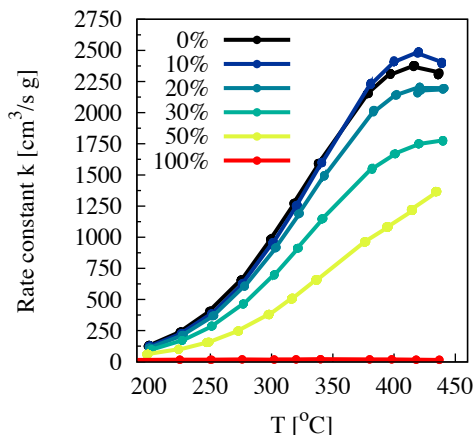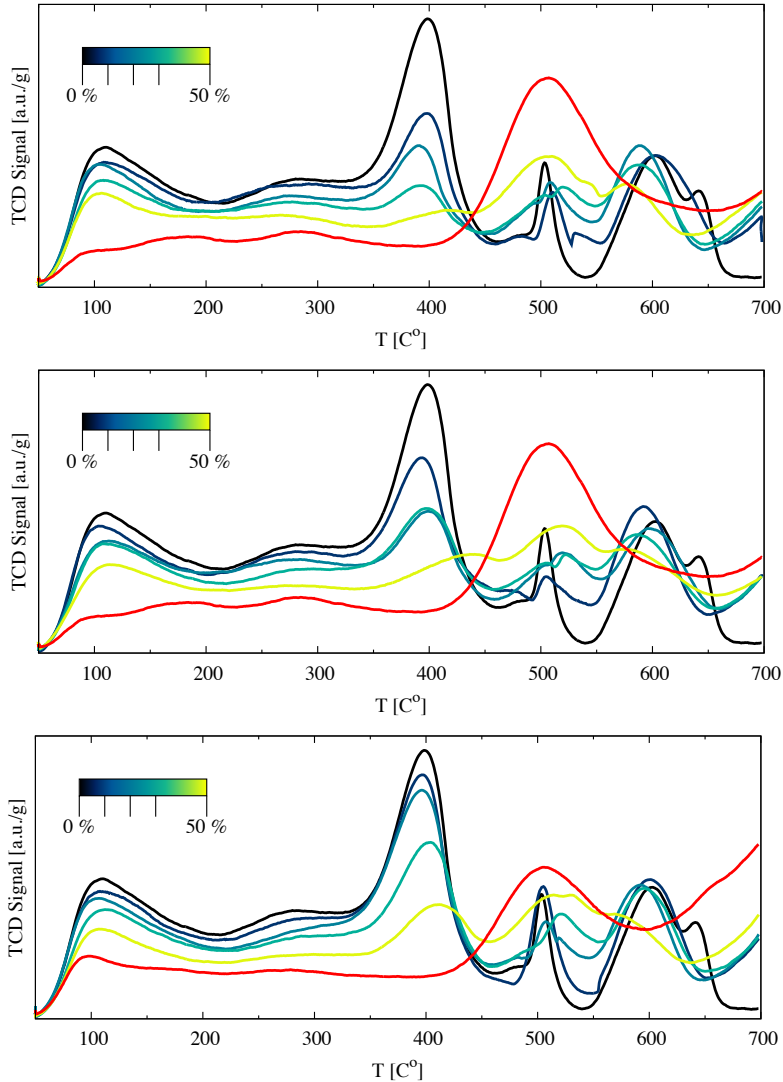
**Figure 5.9.:** *NH$_3$-TPD of sepiolite extrudates comprising 10, 20, 30, 50, 100 wt.% sepiolite and 20 wt.% V$_2$O$_5$/TiO$_2$ (optimised) extruded using water **(Top)**, 0.05M H$_2$SO$_4$ **(Middle)**, 0.25M H$_2$SO$_4$ **(Bottom)**. The pure sepiolite is marked with the red line.*

used on which the paste was applied. After drying in ambient conditions the plate was dried in a oven at 100 °C followed by calcination at 400 °C for 4 hours. A picture of the catalyst plate can be seen Figure B.10 on page 114 in Appendix. Small cracks can be seen on the surface which should be avoided by slower evaporation.
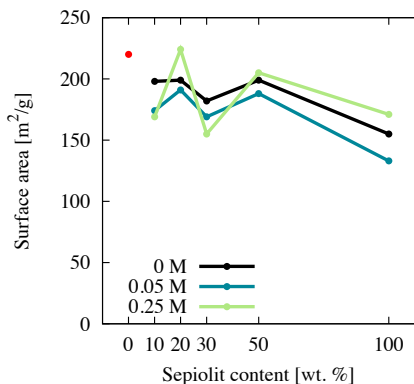
**Figure 5.10.:** *BET surface area as a function of sepiolite loading, extrudates made using 10, 20, 30, 50, 100 wt.% sepiolite and 20 wt.% $V_2O_5/TiO_2$ catalyst (optimised) extruded using water, 0.05M and 0.25M $H_2SO_4$.*
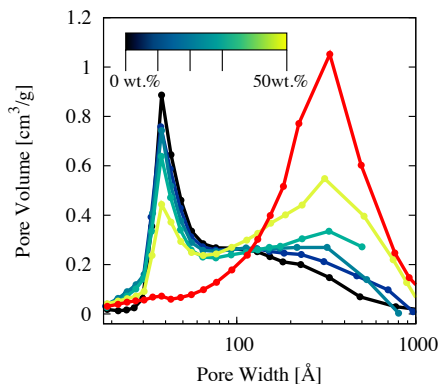
**Figure 5.11.:** *Pore distribution of composite catalysts extruded using pure water, measured by $N_2$ adsorption.*

## 5.5. Structural characterisation

Samples of catalysts synthesised with 10, 20, 30, 50, 100 wt.% sepiolite and pure water was characterised further using SEM, (see Figure 5.12 on the following page). The surface morphology changes from small individual particles of the 20 wt.% $V_2O_5/TiO_2$ catalyst (see Figure 5.12(a) on the next page) to fibrous particles held together by needle like sepiolite particles. Already at 10 wt.% the entire surface is covered by sepiolite, see Figure 5.12(b) on the following page. Increasing the sepiolite content alters the particles from sepiolite covered $V_2O_5/TiO_2$ catalyst particles to catalyst particles embedded in sepiolite fibres. It should be noted that at 20 wt.% and 30 wt.% the catalyst particles are at the surface of the agglomerates and exceeding 30 wt.% sepiolite the catalyst particles are inside the sepiolite structures, hence a decreased rate of mass transfer. This observation matches the activity measurements showing an activity decrease greater than expected from 20 wt.% to 30 wt.% sepiolite. The pure sepiolite can be seen in Figure 5.12(f) on the next page; larger particles comprising needle like sepiolite fibres. From the BET measurements depicted in Figure 5.10 it can be seen that the surface area is quite stable after the initial drop of 25 $^{m^2}/_g$ from the $V_2O_5/TiO_2$ catalyst to a 10 wt.% composite catalyst. The surface area of the sepiolite varies depending on the amount of acid using 0.05M $H_2SO_4$ lowers the surface area of approximately 15 $^{m^2}/_g$ regardless of sepiolite content. Increasing the acid content increases the surface area of some of the composite catalysts, 10 and 30 wt.% is lower. All three kinds of composite catalysts with varying acid content show a drop in surface area at 30 wt.%, which could be due to packing of catalyst particles with sepiolite. There is no direct correlation between activity and surface area, which
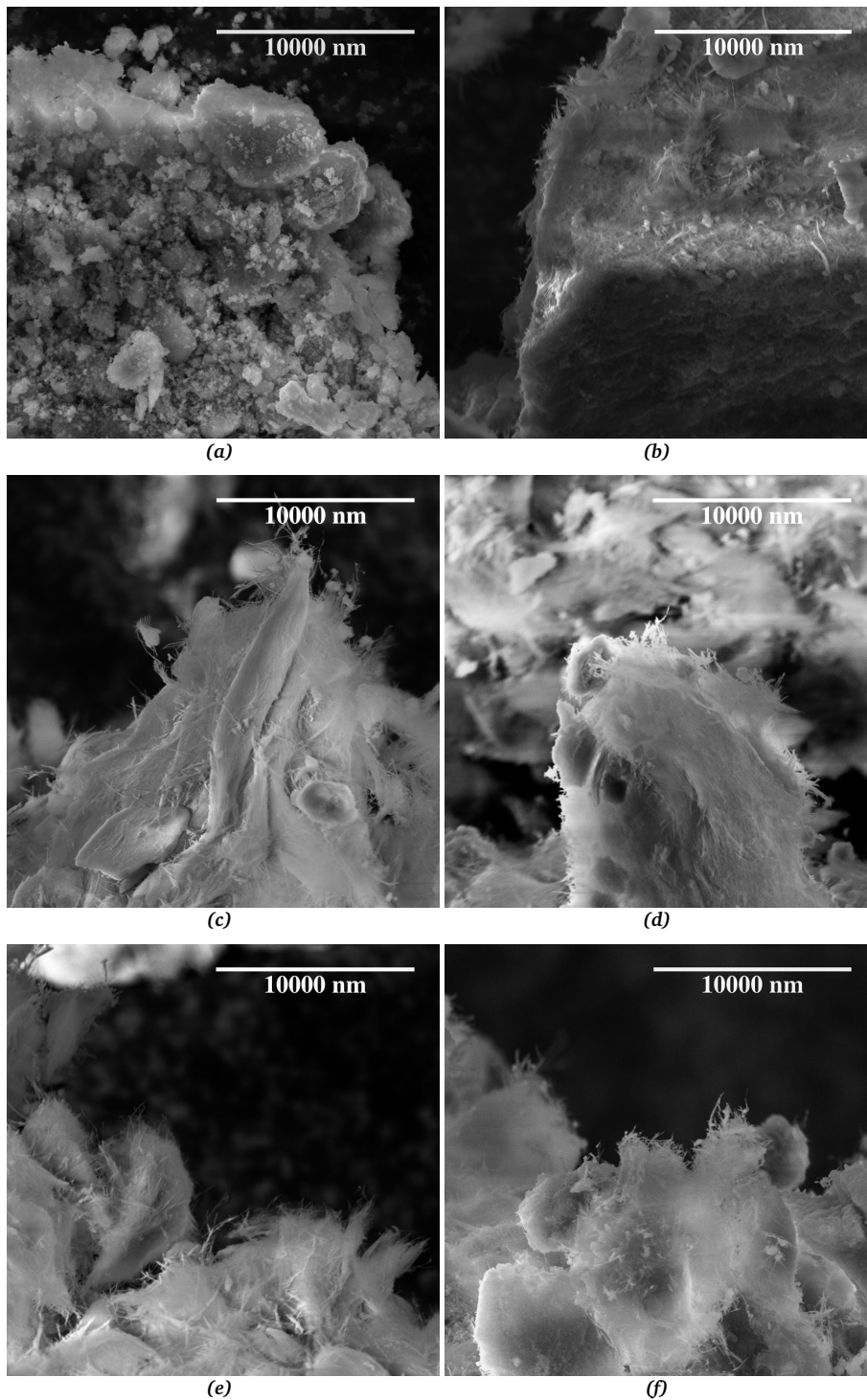
**Figure 5.12.:** *SEM images of selected composite catalysts synthesised using 10, 20, 30, 50, 100 wt.% sepiolite and 20 wt.% $V_2O_5$/$TiO_2$ catalyst (optimised) extruded using water,* **(a):** *20 wt.% $V_2O_5$/$TiO_2$ catalyst,* **(b):** *10 wt.%,* **(c):** *20 wt.%,* **(d):** *30 wt.%,* **(e):** *50 wt.%,* **(f):** *pure sepiolite*
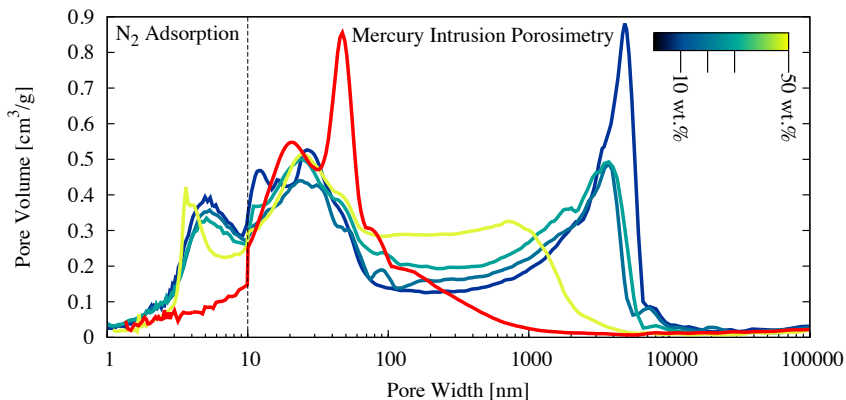
**Figure 5.13.:** *Pore distribution of composite catalysts extruded using pure water. 1-10 nm measurement is done by N$_2$ adsorption and the remaining pore width is done by mercury intrusion porosimetry. The pure sepiolite is marked with* **red**.

is quite surprising. This suggests that decreased diffusion is much more important than the total surface area.

The pore distributions of the composite catalysts are changing with increasing loading of sepiolite. The pure 20 wt.% V$_2$O$_5$/TiO$_2$ catalyst show no mesopores only micropores, increasing the sepiolite content to 10 wt.% increases the mesopores and decreases the micropores, see Figure 5.11 on page 61, this is due to the mesoporous structure of sepiolite. The fractions of macropores are decreasing with increasing loading, this is confirmed by SEM where we see a tendency that sepiolite fibres are filling the voids between catalyst particles forming larger more solid particles, see Figure 5.13.

This tendency is observed regardless of acid content, the pore distribution is only slightly affected by acid addition, see Appendix Figure B.11 on page 115. However the total pore volume decreases a little upon acid addition due to pore filling.

## 5.6. Concise conclusion

Increasing the content of the sepiolite inorganic binder in the composite catalysts provide beneficial effects in terms of physical strength and increase of macro pores decreasing the mass transport problems. It also decreases the catalyst activity pr. g of catalyst due to the increased mass, but furthermore it is deactivated by shielding of active sites. Adding acid to the extrudate paste was shown to be important and extensive deactivation due to shielding of active sites was avoided. Introducing this acid to the catalyst prior to extrusion yielded very active catalysts and subsequent adding of extra H$_2$SO$_4$ had very little effect. The activity of the composite catalyst was not effected by the increased acidity, though NH$_3$-TPD measurements showed a

difference. This increased acidity can maybe increase the potassium resistance, which will be tested in Section 6.4.2 on page 74.

BET and pore distribution measurements showed an increase of macro pores and a decrease of micro pores with increasing sepiolite content, matching the observed tendencies in SEM.

The most promising candidate of the composite catalysts with the best compromise between activity and physical strength is the 20 wt.% sepiolite extruded using pure water. This composite catalyst will be the basis for a plate catalyst used for potassium aerosol exposure in Section 6.4.2 on page 74.

# 6

## Deactivation and SCR under realistic conditions

This chapter is dedicated to potassium deactivation and realistic activity measurements of the optimised nano catalyst. Hereby showing that the catalyst is not deactivated in realistic conditions with a simulated flue gas containing NO, $NH_3$, $O_2$, He , $SO_2$ and $H_2O$. Furthermore the catalysts potassium resistance is tested by a gradually deactivation using potassium and compared to state of the art commercial catalysts. Catalysts with high $V_2O_5$ content have a tendency to oxidise $SO_2$, hence a section of this chapter is devoted to investigation of the $SO_2$ oxidation performance. Finally a catalyst plate has been exposed to a simulated biomass flue gas to measure the potassium deactivation in realistic conditions.

## 6.1. Activity in realistic conditions

In order to investigate the true capabilities of the nano catalyst, it has been exposed to a more realistic flue gas comprising NO, $NH_3$, $O_2$, $H_2O$, $SO_2$ and He. The activity setup used for the exposure is almost identical to the normal setup depicted in Figure 3.1 on page 27. However an alternative detector method was used, a Perkin Elmer Lambda 1000 UV/VIS spectrophotometer fitted with a gas cuvette heated to 150 °C. This was done due to possible deposition of ammonium hydrogen sulphate salts in the analyser. Thus an alternative detector method was used, to avoid deposition of salts and condensation of water. The peak corresponding to NO was used as a measure for the concentration, see Appenix Figure A.1 on page 108.

The gas flow composition during the activity measurements was 1000 ppm NO, 1100 ppm $NH_3$, 3 vol. % $H_2O$ and He as balance, in the case of added $SO_2$ the concentration was 2000 ppm and added $H_2O$ content was 2.4 vol. %.
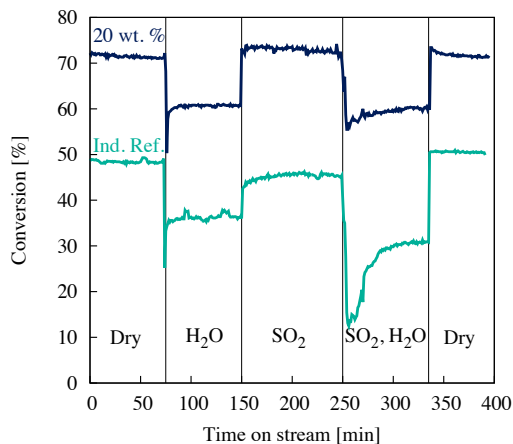
**Figure 6.1.:** *Activity of 20 wt.% $V_2O_5/TiO_2$ compared with an industrial reference at 380 °C. Activity was measured in He, $NH_3$, $O_2$ and NO - Dry and $H_2O$ or $SO_2$ were added.*
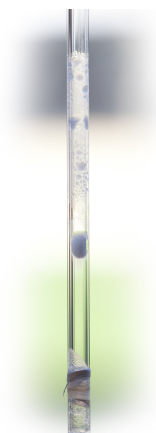


**Figure 6.2.:** *Picture of ammonium hydrogen sulphate formed during activity measurement in the reactor, just after the oven.*

All the tubes leading to the reactor were heated to 250 °C, due to the possible formation of ammonium hydrogen sulphate at low temperatures, see Figure 6.5 on the facing page. After the reactor it was difficult to avoid deposition of ammonium hydrogen sulphate, which made it impossible to measure the ammonia concentration, however the NO signal was not affected.

In Figure 6.1 the activity is plotted as a function of time at 380 °C. The vertical lines mark change of gas composition. The first 75 minutes of the measurement the catalyst is exposed to a dry flue gas identical to a normal activity measurement. No deactivation is observed in this short period. When the nano catalyst is compared with the industrial reference at dry conditions it is clear that the catalyst outperforms it, as expected, which also has been shown on several occasions already in the thesis. When $H_2O$ is introduced the activity drops 10-12 % for both catalysts as expected and described by several authors [155,156]. Thus the difference between the two catalysts are maintained and again no deactivation is observed.

After 150 minutes the $H_2O$ flow is closed and $SO_2$ is introduced, restoring the activity of the catalyst to just above the start activity at dry conditions, the industrial reference is 2-3% below the initial activity. A succeeding introduction of $H_2O$ lowers the activity to the previous level identical to the activity in humid SCR gas. An initial drop in activity is observed, which can be explained by formation of ammonium hydrogen sulphate in the tubes. This lowers the $NH_3$ concentration before the catalyst, decreasing the activity. Last segment confirming the initial activity again in dry flue gas demonstrating a high thermal and chemical stability of the 20 wt.% $V_2O_5/TiO_2$ catalyst. Displaying no activity loss due to $H_2O$ or $SO_2$ treatment and exhibits comparable resistance towards these gases as a state of the art commercial SCR catalyst.

Longer exposure times are desirable, but very difficult to obtain because of deposition of am-

**Figure 6.3.:** *Column for SO₃ absorption, heated to 80 °C by flowing water to avoid H₂O condensation.*

**Figure 6.4.:** *Titration of SO₃ containing washing solution of H₂O/iso-propanole with Barium perchlorate and a Thorin indicator.*

**Figure 6.5.:** *Flow setup with heated tubes before and after the reactor.*

monium hydrogen sulphate in the tubes after the reactor and in the gas cuvette, see Figure 6.2 on the facing page. Long-term activity measurements without $SO_2$ are fairly easy to measure and will be described later, Figure 6.10 and Figure 6.11 on page 70.

These measurements show clearly that the catalyst is not deactivated by $SO_2$ or a mixture of $SO_2$ and $H_2O$, as would be expected.

## 6.2. SO₂ oxidation

Combusting sulphur containing fuels such as oil and coal produces $SO_2$. A small fraction is oxidised in the boiler to $SO_3$, the remaining $SO_2$ can be oxidised over the SCR catalyst and this reaction is very undesired. Because $SO_3$ reacts with ammonia and water forming sulphuric acid and ammonium sulphates, either $NH_4HSO_4$ or $(NH_4)_2SO_4$ [17].

The ammonium sulphates can accumulate onto the catalyst at low temperatures causing fouling and plugging, hence a temperature of at least 300 °C has to be maintained [157]. Accumulation onto the air pre-heater downstream of the catalyst can cause severe corrosion and pressure drop.

Thus it is critical that a commercial catalyst combine a high activity towards the SCR reaction and a very low (almost negligible) activity in oxidation of $SO_2$. Forzatti et al. [158] showed that
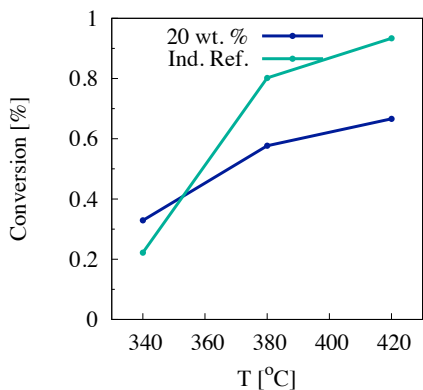
**Figure 6.6.:** *$SO_2$ oxidation activity of a 20 wt.% $V_2O_5/TiO_2$ compared with an industrial reference (3 wt.% $V_2O_5$ 7 wt.% $WO_3$ on $TiO_2$).*
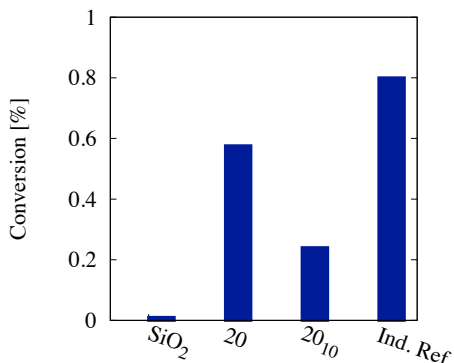
**Figure 6.7.:** *$SO_2$ activity at 380 °C of pure $SiO_2$ as reference and a 20 wt.% $V_2O_5/TiO_2$ catalyst compared with an industrial reference and a 20 wt.% $V_2O_5/TiO_2$ catalyst mixed with 10 wt.% sepiolite (denoted 20$_{10}$)*

the rate constant of the SCR reaction increases linearly with vanadia content on a catalyst, but the rate constant for the $SO_2$ oxidation increased exponentially with increasing vanadia content. This can be explained by a poor $SO_2$ oxidation activity of monomeric vanadia species and a higher activity of dimeric and polymeric species, which are similar to the active complexes in commercial sulphuric acid catalysts[159]. Accordingly a high dispersion of the surface vanadia must be attained by either low vanadia content or a second impregnation of tungsten or molybdenum as is seen on commercial catalysts to separate the vanadia sites and decrease agglomeration[29,139].

The working conditions influence the oxidation of $SO_2$ substantially. Tronconi et al.[160] showed that at a $NH_3/NO$ feed ratio $\alpha > 1$ the formation of $SO_3$ is reduced by a considerable amount. However a high $NH_3$ slip cannot be allowed and under normal industrial conditions $\alpha < 0.9$-0.95. At this $NH_3/NO$ feed ratio the oxidation is considerably reduced, but not to the same extent. Tronconi et al. developed a kinetic model predicting that the monolith can be designed with very thin walls and a large fraction of macropores to decrease the oxidation[158,160]. Hence every part of the catalyst design influence on the $SO_2$ oxidation.

Bearing this in mind, a test setup was developed, see Figures 6.3, 6.4 and 6.5. Where a catalyst (80 mg, fraction: 150-300$\mu$m) could be exposed to a flow of 300 $^{ml}/_{min}$ containing 2000 ppm $SO_2$, 3% $O_2$ and 2.4% $H_2O$ in Helium for 7200 min. All tubes were heated to ensure no condensation and the produced $SO_3$ was collected in an absorption column heated to 80 °C, to ensure no condensation of water. Next the absorption column was washed with a solution of 20 wt.% pure $H_2O$ in iso-propanole. The $SO_3$ content was then determined by titration using aqueous solution of barium perchlorate and a Thorin[a] indicator.

---

[a]Thorin is an indicator used in the determination of barium, beryllium, lithium, uranium and thorium compounds[161]
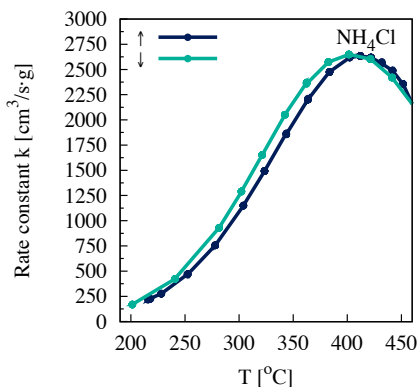
**Figure 6.8.:** *Activity measurement of 20 wt.% $V_2O_5/TiO_2$ catalyst synthesised with $NH_4Cl$ as seed,* **blue** *heating up and* **green** *activity after 440 °C.*
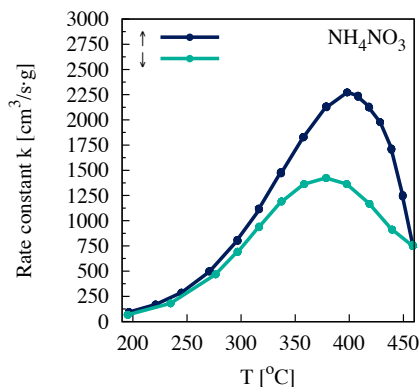
**Figure 6.9.:** *Activity measurement of 20 wt.% $V_2O_5/TiO_2$ catalyst synthesised with $NH_4NO_3$ as seed,* **blue** *heating up and* **green** *activity after 440 °C.*

In Figure 6.6 the conversion of $SO_2$ is depicted as a function of the temperature and remarkably the 20 wt.% $V_2O_5/TiO_2$ catalyst is oxidising less $SO_2$ compared to a 3 wt.% $V_2O_5$ 7 wt.% $WO_3$ on $TiO_2$ industrial reference. Furthermore comparison to a 20 wt.% $V_2O_5/TiO_2$ catalyst mixed with 10 wt.% sepiolite then extruded and fractionated, showed even lower oxidation at 380 °C, see Figure 6.7 on the facing page. This indicates that the sepiolite is distributing the $V_2O_5$ even better, which ensures a good dispersion and a low fraction of polymeric species on the surface. As expected pure $SiO_2$ is not active in the $SO_2$ oxidation and is used as a blank sample, showing that no $SO_2$ is adsorbed in condensed water giving a background value.

These results demonstrate that even with 20 wt.% of $V_2O_5$ on the catalyst, it is still very selective and $SO_2$ oxidation is not an issue.

## 6.3. Temperature stability

Temperature stability is very important and the catalyst has to withstand up to 380 °C for several years without deactivation due to sintering, or other temperature induced deactivation, for more information see Section 2.5.4 on page 23. In Figure 6.8 and Figure 6.9 two activity measurements are depicted, one for a 20 wt.% $V_2O_5/TiO_2$ catalyst synthesised with $NH_4Cl$ as seed and one with $NH_4NO_3$. The **blue** line is the activity heating up the catalyst and the **green** line is the activity after the temperature ramp to 460 °C.

Comparison of the two catalysts clearly shows that the catalyst synthesised with $NH_4Cl$ is much more resistant towards agglomeration at high temperatures, maintaining the activity after heating to 460 °C. Whereas the catalyst synthesised with $NH_4NO_3$ deactivates considerable
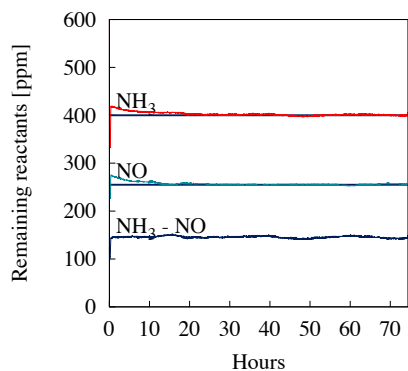
**Figure 6.10.:** *Measured activity at 380 °C for 70 hours in dry SCR gas. $NH_3$, NO concentration and $NH_3$-NO difference respectively denoted with the colors NH$_3$, NO and NH$_3$−NO*
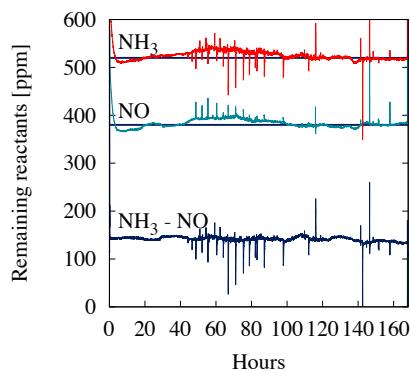


**Figure 6.11.:** *165 hours in humid SCR gas containing 2.4% $H_2O$*

due to the high temperature. 460 °C are far above the normal working temperature of a SCR catalyst, and as expected the same catalyst show no sign of deactivation at 380 °C for 75 hours in dry SCR conditions, see Figure 6.10. The concentration difference between $NH_3$ and NO is not changing, either proving that the vanadia sites are not sintering forming less selective polymeric vanadia sites.

These activity measurements were all carried out in a dry SCR gas, as all of the previously described measurements. As mentioned earlier in Section 2.5.4 on page 23, some catalysts show sign of deactivation due to $H_2O$. Figure 6.11 depicts the activity of the same catalyst as in Figure 6.10, but in humid SCR gas. The spikes are due to detection problems of the chemiluminisence detector in humid gas. Again the catalyst show no sign of deactivation even after 165 hours, the activity varies a little more than in the dry gas case. It can be assumed that this is due to the mentioned detection problems.
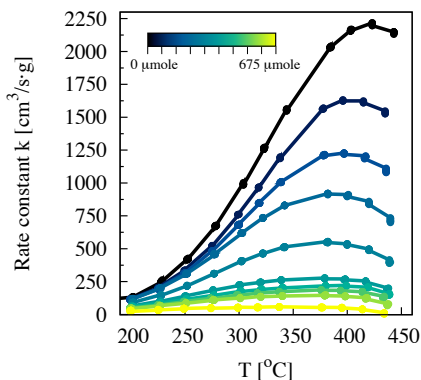
**Figure 6.12.:** *Activity measurement of a 20 wt.% $V_2O_5/TiO_2$ catalyst deactivated with different amounts of potassium (0-675 μmole/g in steps of 75 μmole/g).*
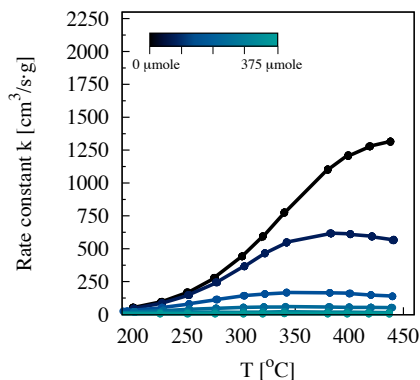
**Figure 6.13.:** *Activity measurement of industrial reference (3 wt.% on 7 wt.% $WO_3-TiO_2$) catalyst deactivated with different amounts of potassium (0-375 μmole/g in steps of 75 μmole/g).*

## 6.4. Potassium deactivation

In this section the optimised catalyst will be evaluated on the potassium resistance and compared with an industrial reference. First deactivation by incipient wetness impregnation using $KNO_3$ and later a more sophisticated potassium aerosol exposure will be applied to a catalyst plate and an industrial reference plate catalyst. These results can then be used to estimate the increased potassium resistance over the industrial reference catalyst.

### 6.4.1. Deactivation by impregnation

After optimisation of the potassium resistance by sulphation in Section 4.6 on page 46, it would be interesting to see the activity development as a function of deactivation compared with a commercial catalyst. This is done by incipient wetness impregnation, which is a "worst case" deactivation where potassium are forced into the catalyst and deactivates active sites as opposed to the study later discussed, where aerosols are passed over the catalyst.

In Figure 6.12 the activity development as a function of potassium doping depicted for a 20 wt.% $V_2O_5/TiO_2$ catalyst and an industrial reference in Figure 6.13. From this it is clear that the 20 wt.% $V_2O_5/TiO_2$ catalyst is more potassium resistant than the industrial reference on a $^{\mu mole}/_g$ basis. The activity maximum decreases slightly from 420 to 380 °C as a function of potassium concentration. The industrial reference (3 wt.% on 7 wt.% $WO_3-TiO_2$ anatase) show a similar trend merely with a larger shift from above 440 to 350 °C. This can be explained
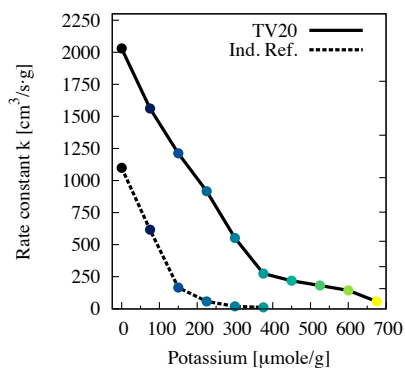
**Figure 6.14.:** *Activity at different potassium loadings at 380 °C of a 20 wt.% $V_2O_5$/$TiO_2$ and an industrial reference (3 wt.% $V_2O_5$ on 7 wt.% $WO_3-TiO_2$ anatase), done by IWI using $KNO_3$.*
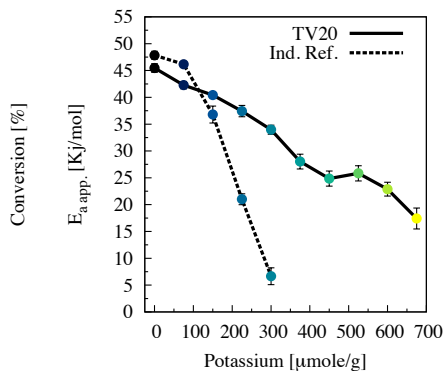
**Figure 6.15.:** *Apparent activation energy at different potassium loadings calculated from activity measurements depicted on Figure 6.12 and 6.13.*

by the decrease in selectivity, see Appendix B Figure B.7 on page 113. The selectivity decreases due to an increase in $NH_3$ oxidation. This suggests a change of the active sites upon potassium deactivation. The apparent activation energy is decreasing rapidly as well, this shows that the active sites are changing, due to the fast decrease in activation energy. The relative activity decreases more rapidly at high temperatures. Hence if the catalysts working temperature is low, the observed deactivation is a little lower as well.

Comparison of the potassium resistance of the industrial reference to the optimised nano catalyst clearly shows that the latter is much superior. The industrial reference is completely deactivated at 300-375 $^{\mu mole}/_g$, whereas the nano catalyst still has a k-value of 40 at 380 °C with 675 $^{\mu mole}/_g$ potassium. Activity of the fresh nano catalyst is considerably higher than the industrial reference providing an advantage of ca. 200 $^{\mu mole}/_g$ potassium, before the two catalyst exhibit the same activity.

The increased number of active sites, due to the high $V_2O_5$ loading, is responsible for the increased activity. In addition the increased potassium resistance and rate of deactivation is slightly lower for the nano catalyst. At 0-375 $^{\mu mole}/_g$ potassium (K/V=0-0.17) the deactivation rate is almost linearly decreasing, and then the deactivation rate decreases with a factor of 10 (K/V=0.17-0.3). This can be explained by a deactivation of the most accessible and active sites first and followed by a deactivation of less active and accessible sites. Assuming that the deactivation mechanism is as described earlier 1:2 in K:V - one potassium deactivate a dimeric site, see Section 2.5.2 on page 20. The amount of easy accessible vanadium (0-375 $^{\mu mole}/_g$) is approx. 34 % of the total amount, assuming constant deactivation rate. This is low, but due to the type of synthesis it is not surprising that not all the vanadia is attainable, contrary to a catalyst synthesised by an incipient wetness impregnation of $TiO_2$ with a vanadium precursor.
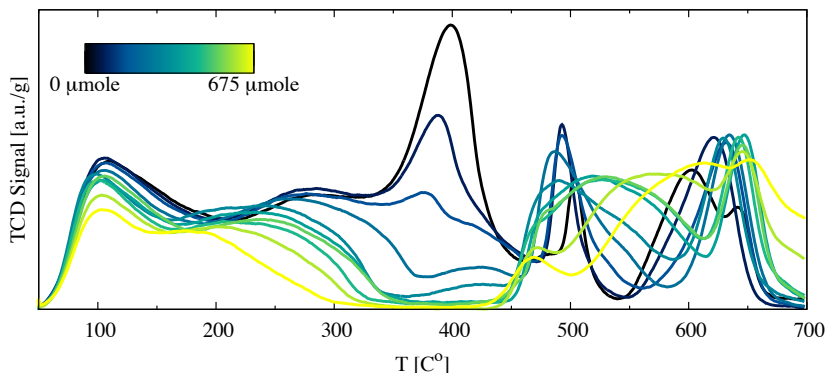
**Figure 6.16.:** *NH$_3$ TPD of the 20 wt.% V$_2$O$_5$/TiO$_2$ catalyst deactivated with different amounts of potassium (0-675 $^{\mu mole}/_g$ in steps of 75 $^{\mu mole}/_g$)*

Comparison of K/V ratios with the industrial reference is not viable due to the fact that it comprises not only TiO$_2$ and V$_2$O$_5$, but also the SCR active component WO$_3$. The industrial reference show a similar trend, a fast deactivation and then a much slower deactivation of the remaining sites, however it is not as pronounced.

NH$_3$ TPD is also showing that the surface acidity is decreasing, the first peak at 100 °C originating from weakly bound surface NH$_3$ is not affected much by potassium doping, but are showing a small decrease. These types of adsorbed ammonia are not active in the SCR reaction at realistic conditions, hence temperatures above 250 °C. This assumption fits quite well because there is no correlation between activity and the amount of NH$_3$ desorbed at these sites. The two following peaks originating from Lewis and Brønsted active acid sites are much affected by the potassium, showing a total removal of the peak at 400 °C and a large reduction of the peak at 270 °C. This shows that potassium is coordinating to NH$_3$ adsorption sites. Strongly bound ammonia at 500 °C, is also decreasing as a function of potassium doping.

All peaks above 550 °C is SO$_2$ or SO$_3$ due to evaporating sulphate species on the surface. A new broad peak is formed at 525 °C likely originating from destabilised SO$_4^{2-}$ sites on the catalyst surface. This is normally observed at 600-650 °C. The observation is supported by FTIR investigations described later, which shows a decrease in S-Ti bond strength, see Section 7.4 on page 93.

So the bond strength of the adsorbed ammonia is not changing upon potassium doping only the amount of NH$_3$ is decreasing, which indicate that the potassium adsorb at the same sites as ammonia and the resulting deactivated sites are not adsorbing NH$_3$. This is further supported by FTIR that shows only a decrease of Lewis and Brønsted adsorbed ammonia and not a shift of the peaks. Likewise the V=O group showed same trends upon potassium doping as adsorption of ammonia indicating that potassium react with these sites, see Figure 7.12 on page 95. But the mechanism of the SCR reaction is changing, hence the decrease of apparent activation
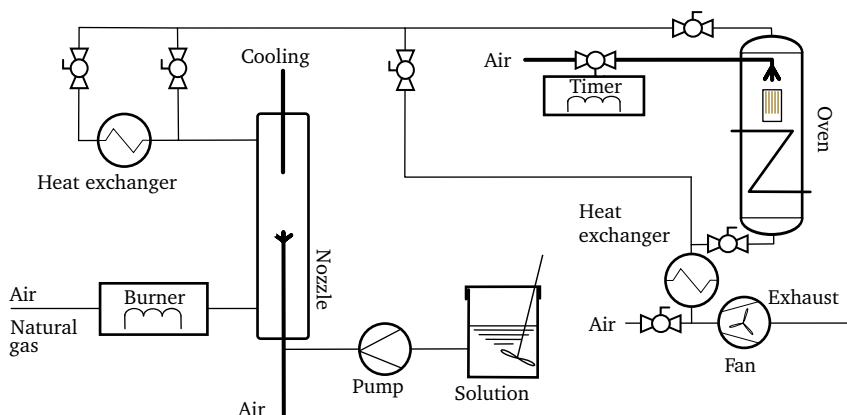
**Figure 6.17.:** *Schematic presentation of KCl aerosol exposure setup, comprising a 50kW natural gas burner, an aerosol generating fluid nozzle and a catalyst reactor with 9 slots holding 3×10 cm catalyst plates insulated and fitted with electrical heating, maintaining a temperature of 350 ±10 °C.*

energy. This can be due to a change of the active sites or a change of composition of types of active sites, e.g. monomeric, dimeric and polymeric sites.

### 6.4.2. Realistic potassium deactivation of catalyst plates

A more realistic approach to evaluate the potassium resistance of a catalyst is to expose it in an aerosol of potassium to model a biomass flue gas. This can be done by exposing a plate type catalyst in a pilot plant reactor, see Figure 6.17. Here the catalyst plate can be exposed to a well defined KCl aerosol, with an average size of 12 nm, see appendix Figure B.8 on page 113. In this setup hot flue gas was produced by a 50kW natural gas burner. The aerosol was generated by injecting 420 ml/h of an aqueous KCl solution (7.4 g/L KCl) through a fluid nozzle into the flue gas close to the burner at a temperature of 1053-1096 °C. A bayonet heat exchanger was inserted into the main duct downstream, to cool down the flue gas, see Figure 6.17. The catalyst reactor was fitted with a small catalyst cassette with 9 slots holding catalyst plates with the dimensions of 3.5×10cm, furthermore this reactor was well insulated and heated by an electrical heating wire to maintain the operating temperature of 350 ±10 °C with minimal temperature gradients. A soot blower above the catalyst plates was also installed to minimise plugging problems, blowing with compressed air every 30 minutes for 3-5 seconds. The total flow rate through the catalyst was kept at 38 ±2 $^{Nm^3}/_h$, which was adjusted by a bypass valve. The exposures were conducted for 632 hours. This setup has been used several times before with great reproducibility and success[90,162].

Figure 6.18 on the facing page shows the activity of the fresh fractionated catalyst plate com-
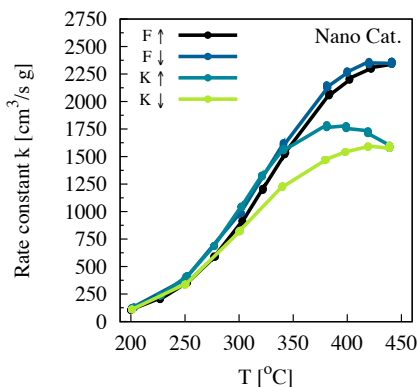
**Figure 6.18.:** *Activity of fresh fractionated catalyst plate, comprising 20 wt.% sepiolite and 20 wt.% $V_2O_5/TiO_2$ catalyst (heating up: black and cooling down: blue) and deactivated for 632 hours in KCl aerosol (heating up: cyan and cooling down: green).*
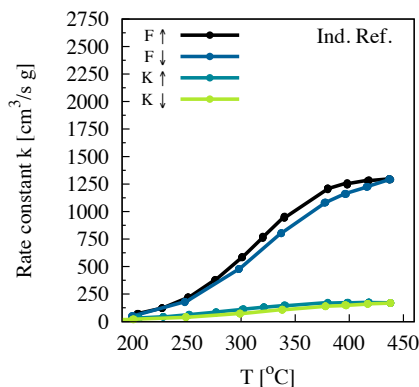
**Figure 6.19.:** *Activity of fractionated industrial reference catalyst with 3 wt.% $V_2O_5$ on $TiO_2$ (up and down) and deactivated for 632 hours in KCl aerosol (up and down)*

posed of 20 wt.% sepiolite mixed with a powdered 20 wt.% $V_2O_5/TiO_2$ catalyst and water (denoted $S_{20}V_{20}Ti$). In the same Figure an activity measurement after exposure in the aerosol setup is present. For comparison an industrial reference catalyst plate (3 wt.% $V_2O_5/TiO_2$ catalyst), has also been exposed and the activity of the fresh and deactivated catalyst is depicted on the Figure 6.19.

The ($S_{20}V_{20}Ti$) catalyst displays very low deactivation after 632 hours of exposure only deactivated 32% at 380 °C. Some hysteresis is observed due to the increased mobility of potassium at high temperatures, see Figure 6.18. The industrial reference in Figure 6.19 also shows some hysteresis. There is a vast difference compared to the industrial reference, which has suffered severe deactivation (84% at 380 °C) after the same exposure. These results are rather surprising, because a deactivation resembling the earlier mentioned impregnation studies was to be expected. These results show that the potassium aerosol particles have penetrated the industrial reference more easily than the ($S_{20}V_{20}Ti$), because the difference in rate of deactivation is higher compared with earlier results depicted in Figure 6.14 on page 72. The industrial reference shows deactivation corresponding to impregnation with 175 $\mu$mole/g and the ($S_{20}V_{20}Ti$) catalyst only 75 $\mu$mole/g. This is indicating that the penetration of KCl is twice as high for the industrial reference.

This demonstrates that the porous structure of the sepiolite is blocking the KCl from the active centres on the catalyst. It is illustrated in Figure 6.20 on the following page, where a SEM picture of a cross-section of the exposed ($S_{20}V_{20}Ti$) catalyst is depicted with elements highlighted with different colours. From this it is clear that the potassium sits on the surface of
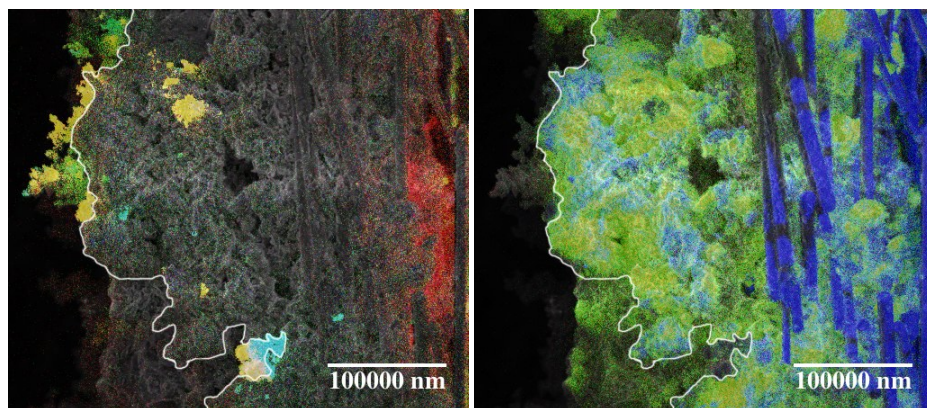
**Figure 6.20.:** *(Left) SEM picture with EDX information highlighted with different colours denoting elements,* **Cl**, **K** *and* **S**. *(Right) same SEM picture with EDX information of the elements,* **V**, **Ti** *and* **Si**. *The white line is illustrating the surface of the catalyst plate. If two elements are at the same place the two colours are added (KCl =* **K**+**Cl**=**KCl**).

the catalyst and only small amounts are penetrated the outer layer. The sepiolite is also fairly evenly distributed as it can be seen on Figure 6.20 **(right)** covering and protecting the catalyst. This is discussed in detail and pictures with greater magnification is shown, in (Chapter 5 on page 53). Vanadium is again evenly distributed in the catalytic active $TiO_2$, as previously shown, see Figure 4.7 on page 41.

The majority of potassium is present as KCl (**green**+**red**=**yellow**) and some as K (**green**) and $K_2SO_4$ (**turquoise**). The red signal on the right in the left Figure is a false signal and not due to chloride.

 In order to see if this deactivation is due to the chemical nature of the sepiolite or the physical blocking four catalysts were deactivated with 280 $\mu$ mole/g potassium by incipient wetness impregnation using $KNO_3$. One 20 wt.% $V_2O_5/TiO_2$ catalyst without sepiolite ($V_{20}T$) and three with 10 wt.% on a 20 wt.% $V_2O_5/TiO_2$ catalyst all extruded with different amounts of $H_2SO_4$ in the water were used to make the paste 0M, 0.05M and 0.25M, ($0MV_{20}T$), ($0.05MV_{20}T$) and ($0.25MV_{20}T$) respectively. The extra $H_2SO_4$ was added to increase the potassium resistance by making the catalyst more acidic.

In Figure 6.21 and Figure 6.22 on the next page, the activities of the deactivated catalysts are depicted. A slight advantage can be seen using 0M and 0.25M with sepiolite, however the difference is not great. Comparison of the composite catalysts with the pure $V_{20}T$, shows that the sepiolite is not changing the deactivation rate when impregnated with potassium. This indicate that the increased potassium resistance of the ($S_{20}V_{20}Ti$) catalyst is due to a physical blocking which prevents the potassium of reaching the active centres. Use of IWI avoids this physical blocking by capillary forces and almost all the potassium reaches the active centres of the catalyst.
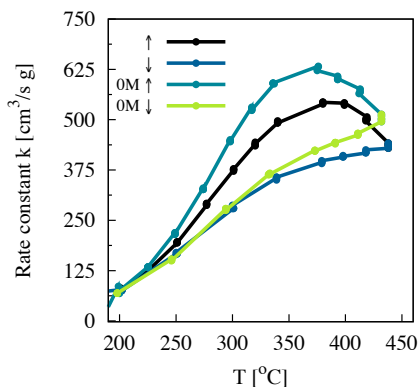
**Figure 6.21.:** *Activity of an extrudate comprising 10 wt.% sepiolite mixed with a 20 wt.% $V_2O_5/TiO_2$ catalyst and a pure 20 wt.% $V_2O_5/TiO_2$ catalyst, deactivated with 280 $^{\mu\,mole}/_g$ potassium by incipient wetness impregnation (heating up and down denoted with different colours).*
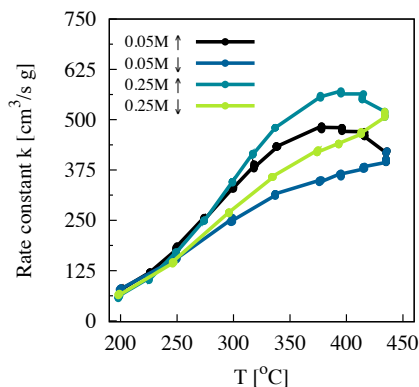
**Figure 6.22.:** *Activity of two catalysts comprising 10 wt.% sepiolite mixed with a 20 wt.% $V_2O_5/TiO_2$ catalyst and either a 0.05 M or 0.25M $H_2SO_4$ aqueous solution.*

## 6.5. Concise conclusion

Through this chapter the chemical and thermal stability of the catalyst has been tested, and no test showed evidence of deactivation, either due to irreversible sulphation of $SO_2$ gas or deactivation due to $H_2O$ induced sintering at 380 °C. Likewise a long exposure to SCR gas at 380 °C showed no deactivation, in neither humid nor dry conditions. More importantly the high $V_2O_5$ loaded catalyst showed no sign of enhanced $SO_2$ oxidation activity, compared with an industrial reference with a low $V_2O_5$ content.

The potassium resistance of the catalyst surpass the industrial reference with a factor of 2, before a total deactivation was observed. Realistic KCl aerosol exposures of a plate catalyst showed even higher resistance, due to the porous nature of the sepiolite binder. Further increase of the acidity of the composite catalyst, could not increase the potassium resistance significantly.

# 7

## Mechanistic studies

This chapter is dedicated to mechanistic studies of the nano catalyst using in-situ FTIR combined with already introduced measurements on the studied catalysts. In-situ $NH_3$ adsorption will be discussed under dry and humid conditions and the deactivation mechanism of potassium will also be investigated. These studies will shed light on the way the catalyst works and how it deactivates. The results will be summed up in a proposed SCR mechanism and a discussion of the potassium deactivation of a SCR catalyst. This new understanding of the system can then be used for development of new more potassium resistant and active catalysts.

## 7.1. Introduction

Using in-situ FTIR is a very effective method to get insight into the mechanistic aspect of a SCR catalyst. This method has been employed many times to investigate the adsorption and reaction of ammonia and nitrogen oxide [16,20,36,37,40–42,47,50,52–56,60–62]. Mechanistic investigations of the SCR reaction is reviewed in detail in Section 2.4 on page 14. The results of the FTIR investigations presented here will be compared with known proposed mechanisms and deactivation mechanisms earlier described.

### 7.1.1. Experimental

The in-situ FTIR investigations were carried out using a Thermo Scientific Nicolet iS5 spectrometer equipped with a specially designed in-situ reaction transmission cell, see Figure 7.1

on the next page. Catalyst powder samples were pressed at 6 $^{tonnes}/_{cm^2}$ into self-supporting disks which were cut to disks with an average diameter of 0.8 cm and a weight of approximately 8 mg, which were placed in the sample holder. The sample holder had two separate compartments, one dedicated to a standard for background measurements (normally just blank to measure the gas flow) and a self supporting wafer of sample held in place by two thin aluminium plates and a steel ring. During the measurement it was possible to take a background by raising of the sample holder arm, see Figure 7.1 on the facing page **(middle)**. Furthermore there was an inlet for SCR gases or other gas mixtures, which could be passed over the catalyst; it was placed just above the "blank" sample compartment. The in-situ cell was also equipped with a water-cooling system to avoid breakage of crystal windows due to thermal chock. Flow was maintained at a total of 128 $^{ml}/_{min}$. A SCR gas mixture comprises He 100 $^{ml}/_{min}$, $O_2$ 4 $^{ml}/_{min}$, 1% $NH_3$ in He 12 $^{ml}/_{min}$ and 1% NO in He 12 $^{ml}/_{min}$. The composition was varied depending on type of experiment. All experiments were conducted at 250 °C except for $NH_3$-TPD where the temperature was varied. The choice of operation temperature was based on FTIR study concluding that the species on the surface of the catalyst did not change from 250 to 440 °C. Moreover at 250 °C the noise to signal ratio much better than at high temperatures. Furthermore at 250 °C no or almost no $NH_3$ oxidation was observed. Flow rate was chosen to ensure a small SCR activity of the catalyst 15-20% conversion. The poor activity of the catalyst can be explained by a change in pore structure and the catalyst shape, which induces transport limitations and thereby lowers the activity[163]. Furthermore the design of the in-situ cell does not allow plug flow and it has a rather high dead space, which has a large impact on the conversion. Concentration of the remaining reactants was monitored online with a Thermo Environmental Chemiluminesence analyser model 17C. A linear background has been subtracted from all the spectra in the chapter to enhance the bands and increase the comparability between the spectra, the signal of $H_2O$, $NH_3$ and NO was reduced by subtraction of the respective gas spectra, see appendix Figure B.5 on page 111. In Figure 7.2 on the facing page three in-situ spectra of different samples are depicted to illustrate the different species in the catalyst, all measured at 250 °C and in a flow of He 112 $^{ml}/_{min}$, $O_2$ 4 $^{ml}/_{min}$ and 1% NO i He 12 $^{ml}/_{min}$. The full spectrum ranging from 800-4000 cm$^{-1}$, has been cut down into two parts to increase readability. This has been done on all the spectra throughout the chapter.

### 7.1.2. In-situ FTIR feature overview

Comparing the $TiO_2$ sample with the $V_2O_5/TiO_2$ catalyst sample show the $V_2O_5$ species absorptions at 1031 cm$^{-1}$ and the overtone at ∼2044 cm$^{-1}$ due to $\nu_{V=O}$ vibrations[36,40,41,54]. In addition $\nu_{V-OH}$ can be seen at 3650 cm$^{-1}$ [36,40,41,54] and a mixture of V-O-Ti and V-O-V vibrations can explain the increased absorption in the <900 cm$^{-1}$ range[164]. Strong absorptions due to sulphate species are also observed at 1129 and 1081 cm$^{-1}$ due to $\nu_{Ti-O-S}$ vibrations,
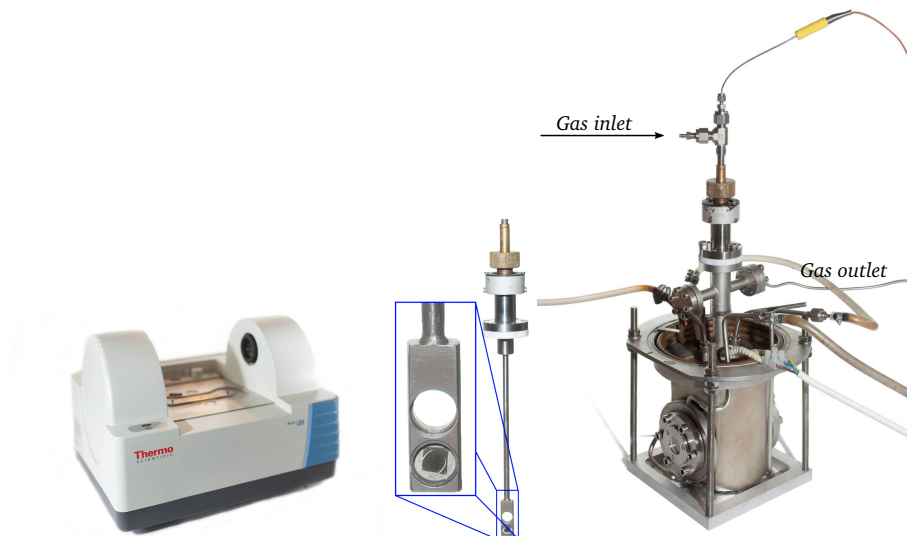
**Figure 7.1.:** *(Left) Thermo Scientific Nicolet iS5 spectrophotometer. **(Middle)** Pellet holder for in-situ cell with two compartments. One blank for background measurements and one for the self supporting sample wafer. By adjusting the height of the holder rod either the background or sample can be measured. **(Right)** In-situ FT-IR cell specially designed for pellet sized samples, equipped with ZnS (Cleartran) windows.*
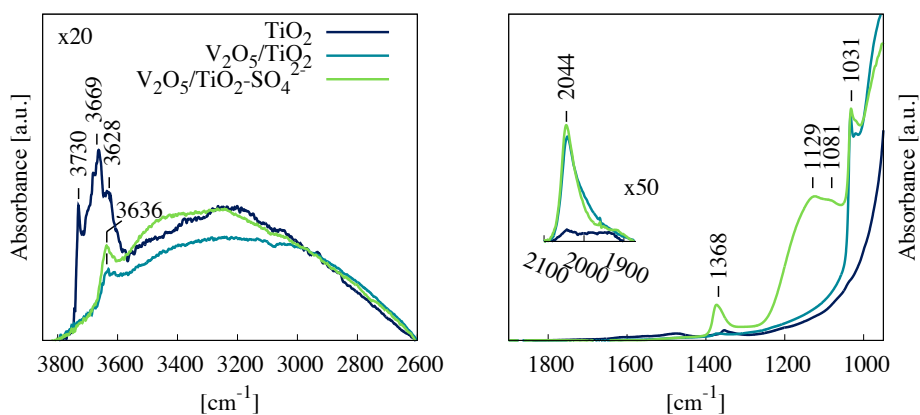


**Figure 7.2.:** *Spectra of three different samples, $TiO_2$, a $V_2O_5/TiO_2$ catalyst and a sulphated $V_2O_5/TiO_2$ catalyst. The spectra are divided into two for a better overview, the 1900-2100 region has been enhanced by multiplying by 50 and the 2600-3800 region by 20. Measured at 250 °C and in a gas mixture comprising 1000 ppm NO, 3.4% $O_2$ and He as carrier, with a total flow of 128 $^{ml}/_{min}$.*

these vibrations will be discussed later in detail, with the $\nu_{S=O}$ vibration observed at 1368 cm$^{-1}$ [165–167]. Three distinct Ti-OH bands are observed at 3730, 3669 and 3628 cm$^{-1}$. These bands are not observed when the catalyst is loaded with $V_2O_5$. Due to removal of the free Ti-OH groups which is replaced with surface V-OH and V=O [41]. The importance of the catalyst species will be dealt with later, first by in-situ FTIR measurements of a 20 wt.% $V_2O_5/TiO_2$ catalyst and later an analogous sulphated catalyst.

## 7.2. FTIR on nano structured an unsulphated 20 wt.% $V_2O_5/TiO_2$

In Figure 7.3 on the next page, a series of spectra are depicted of an unsulphated 20 wt.% $V_2O_5/TiO_2$ catalyst. All measured under different conditions to investigate how the SCR reactants are interacting with the catalyst surface. The two spectra from the bottom are measured under He, $O_2$ and NO with or without water. No bands originating from NO was observed indicating that NO is not adsorbed on the catalyst surface. This observation is identical to the measurements of many authors and it is generally accepted that NO is not adsorbed or only very weakly adsorbed on the surface. [40,41,54]. On the contrary water adsorbs on the surface of the catalyst, resulting in $V-OH_2$ vibrations at 1609 cm$^{-1}$. This band has been regarded as Lewis adsorbed $NH_3$ several times due to the adsorption of such a species at 1603 cm$^{-1}$ [4,16,37,41,54,168]. In very dry conditions this band can be used, but introducing NO to the gas mixture will increase the water concentration and the validity of the data will decrease. The two bands can be deconvoluted, but it is a difficult task and there is a great risk of inducing errors. For this reason the band at 1603-1609 cm$^{-1}$ will not be used quantitatively in this study.

In the OH stretching region two sharp bands are observed, one can be assigned to Ti-OH at 3730 cm$^{-1}$ and one to V-OH at 3642 cm$^{-1}$. Upon water adsorption these bands are increasing in intensity as expected and a very broad band in the 2600-3800 cm$^{-1}$ range are observed, due to adsorbed water on the surface of the catalyst. The $\nu_{V=O}$ vibration at 2043 cm$^{-1}$ is also influenced by the adsorbed water shifting down indicating that water adsorbs on the vanadium sites like proposed earlier in section 2.4 (Figure 2.5 on page 15) weakening the V=O band and increasing the amount of V-OH as observed. This observation fits with a DFT study done by Lewandowska et al. [169] showing that vanadium sites can be hydrated with one or more -OH groups under humid conditions forming new vanadia sites, see the three different sites $\mathbb{1}$, $\mathbb{1}$ and $\mathbb{3}$ in Figure 7.7 on page 88 . The small band at 1350 cm$^{-1}$ is organic residues adsorbed on the surface of the catalyst and are not catalytic active, see Section 4.7 on page 48 for further explanation.

After addition of $NH_3$ until steady state is achieved (ca. 30 min) several new bands are observed in the low region (1200-1900 cm$^{-1}$). Two new adsorptions are present at 1225 cm$^{-1}$ and
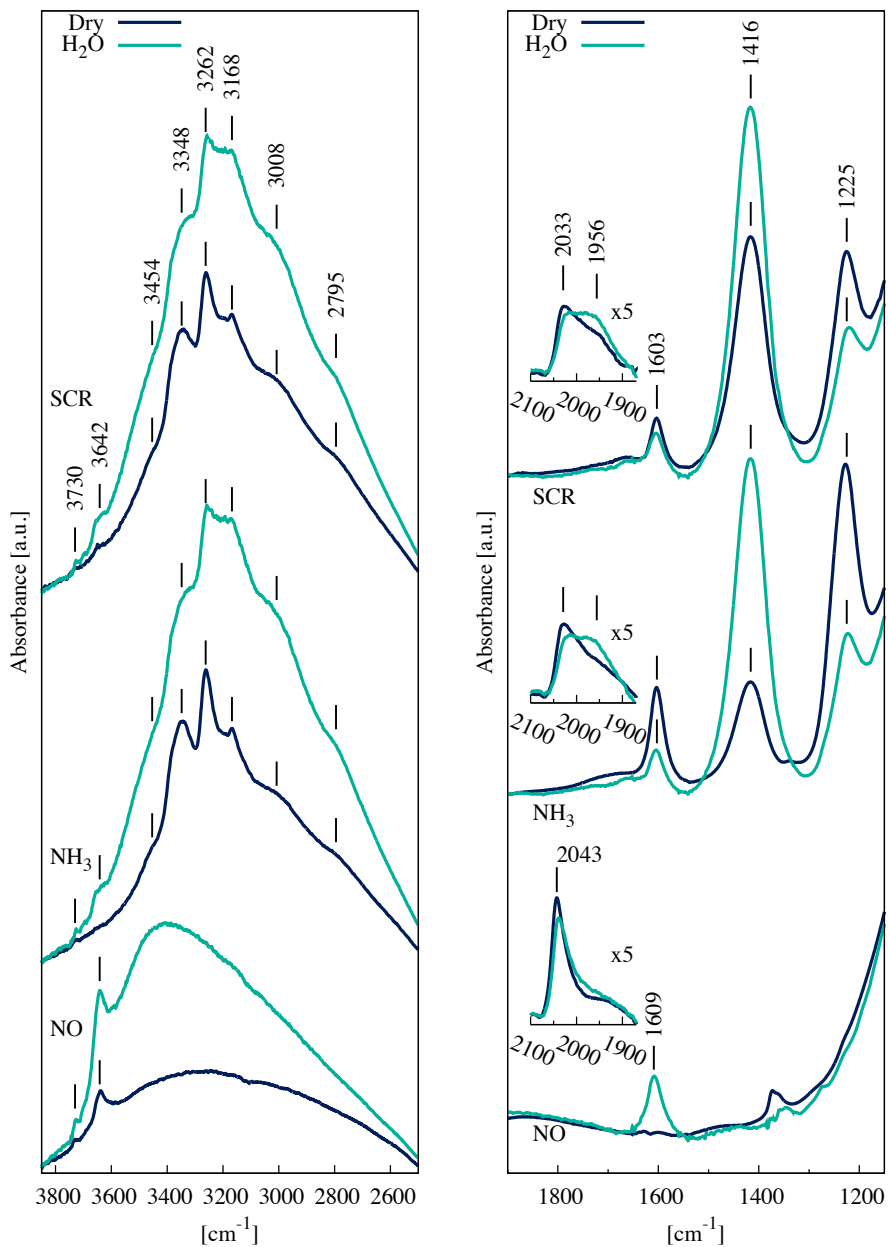
**Figure 7.3.:** *Spectra of a 20 wt.% $V_2O_5/TiO_2$ measured in dry and humid conditions (∼2% $H_2O$), from below **NO:** 940 ppm NO and 3.2 % $O_2$ in He, **NH3:** 940 ppm $NH_3$ and 3.2 % $O_2$ in He and **SCR:** 940 ppm NO, 940 ppm $NH_3$ and 3.4 % $O_2$ in He. Under all conditions the total flow was 128 $ml/min$*
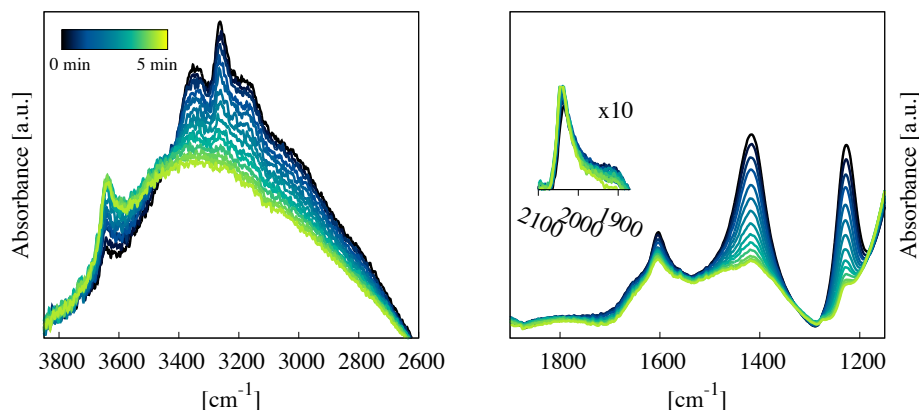
**Figure 7.4.:** *Transient in-situ FTIR study of Brønsted and Lewis adsorbed $NH_3$ reactivity, a 20 wt.% $V_2O_5/TiO_2$ catalyst with preadsorbed $NH_3$ under working conditions at 250 °C is exposed to a He, $O_2$ and NO gas mixture and a spectrum is measured every 20 second.*

1416 cm$^{-1}$, which can be assigned to adsorbed $NH_3$. The band at 1225 cm$^{-1}$ originates from the symmetric bending mode of $NH_3$ coordinated to Lewis sites (denoted $\delta_s NH_3$). The second band at 1416 cm$^{-1}$ arises from the asymmetric bending mode of adsorbed $NH_3$ on Brønsted sites (denoted $\delta_{as} NH_4^+$) [40,41,54]. Furthermore the band at 1603 cm$^{-1}$ can be assigned to the asymmetric bending mode of Lewis coordinated $NH_3$ (denoted $\delta_{as} NH_3$). Upon adsorption of $NH_3$, the $\nu_{V=O}$ vibration at 2043 cm$^{-1}$ is shifted down to 2033 and 1956 cm$^{-1}$, this can be explained by the adsorption of $NH_3$ at the V=O site either as Lewis or Brønsted coordinated $NH_3$. This observation is wellknown [41,42] and in Raman a similar trend have been observed [170,171]. Upon introduction of $H_2O$ the shift is even more pronounced, increasing the 1956 cm$^{-1}$ band and decreasing the 2033 cm$^{-1}$ band, indicating that Brønsted coordinated $NH_3$ is weakening the V=O bond more than Lewis coordinated $NH_3$.

Ammonia adsorption in humid conditions also yield a changed Brønsted Lewis ratio. The amount of Brønsted coordinated $NH_3$ is increased and Lewis coordinated decreased. It is a known phenomenon that the Lewis Brønsted acidity of a catalyst is not a fixed ratio and can be changed by adding or removing water [4,68,156]. This is the similar trend as observed by $H_2O$ adsorption, where an increase of V-OH was observed and correlated with a shift of the $\nu_{V=O}$ vibration, hence forming more Brønsted acid sites.

An increase of the $\delta_{as} NH_3$ asymmetric bending mode is also observed at 1603 cm$^{-1}$ and introduction of $H_2O$ increases this band further owing to adsorbed water. In the 3800-2600 cm$^{-1}$ region a decrease of $\nu_{V-OH}$ is observed due to hydrogen bonding of $NH_3$. In humid conditions small amounts of V-OH is still observed, however the Ti-OH band is only affected slightly. A multiplet is observed in the NH stretching region (2795, 3008, 3168, 3262, 3348 and 3454 cm$^{-1}$) due to symmetric and asymmetric $\nu NH$. The change in Lewis Brønsted ratio upon water

addition can be used to conclude that the bands at 3454, 3348 and 3262 cm$^{-1}$ is correlated with Lewis bonded ammonia and 2795, 3008 and 3168 cm$^{-1}$ with Brønsted bonded ammonia. However because of the complexity of the area there is no direct correlation.

Introduction of NO to the gas mixture changes the Brønsted / Lewis ratio in dry conditions. In humid conditions no considerable changes are observed due to the increased amount of $H_2O$ produced by the SCR reaction. The described nitrosamide species are not observed under any conditions. This can be explained by the common assumption, that it decomposes readily upon formation. However, the activated amide specie that reacts with NO forming nitrosamide is not observed under NH$_3$ flow, and this is a direct contradiction to the mechanism by Ramis et al.[40]. Ramis et al. stated that an activated amine complex is formed and gives rise to a band at 1535 cm$^{-1}$, but these studies were not done under realistic working conditions. Conducting in-situ experiments under vacuum and very dry conditions can lead to wrong conclusions, and the amine complex have not been reported by other authors since[16]. The ammonia activation part of the Ramis et al. mechanism can therefore not be confirmed by our measurements. This indicates that the activation mechanism of NH$_3$ may not be going through a -NH$_2$ specie, or that the specie is only present in very low concentrations. Even though the amide specie was not observed it cannot be concluded that the NH$_3$ is not activated through an amide specie.

Another very debated subject of the mechanism is the reactivity of the Brønsted and Lewis adsorbed NH$_3$.

In Figure 7.4 on the preceding page, an in-situ transient FTIR study is depicted where pre-adsorbed NH$_3$ is exposed to a He, O$_2$ and NO gas mixture. Both the Lewis and Brønsted coordinated NH$_3$ decreases, hence reacting with the NO forming $H_2O$ and N$_2$. At the same time the $\nu_{V-OH}$ vibration is increasing indicating that V-OH groups are formed during the SCR reaction. Under normal working conditions these V-OH groups would again adsorb NH$_3$ and the SCR reaction would continue, but in absence of NH$_3$ these groups are preserved. The total amount of V=O is not changed through the experiment[a], only a slight shift towards higher cm$^{-1}$ is observed showing that NH$_3$ is removed from these sites as more and more NH$_3$ reacts. Further experiments has to be done to determine the reactivity of the Lewis and Brønsted adsorbed ammonia. In Figure 7.5 on the following page, the integrated values of the $\delta_{as}NH_4^+$ band at 1416 cm$^{-1}$ and the $\delta_s NH_3$ at 1225 cm$^{-1}$ during adsorption of NH$_3$ and reaction of adsorbed NH$_3$ with NO in dry or humid conditions are depicted. From these experiments it looks like the total amount of adsorbed NH$_3$ is higher in humid conditions, however this is not the case. Under humid conditions the amount of NH$_3$ should be a little lower, due to the competition with $H_2O$. The observation can be explained by the considerable difference between the extension coefficient of the $\delta_{as}NH_4^+$ and the $\delta_s NH_3$ bands, which Van Tongelen[172] estimated to be 7.

The data, in Figure 7.5 on the next page can be used to estimate an activity constant as a

---

[a]determined by deconvolution of the bonds at ∼2000 cm$^{-1}$
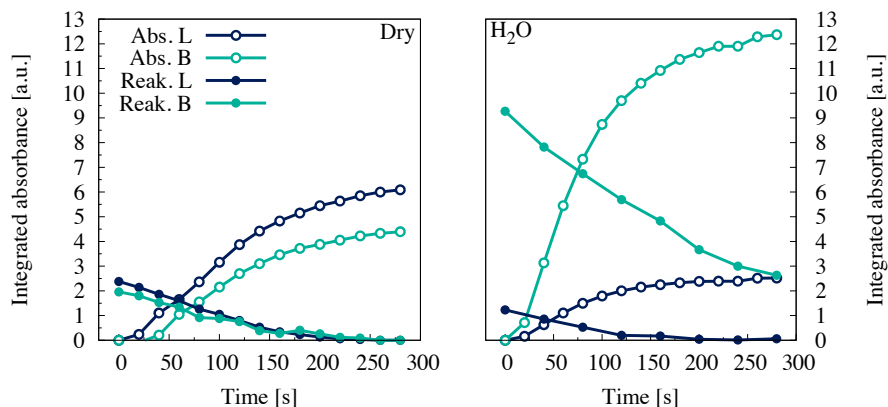
**Figure 7.5.:** *Integrated values of the $\delta_{as}NH_4^+$ band at 1416 cm$^{-1}$ and the $\delta_s NH_3$ at 1225 cm$^{-1}$ during adsorption of NH$_3$ and reaction of adsorbed NH$_3$ with NO in dry or humid conditions, time resolutions is one spectrum pr. 20 second. $\delta_s NH_3$ and $\delta_{as}NH_4^+$ are respectfully denoted as L and B followed by either Abs. or Reak.*

function of absorbance and time. The first linear region of the experiment can be correlated with the actual activity of the catalyst wafer in steady state, 14.2% conversion in humid conditions and 15.6% in dry. Combining these data yields an extension coefficient of 6.2 ($\delta_s NH_3$/ $\delta_{as}NH_4^+$=6.2). The estimated Lewis Brønsted ratio is then approximately 1:1 under humid conditions and 9:1 in dry. Furthermore the data showed that the total amount of adsorbed NH$_3$ is 10% lower in humid conditions. In both humid and dry conditions, the fastest decreasing type of adsorbed NH$_3$ is Lewis coordinated, having the same rate regardless of the conditions. The Brønsted adsorbed NH$_3$ is decreasing 6 times faster under humid conditions. The overall reaction rate is lower in humid conditions and can be explained by decreased availability of NH$_3$ combined with a slower reaction rate of Brønsted adsorbed NH$_3$ or that the Brønsted coordinated NH$_3$ has to migrate to an active Lewis centre to react, leading to a slower reaction rate. Because NH$_3$ can, as shown earlier, migrate from one type site to another it is possible that only Lewis or Brønsted adsorbed NH$_3$ is active. But because the activity in humid conditions is different than in dry it is likely that both sites are active. The combined rate of adsorption is nearly identical under both conditions only the ratio differs. Additionally the adsorption rates are much faster than the SCR reaction. Thus the rate-determining step must then be either the combined activation and decomposition of nitrosamide or the reoxidation of the vanadium redox site.

Adsorption of NH$_3$ in a O$_2$ deficient atmosphere increases the Lewis to Brønsted ratio. This is also observed in humid conditions, see steady state spectra in appendix Figure B.2 on page 110. When NO is introduced, this trend is further amplified, see Figure B.3 on page 110. This can be explained by the change of adsorbed H$_2$O on the surface. In O$_2$ deficient con-
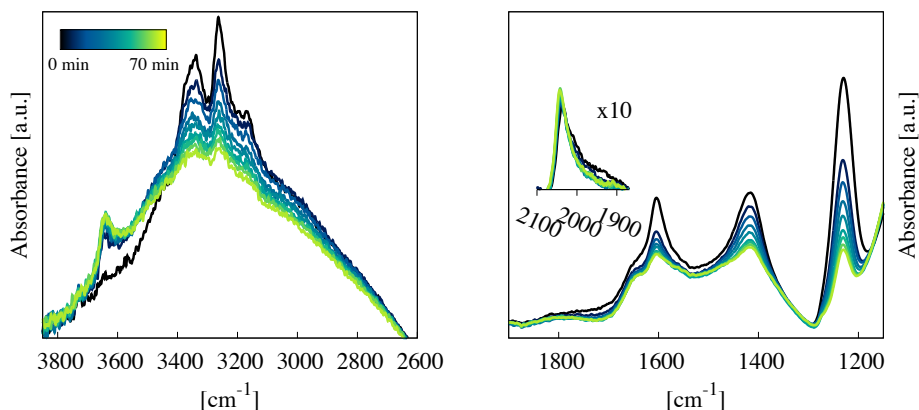
**Figure 7.6.:** *Transient in-situ FTIR study of Brønsted and Lewis adsorbed $NH_3$ reactivity, a 20 wt.% $V_2O_5/TiO_2$ with pre-adsorbed $NH_3$ under working conditions at 250 °C and in absence of $O_2$ is exposed to a He and NO gas mixture and a spectrum is measured every 10 min.*

ditions the SCR reaction is almost stopped and the amount of $H_2O$ formed on the surface is lower, compared to normal SCR reaction conditions, hence a lower amount of active sites are transformed into Brønsted sites. Furthermore under $O_2$ deficient conditions the reoxidation is not possible. These measurements under $O_2$ deficient conditions can illustrate if the V=O groups are reduced to V-OH during the SCR reaction as predicted by Inomata et al.[20] and Topsøe et al.[37,41,54]. But as seen in Figure 7.6 the total amount of V=O is constant throughout the experiment showing that the V=O bond is not broken during the SCR reaction contradicting the Inomata et al.[20] and Topsøe et al.[37,41,54] mechanisms. It is also generally accepted in newer literature that the V=O is a too strong bond to be broken in the SCR reaction, matching these observations[64,72].

In Figure 7.6 another transient experiment is depicted where a 20 wt.% $V_2O_5/TiO_2$ catalyst pre-adsorbed with $NH_3$ is exposed to NO in He and in absence of $O_2$. As expected the reaction rate is much slower and the rate is gradually reduced and after 70 min the SCR reaction is almost at a stop, because the redox sites are not regenerated by oxidation.

This illustrates that there are many more $NH_3$ adsorption sites than active reaction sites on the surface of the catalyst. In this experiment the $NH_3$ is adsorbed, then the flow of $NH_3$ is closed. Followed by a flushing with helium, ensuring that no $NH_3$ is present at very weak acid sites. Then the NO is added to the He gas. Again no change in the V=O is observed, but a formation of V-OH groups are occurring and not gradually with decreasing $NH_3$ as it is seen in a normal reaction of $NH_3$ on the surface, see Figure 7.4 on page 84. This can be interpreted as the reoxidation of the vanadia site containing the V-OH is inhibited and the adsorbed $NH_3$ is not migrating to the reduced active centre leaving the V-OH group on the surface.
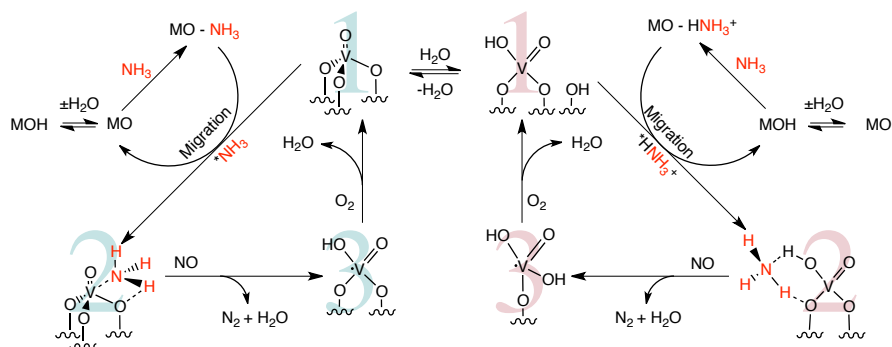
**Figure 7.7.:** *Proposed mechanism based on the observations done by in-situ FTIR described. The mechanism consists of two cycles one related to the Lewis centers and one to the Brønsted centres with equilibrium between the two cycles depending on water concentration. Both cycles are basically an adsorption of NH$_3$ on a surface site, migration of the adsorbent to an active site, reaction with NO and finally reoxidation of the active site. The reaction 2-3 is very fast and therefore the nitrosamide intermediate not observed in the in-situ FTIR measurements.*

Using all the above information a refined mechanism can be formulated and graphical illustrated, see Figure 7.7. The mechanism comprises two different catalytic cycles, one Lewis based and one Brønsted cycle. Between the cycles there is an equilibrium that depends on water concentration. In dry conditions the Lewis cycle predominate and upon water addition the amount of NO converted by the Brønsted cycle is increased. This is the key feature of the mechanism explaining that both Brønsted and Lewis acid sites are active and there is a dynamic equilibrium between the two. Another important part of the mechanism is the adsorption of NH$_3$. The adsorption occur at many different sites on the surface not only at vanadium sites also titania or sulphate sites if the catalyst is sulphated. This is correlated with the observation that it is not possible to distinguish between two Lewis coordinated NH$_3$ bonded to two different sites. The adsorbed NH$_3$ then migrates to an active site and reacts fast with gas phase NO forming a nitrosamide specie that decomposes rapidly to N$_2$ and H$_2$O. The active site is then reduced, a V-O-Ti bond is broken and a -OH group is formed during the decomposition. After the reduction, the active site is reoxidised by O$_2$. This was the step that was inhibited under the O$_2$ deficient transient in-situ FTIR experiment, leading to an increase of V-OH and a very slow NH$_3$ decrease. This Showed that NH$_3$ is not migrating to reduced active centres and that the reduction of an active centre yields a formation of V-OH. As for the transient study a graduate increase of V-OH was observed under normal conditions as the NH$_3$ concentration decreased showing that the NH$_3$ migrate to the active centres. The increase of V-OH is owing to the Brønsted Lewis equilibrium after reaction of NH$_3$. After the reoxidation the catalytic cycles are closed. Throughout the mechanism the V=O bond is preserved as showed in all the experiments. This also complies to new theoretical studies stating that the bridge V-O-Ti is the most reactive part of the active vanadia centres [52,64,72]. The rate determining
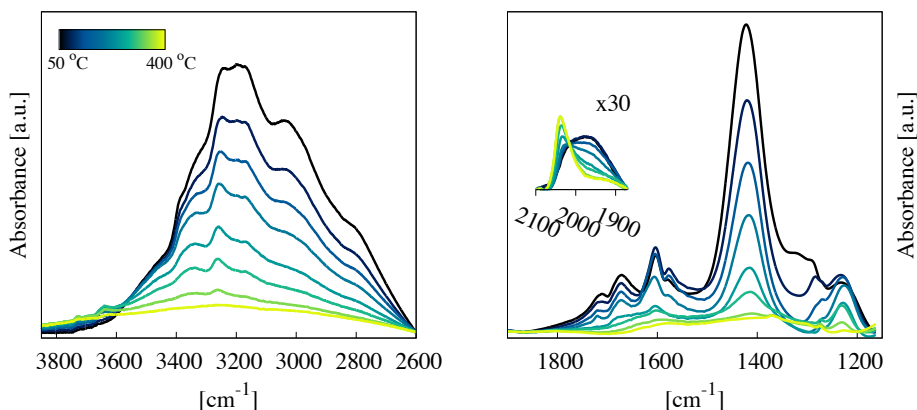
**Figure 7.8.:** *Temperature controlled in-situ FTIR desorption study of a 20 wt.% $V_2O_5$/$TiO_2$ , heating from 50 to 400 °C in steps of 50 °C.*

step of the mechanism is the reaction of gas phase NO with adsorbed $NH_3$. Not the formation of nitrosamide or decomposition because, this has to be very fast since we did not observe nitrosamide or any related compounds. In addition this also fits very well with the fact that the SCR reaction is first order regarding NO if $NH_3$ is in excess. As illustrated later by Raman studies the vanadia species on the surface are of a polymeric character, hence the mechanism should also apply for polymeric vanadate species (schematically by substituting V-O-Ti with V-O-V).

### 7.2.1. Temperature controlled in-situ FTIR desorption of $NH_3$

As a supplement to ordinary $NH_3$-TPD measurements a temperature controlled in-situ FTIR desorption study have been performed. Here $NH_3$ has been adsorbed at 25 °C followed by heating and a spectrum is collected every 50 °C up to 400 °C. The measurements show (see Figure 7.8) that the amount of Lewis coordinated ammonia is much lower at 50 °C than the amount of Brønsted adsorbed $NH_3$ even when the extension coefficient of 6.2 is taken into consideration. Upon heating, the Lewis adsorbed $NH_3$ is not changing from 50-200 °C, whereas the Brønsted adsorbed $NH_3$ is decreasing fast until the observed ratio in Figure 7.3 on page 83. From 200 to 400 °C both Lewis and Brønsted coordinated $NH_3$ desorb. This shows that most of the desorbed ammonia observed during the first 100-200 °C of the $NH_3$-TPD measurements are desorbed from Brønsted acid sites and not necessary the active sites under working conditions. Moreover it supports that the Lewis adsorbed $NH_3$ is much more stable than Brønsted coordinated $NH_3$ in dry conditions. Furthermore it indicates that the important desorption band at 400 °C observed in Figure 6.16 on page 73, can be associated with a desorption of both Lewis and Brønsted coordinated $NH_3$. Again showing that both sites are important in the
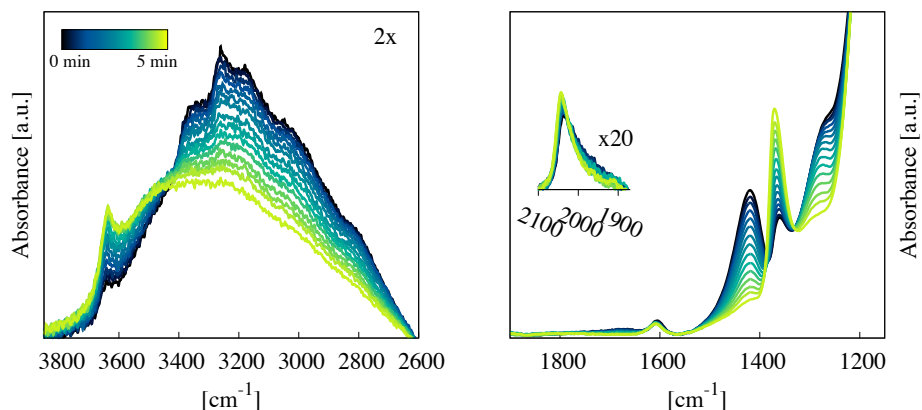
**Figure 7.9.:** *Transient in-situ FTIR study of Brønsted and Lewis adsorbed $NH_3$ reactivity, a sulphated 20 wt.% $V_2O_5/TiO_2$ with pre-adsorbed $NH_3$ under working conditions at 250 °C exposed to a NO, $O_2$ and He gas mixture and a spectrum is measured every 20 sec.*

SCR reaction mechanism, due to the observed correlation between the 400 °C desorption band and activity of the catalyst during potassium deactivation. The temperature profiles of the two experiments cannot be compared directly because the FTIR investigations are done over 6 hours, waiting at each temperature for steady state and the $NH_3$-TPD profile is measured at a heating rate of 10 $^{\circ}C/_{min}$. Additionally it proves the importance of complimentary in-situ FTIR investigations and that $NH_3$-TPD profiles are difficult to analyse without additional information.

## 7.3. FTIR on a sulphate promoted 20 wt.% $V_2O_5/TiO_2$ catalyst

In Figure 7.11 on page 92 a serie of in-situ FTIR measurements is depicted of a sulphated 20 wt.% $V_2O_5/TiO_2$ catalyst under different conditions. The spectrum measured in dry NO, $O_2$ and He gas mixture show one more characteristic band compared to the unsulphated catalyst, see Figure 7.3 on page 83, which as earlier described arises from $\nu_{S=O}$ as a sharp band at 1374 cm$^{-1}$. Many authors have demonstrated that the band can be assigned to a S=O group on a tridentate or bidentate sulphate specie coordinated to the $TiO_2$ surface [165,166], see Figure 7.10 on the facing page. Sulphate on other surfaces such as $ZrO_2$ shows similar trends and can therefore be compared with studies conducted on sulphated $TiO_2$ [45,173–176].

Introduction of water shifts the $\nu_{S=O}$ band to 1361 cm$^{-1}$ and a new band appears at 1283 cm$^{-1}$ corresponding the vibration of a S=O group bonded to a water molecule. This is rather comparable to the vanadia hydration or as the illustrated reaction in Figure 7.10 on the next page,
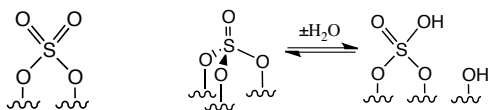
**Figure 7.10.:** *Proposed sulphate species on the surface of sulphated metal oxide catalysts. Proposed by Arata et al. [45] and Saur et al. [165], respectively.*

however the S-OH vibration is not observed. The bands corresponding to $\nu_{Ti-O-S}$ vibrations at 1129 and 1081 cm$^{-1}$ (not included in Figure 7.11) are not changing. This suggests that the bonds are not broken and it is only the S=O group that is affected by the adsorbed H$_2$O. This Demonstrates that the Saur et al. hydration is not observed, see Figure 7.10.

Like the unsulphated catalyst a new bond is observed, after addition of water, at 1609 cm$^{-1}$ corresponding to V$-$OH$_2$ vibrations of adsorbed water. In this case the amount of water is 2.5 times greater[b] due to the increased acidity of the catalyst. Furthermore in the OH stretching region one sharp band is observed corresponding to the vibration of V-OH at 3642 cm$^{-1}$ identical to the unsulphated catalyst. The Ti-OH vibration at 3730 cm$^{-1}$ is not observed, which can be explained by adsorption of sulphate species on these sites.

The $\nu_{V=O}$ vibration is observed at 2043 cm$^{-1}$ showing that the sulphate species are not bonding to the vanadium species lowering the frequency of this band. Upon water adsorption the vibration shifts a little to lower frequencies. Compared to the unsulphated catalyst this shift is a little greater matching the increased amount of water adsorbed on the surface.

The $\nu_{S=O}$ vibration is more affected by adsorption of NH$_3$ than by adsorption of water. A decrease and shift of the $\nu_{S=O}$ vibration to 1348 cm$^{-1}$ is observed. After adsorption the only visible band remaining from sulphate species is the shifted band at 1348 cm$^{-1}$. This suggest that all the tridentate or bidentate sulphate on the surface are bonding to NH$_3$ lowering the vibration frequency even further upon adsorption of NH$_3$.

Like the unsulphated catalyst the NH$_3$ adsorbs as two different species Lewis coordinated and Brønsted adsorbed at 1225 cm$^{-1}$ $\delta_s$NH$_3$ and 1416 cm$^{-1}$ $\delta_{as}$NH$_4^+$, respectively. The increased acidity of the catalyst compared with the unsulphated has increased the overall amount of adsorbed NH$_3$, but also changed the Brønsted Lewis ratio increasing the Brønsted coordinated NH$_3$ more than the counter part.

The adsorbed NH$_3$ is again influencing the $\nu_{V=O}$ vibration lowering it from 2044 cm$^{-1}$ to 2033 cm$^{-1}$ and 1956 cm$^{-1}$ identical to the unsulphated catalyst. This shows that the vanadia sites are affected identically suggesting that the vanadia sites are the same.

Introduction of water to the gas mixture increases the Brønsted adsorbed NH$_3$ and the band at 1348 cm$^{-1}$ disappears entirely suggesting that it is the Brønsted adsorbed ammonia that interact with the sulphate species on the surface.

The change in the S=O vibration at 1374 cm$^{-1}$ and the decrease of the two bending modes at

---

[b]Calculated by normalising the spectra using the $\nu_{V=O}$ vibration and then measuring the amount of adsorbed H$_2$O

**Figure 7.11.:** *Spectra of a 20 wt.% $V_2O_5/TiO_2$ sulphated catalyst measured in dry and humid conditions ( 2% $H_2O$), from below **NO:** 940 ppm NO and 3.2 % $O_2$ in He, **NH3:** 940 ppm $NH_3$ and 3.2 % $O_2$ in He and **SCR:** 940 ppm NO, 940 ppm $NH_3$ and 3.4 % $O_2$ in He*
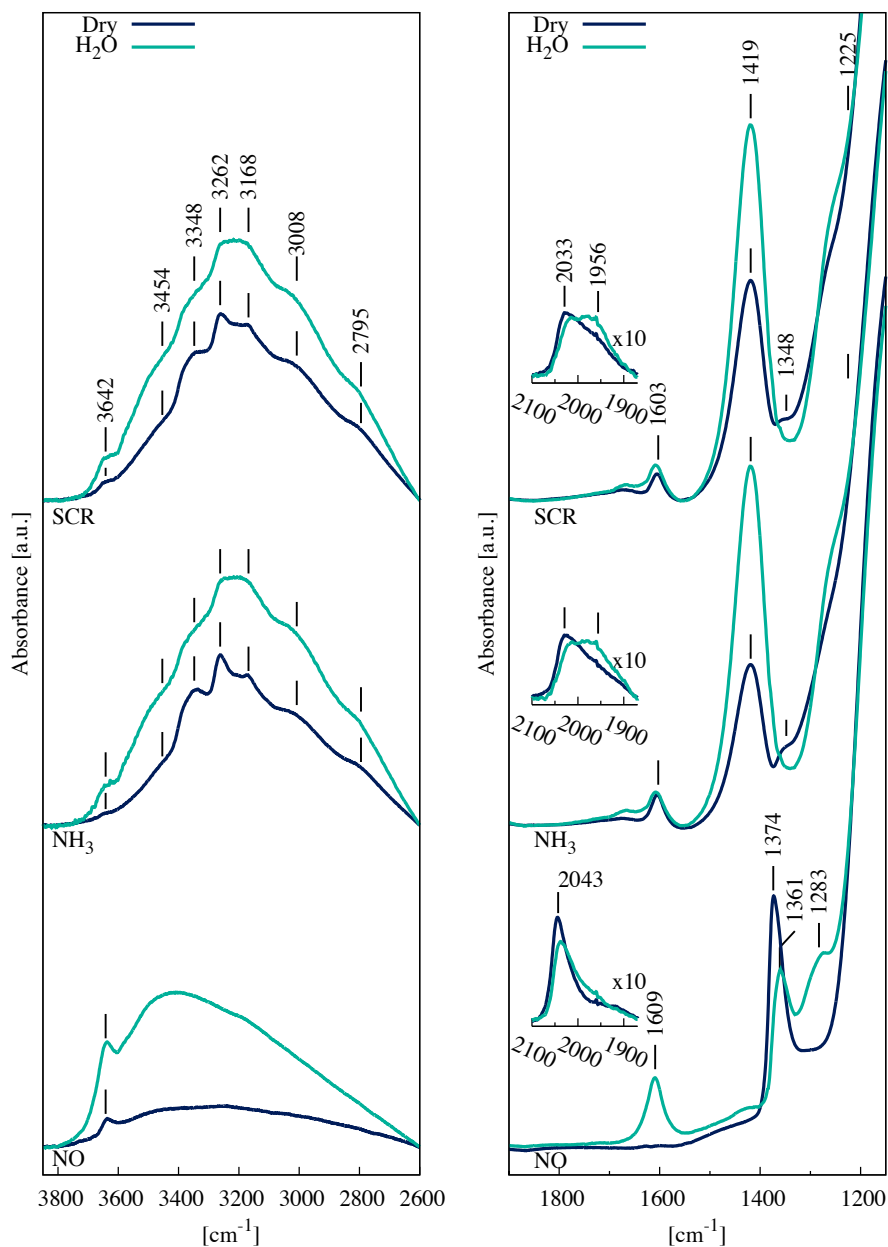
1225 and 1416 cm$^{-1}$ corresponding to Lewis and Brønsted coordinated NH$_3$ and $\delta_s$NH$_3$. These vibrations are easily followed in Figure 7.9 on page 90, where a transient in-situ FTIR study of the SCR reaction is presented. As the previously described transient experiments, the catalyst has been exposed to NH$_3$. After adsorption the catalyst was treated with He at 250 °C until steady state, prior to the exposure to the NO, O$_2$ and He gas mixture. Upon NO gas exposure the adsorbed NH$_3$ reacts and the two NH$_3$ adsorption bands decrease accordingly and the $\nu_{S=O}$ band increases. This shows that the adsorbed NH$_3$ at the sulphate sites are migrating to the active sites and reacts, which fits with activity measurements showing that no activity increase is observed due to sulphation, see Figure 4.5(a) on page 39.

From these observations it is clear that the sulphated and the unsulphated catalyst are identical in terms of reaction mechanism just with one small difference of Lewis Brønsted ratio. The increased acidity has increased the amount of Brønsted adsorbed ammonia more than of Lewis coordinated. The overall amount of NH$_3$ adsorbed has increased. However as it was shown earlier the amount of acid sites on an unsulphated catalyst is already much higher compared with the number of active centres, hence the activity will not increase by increasing the acidity and this is not observed. But the potassium resistance will increase due to the "capturing" capability of sulphate species on the surface. In the next section this subject will be discussed.

## 7.4. Deactivation mechanism

A selection of the potassium deactivated catalysts from Section 6.4.1 on page 71 have been investigated using in-situ FTIR to determine the deactivation mechanism or at least see how the potassium affects the catalyst. In Figure 7.12 on page 95 in-situ FTIR spectra of a 20 wt.% V$_2$O$_5$/TiO$_2$ catalyst deactivated with different amounts of potassium ranging from 0 to 675 $^{\mu mole}/_g$ is depicted. The left side of the Figure is the OH range of the spectrum and the right side is the low range with a zoom of the V=O band. The $\nu_{V=O}$ vibration is measured in NO, O$_2$ and He to ensure the dehydrated form. At 0 $^{\mu mole}/_g$ the catalyst reassembles the described sulphated catalyst with a sharp absorption at 2043 cm$^{-1}$, this band is as earlier described the $\nu_{V=O}$ vibration. Deconvolution of this band show that it comprises three different bands all originating from different vanadia species. The two vibrations at 2046 and 2030 cm$^{-1}$ probably arise from the two vanadia species denoted as $\mathbb{1}$, $\mathbb{1}$ in Figure 7.7 on page 88. Lewandowska et al. [169] showed that the two species would have absorptions reassembling these, the tridentate specie at 1020 (and the overtone correspondingly) and the bidentate specie at 20 cm$^{-1}$ lower. The band at 1978 cm$^{-1}$ could arise from a hydrated monodentate vanadia specie.

Right side of Figure 7.12 on page 95 show the -OH region in humid NO, O$_2$ and He gas mixture to ensure a hydrated surface. If the measurements were done under dry conditions the V-OH

would not be a reliable measure for the amount of V-OH on the surface, due to the fact that the amount of V-OH is very dependent on water concentration. The first spectrum shows a working SCR catalyst with a high degree of V-OH groups on the surface. As earlier mentioned the Ti-OH groups are not observed due to the sulphation.

After deactivation using 75 $\mu mole/g$ the $\nu_{V=O}$ vibration is shifted by a moderate amount. The vibration at 2046 cm$^{-1}$ has decreased in intensity and the band at 2030 cm$^{-1}$ is shifted downwards and the last band has increased in intensity. The amount of V-OH has also decreased and the band has split into two. Furthermore the amount of water adsorbed on the surface are decreased. These observations suggest that the potassium has reacted with the vanadia species almost as $NH_3$ does, binding to V-OH and close to V=O. Exposure to $NH_3$ shifts the V=O absorptions further showing that some $NH_3$ can still be adsorbed, the activity is also still high at 1570 cm$^3$/s·g , see Figure 6.12 on page 71.

At 280 $\mu mole/g$ the $\nu_{V=O}$ vibration has shifted even further leaving only a small fraction of tridentate vanadia and the activity has decreased a large amount. Adsorption of $NH_3$ also show that the amount of $NH_3$ adsorbed at the vanadia sites has decreased to a very little fraction. The amount of V-OH on the surface in humid conditions has decreased further and is now only a third of the original concentration.

Increasing the potassium loading to further to 450 $\mu mole/g$ the $\nu_{V=O}$ vibration consists of two different bands one major at 1980 and one small at 2030 cm$^{-1}$. This suggests that almost all the vanadia comprises potassium coordinated monomeric and dimeric species with the first over represented. The V-OH has also decreased and proves that there is only little vandia that can be hydrated and again the amount of water adsorbed has decreased further.

Deactivation by 675 $\mu mole/g$ decreases the V-OH further and now the $\nu_{V=O}$ vibration mainly consists of one vibration. Adding $NH_3$ to the gas mixture has almost no effect on the $\nu_{V=O}$ vibration, matching the poor activity at this state.

The sulphate species on the surface of the catalyst also undergo many different structural changes during the potassium deactivation of the catalyst, see Figure 7.13 on page 96. The first spectrum show the earlier described fresh catalyst with the S=O vibration highlighted at 1373 cm$^{-1}$ and the two S-O-Ti vibrations at 1130 and 1083 cm$^{-1}$. Suggesting that there are either bidentate or tridentate sulphate species on the surface matching observations of Hofmann et al. on a similar $ZrO_2$ system and the observations of Saur et al. on a sulphated $TiO_2$ system [165].

After addition of 75 $\mu mole/g$ the S=O band has shifted to 1301 cm$^{-1}$ and the two bands at 1130 and 1083 cm$^{-1}$ have decreased in intensity. This suggests that some of the S-O-Ti bonds have been broken and the sulphate specie is changed from a tridentate species to a bidentate. The shift of the S=O imply that the potassium have bonded close to or to this group weakening the bond. Adsorption of $NH_3$ shows that the sulphate groups still interact with the adsorbed

**Figure 7.12.:** *Spectra of a 20 wt.% $V_2O_5$/$TiO_2$ sulphated catalyst deactivated with different amounts of potassium ranging from 0 to 675 $^{\mu mole}/_g$. The left side spectra is measured under a humid NO, $O_2$ and He gas mixture to hydrolyse all available V-O groups to V-OH. Right side is the V=O region measured in dry NO, $O_2$ and He gas mixture. The coloured line is the measured data and the thin black line is the gauss functions fitted to the date, the grey line is data collected using a $NH_3$, $O_2$ and He gas mixture. All spectra are steady state.*

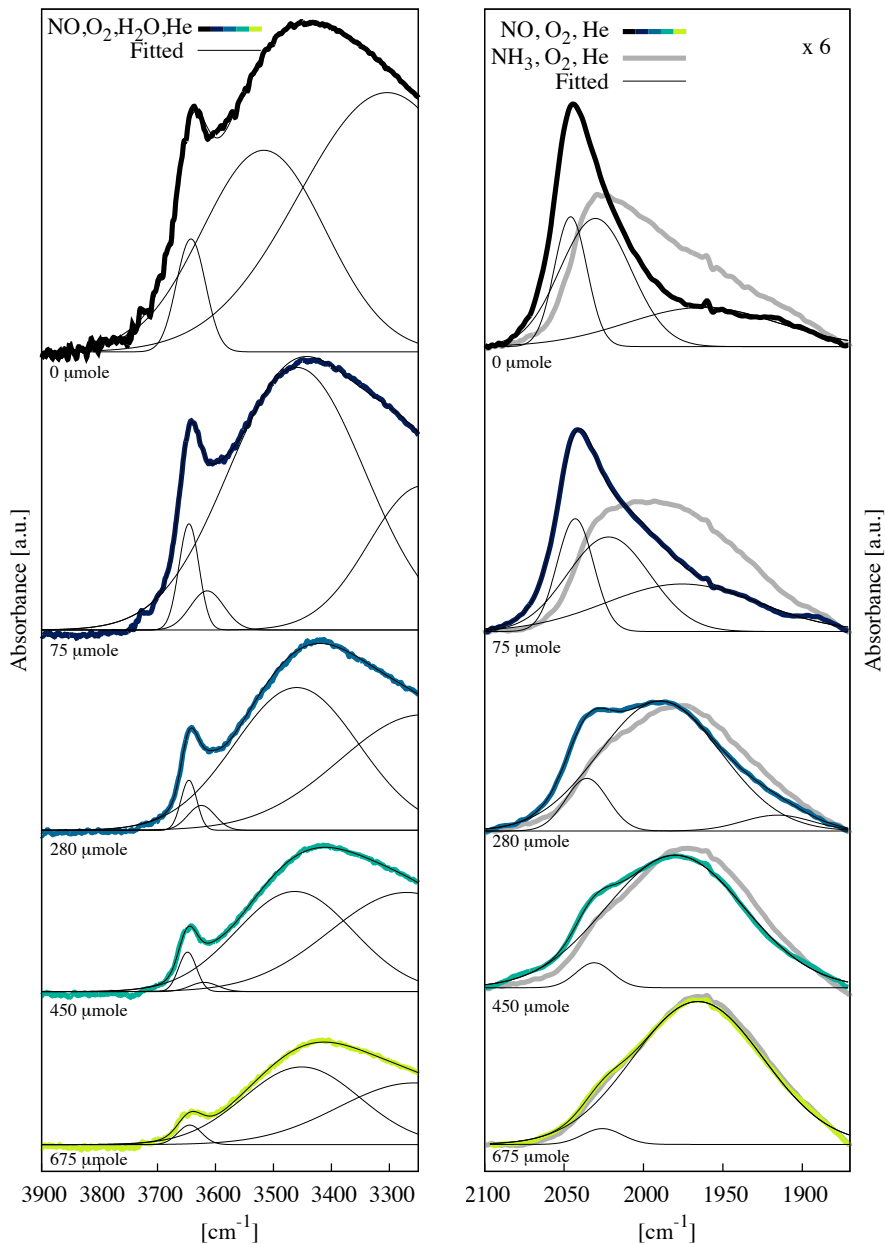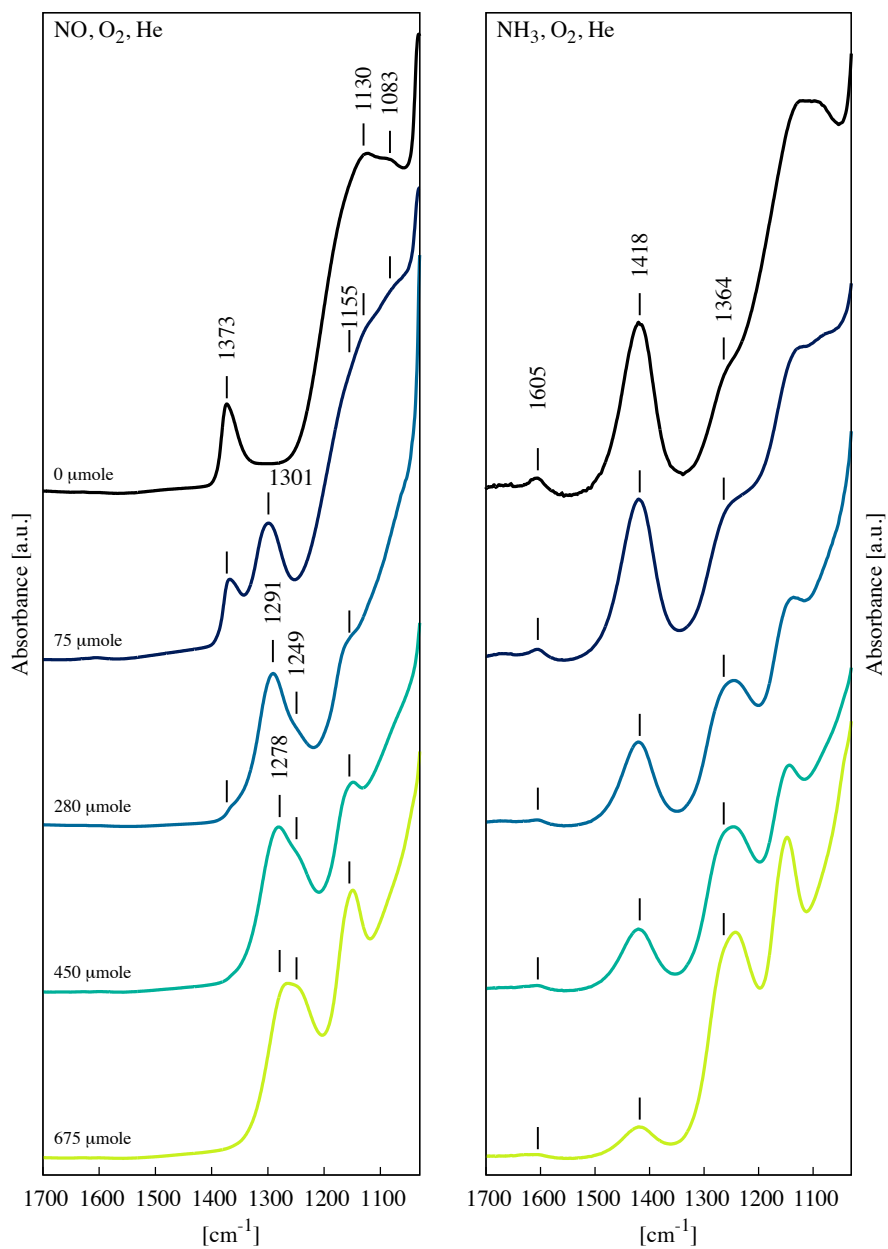**Figure 7.13.:** *Spectra of a 20 wt.% $V_2O_5/TiO_2$ sulphated catalyst deactivated with different amounts of potassium ranging from 0 to 675 $^{\mu\,mole}/_g$. The left side spectra is measured under a dry NO, $O_2$ and He gas mixture. Right side measured under a $NH_3$ containing gas mixture to show the amount of adsorbed $NH_3$ as a function of potassium loading.*

ammonia and that the amount of ammonia adsorbed are almost identical to the fresh catalyst. Deactivation by 280 $^{\mu mole}/_g$ changes the sulphate species more, the S=O vibration at 1373 cm$^{-1}$ is almost removed and the band at 1301 cm$^{-1}$ shifts to 1291 cm$^{-1}$. This demonstrates that almost all the sulphate on the surface are affected by the potassium, at a S:K ratio of 2:1. The Two S-O-Ti vibrations decrease further and a new band at 1155 cm$^{-1}$ increases a little. This indicates that the tridentate species are removed and new bidentate or monodentate species are formed. The amount of NH$_3$ adsorbed is decreased to half implying that much of the sulphate on the surface is affected by the potassium. After deactivation by 675 $^{\mu mole}/_g$ the sulphate species are probably changed to a mixture of monomeric and dimeric species. The activity is very low but some NH$_3$ can still be adsorbed on the surface due to a little acidity left.

The in-situ FTIR measurements illustrated that the sulphate reacts with potassium increasing the potassium resistance and at the same time increasing the acidity. At some point all the active sites are poisoned and the adsorbed NH$_3$ cannot be used. This can be explained by the amount of acid sites exceeds the number of active sites many times.

Furthermore it was showed that potassium coordinates to the active vanadia centres as NH$_3$ does.

## 7.5. In-situ Raman spectroscopy of 20 wt.% $V_2O_5/TiO_2$

### 7.5.1. Experimental setup

A home made Raman cell was used for recording the in situ Raman spectra of the studied catalysts consisting of a double-walled quartz-glass transparent tube furnace mounted on a xyz plate allowing it to be positioned on the optical table. The inner furnace tube (23 mm o.d.; 20 mm i.d and 10 cm long) is kanthal wire-wound for heating the cell. The cell has a gas inlet and a gas outlet and a thermocouple sheath possessing a sample holder at its tip. Approximately 100 mg of each catalyst was pressed into a wafer and mounted on the holder that could be vertically adjusted in the in situ cell. The gases used were O$_2$ (L'Air Liquide 99.995%) at a 15 $^{cm^3}/_{min}$ flow, 10000 ppm $^{NH_3}/_{N_2}$ (L'Air Liquide) and N$_2$ (L'Air Liquide 99.999%) of which the flows were controlled by electronic mass flow meters.

A 491.5 nm DPSS (diode pumped solid state) laser (Cobolt/Sweden) was used for recording of the Raman spectra. The laser beam, operated at a power level of 80 mW, was focused on the sample by a cylindrical lens. The incident light was slightly defocused in order to reduce sample irradiance. The scattered light was collected at 90°, analysed with a 0.85 m Spex 1403 double monochromator and detected by a –20 °C cooled RCA PMT equipped with EG&G photon counting electronics interfaced with Labspec software. Due to the extremely low scattered
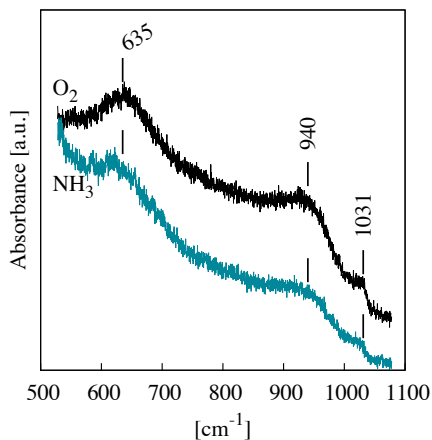
**Figure 7.14.:** *In-situ Raman spectra of a 20 wt.% $V_2O_5$/$TiO_2$ catalyst synthesised with $H_2SO_4$, $NH_4Cl$ and Ethanol. Measured under flowing $O_2$ and $NH_3$/$N_2$ at 250 °C.*
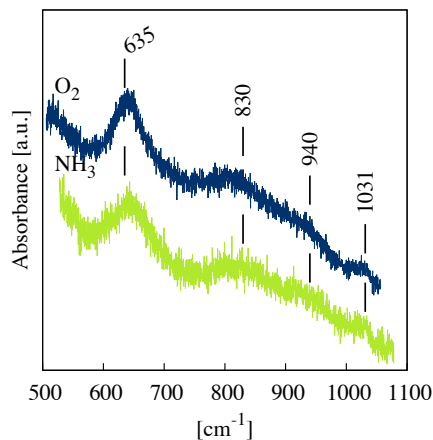
**Figure 7.15.:** *In-situ Raman spectra of a 20 wt.% $V_2O_5$/$TiO_2$ catalyst synthesised with $HNO_3$, $NH_4Cl$ and THF. Measured under flowing $O_2$ and $NH_3$/$N_2$ at 250 °C.*

signal arising from the samples, very slow scans (up to 7 hours per scan) were necessary in order to improve the signal-to-noise ratio. Recording of spectra took place initially at ambient conditions and subsequently at 250 °C under flowing $O_2$ (in situ dehydrated conditions) after exposing the studied sample for 30 min at 420 °C under flowing $O_2$. Each sample was then subjected to a 2200 ppm $^{NH_3}/_{N_2}$ flow for 30 min and the corresponding in situ Raman spectrum was recorded.

### 7.5.2. Results

Figure 7.14 and 7.15 shows in-situ Raman spectra obtained under $O_2$ flow at 250 °C (Top), of two catalysts. One 20 wt.% $V_2O_5$/$TiO_2$ catalyst synthesised with THF, $NH_4Cl$ and $HNO_3$ (denoted $^{THF}_{HNO_3}$) and another catalyst synthesised using ethanol, $NH_4Cl$ and $H_2SO_4$ (denoted $^{Ethanol}_{H_2SO_4}$), see Section 4.3 on page 36 for further information. The strong feature seen at 635 cm$^{-1}$ in all four spectra originate from the vibration mode of $TiO_2$. The rest of the bands arises from dispersed amorphous vanadates or deposited vanadia overlayers.

The $^{Ethanol}_{H_2SO_4}$ catalyst exhibits the typical characteristics of a $V_2O_5$/$TiO_2$ catalyst with a high coverage of dispersed vanadia [170,177–180]. The V=O stretch is observed at 1031 cm$^{-1}$ like in the previous FTIR measurements. The ~940 cm$^{-1}$ broad feature is due to antisymmetric V-O-V stretches, which judged from their location originate from small vanadate sites [177].

The $^{THF}_{HNO_3}$ catalyst exhibit the V=O stretching band as well as the broad V-O-V feature. A new

broad band is observed at $\sim$830 cm$^{-1}$, which could indicate an occurrence of amorphous poly-vanadate overlayers, suggesting a poorer dispersion of the vanadia. The very low surface area $^{MeOH}_{H_2SO_4}$ catalyst showed same bands supporting this hypothesis, see Appendix Figure B.6 on page 112.

An alternative interpretation is that the feature at $\sim$830 cm$^{-1}$ arises from the V-O-V stretching and the band at $\sim$940 cm$^{-1}$ is stretching of Ti-O-V interface bonds. As it was suggested by Brázdová et al. [181] on a AlVO$_4$ system. This interpretation also fits with the observations stated above - an increase of V-O-V and a decrease of V-O-Ti with decreasing surface area.

Great intensity loss for the V=O stretching band and correspondingly significant lowering of the band at 940 cm$^{-1}$ is observed upon NH$_3$ treatment, see Figure 7.14 and 7.15. The band that has been arranged to the vanadate overlayers or V-O-V of the $^{THF}_{HNO_3}$ catalyst is affected to a much lesser extent.

From this it is concluded that the active centres are not identical on the two catalysts, suggesting that the solvent is not only responsible for the surface area but also the nature of the active centres. This also illustrates the difference in activity of polymeric and dimeric vanadia species. The $^{MeOH}_{H_2SO_4}$ catalyst has a very low surface area but retains a high activity due to polymeric vanadia species.

## 7.6. Concise conclusion

Using in-situ FTIR have proven to be a very effective method to investigate the SCR reaction in-situ on the surface of the catalyst. Through these measurements a mechanism for the SCR reaction on the nano-catalyst has been proposed, explaining the importance of both Brønsted and Lewis acid sites on the surface. It also showed that the adsorption sites are not necessarily the same as the active sites, so migration of adsorbed NH$_3$ is an important step in the mechanism. Furthermore the measurements also showed that the ratio of Brønsted and Lewis acid sites are dynamic. Lewis sites can be converted into Brønsted sites upon water addition and vise versa.

Potassium deactivation was also investigated by this method showing that both vanadia and sulphate on the surface of the catalyst was affected upon deactivation. The way potassium deactivated the catalyst reassembled the adsorption of NH$_3$ suggesting that potassium adsorb on the same sites as NH$_3$. Both the amount of the tridentate vanadia and free V-OH groups was related to the activity of the catalyst and potassium deactivation decreased the amount of both sites. This matched the proposed mechanism arguing that the active species was a tridentate and a bidentate vanadia specie where ammonia could coordinate to the vanadia atom or to the bridging V-O-Ti oxygen.

The improved potassium resistance of the sulphated catalysts was also explained by the coor-

dination of potassium to the sulphate species on the surface of the catalyst shielding the active vanadia. This was observed by a change of the sulphate species from a tridentate form to a bidentate and lastly a monodentate form. The sulphation also increased the acidity adsorbing more $NH_3$ even at high potassium loadings. The limiting activity factor was not the amount of adsorbed $NH_3$ but the amount of active vanadia centres.

# 8

## Concluding remarks and outlook.

The objective of the thesis have been to optimise the synthesis of a new type of nano particular deNO$_x$ catalyst, towards a possible upscaling. In this process a new synthesis route has been found, that yields more active catalysts and are easier to upscale. In this process each of the synthesis steps have been investigated and the importance of each step evaluated. Especially the solvent and acid did turnout to have a very large impact on the resulting activity of the catalyst. Furthermore the potassium resistance was optimised by acidifying the catalyst in two different steps with H$_2$SO$_4$. However most importantly a simple synthesis of the vanadium precursor was found.

In order to shape the optimised catalyst, it was mixed with sepiolite, making a plate type catalyst prototype. Exposure in a potassium aerosol for 632 hours showed a further increase of the potassium resistance, owed to the physical blocking of potassium by sepiolite fibres. Exceeding the potassium resistance of the industrial reference by a great margin, 32% deactivation compared to 84%. With the higher initial activity of the nano catalyst it still exceeds the activity of the fresh industrial reference after aerosol exposure.

Activity measurements under realistic conditions proved that the catalyst did not deactivate, due to neither temperature induced sintering nor irreversible sulphation of SO$_2$. The big concern of SO$_2$ oxidation was also rejected by SO$_2$ oxidation measurements. Displaying very low activity for the nano particular deNO$_x$ catalyst, even lower than a low vanadia industrial reference.

Finally a mechanistic study shed light on how the catalyst works under reaction conditions. Most importantly it was showed that the V=O bond did not break during the SCR reaction. Suggesting that another oxygen on the active vanadia site is responsible for the SCR reactivity.

Ammonia adsorption studies demonstrated that the amount of $NH_3$ adsorbed exceeded the number of active sites many times, explaining the lack of increased activity upon sulphation. On the other hand potassium deactivation of a sulphated catalyst showed that potassium reacted with the tridentate sulphate species on the surface, explaining the increased potassium resistance due to sulphation.

The next step towards an industrial size catalyst, is making a honeycomb structured monolith pilot. Making activity tests, potassium resistance and $SO_2$ oxidation.
At the time of writing funding has been sought to pursue this and an industrial partner has been found.

# Bibliography

[1] Chorkendorff, I.; Niemantsverdriet, H. *Concepts of Modern Catalysis and Kinetics;* Wiley-VCH, second ed., 2007.

[2] Bosch, H.; Janssen, F. *Catal. Today* **1988**, *2*, 369–379.

[3] Roy, S.; Hegde, M.; Madras, G. *Appl. Energy* **2009**, *86*, 2283–2297.

[4] Parvulescu, V.; Grange, P.; Delmon, B. *Catal. Today* **1998**, *46*, 233–316.

[5] UNECE EB. Protocol to abate acidification, eutrophication and ground-level ozone. 30 November , **1999**.

[6] Finansministeriet. Aftaler om finansloven 20 November , **2012**.

[7] Kustov, A.; Rasmussen, S.; Fehrmann, R.; Simonsen, P. *Appl. Catal. B* **2007**, *76*, 9–14.

[8] Bosch, H.; Janssen, F. *Catal. Today* **1988**, *2*, 381–401.

[9] Xie, S.; Rosynek, M. P.; Lunsford, J. H. *J. Catal.* **1999**, *188*, 24–31.

[10] Shin, S.; Hatakeyama, Y.; Ogawa, K.; Shimoura, K. *Mat. Res. Bull.* **1979**, *14*, 133–136.

[11] Iwakuni, H.; Shinmyou, Y.; Hiroshi Yano, H. M.; Ishihara, T. *Appl. Catal. B* **2007**, *74*, 299–306.

[12] He, H.; Dai, H.; Ngan, K.; Au, C. *Catal. Lett.* **2001**, *71*, 147–153.

[13] Chang, Y. F.; McCarty, J. G. *J. Catal.* **1998**, *178*, 408–413.

[14] Bae, S. W.; Roh, S. A.; Kim, S. D. *Chemosphere* **2006**, *65*, 170–175.

[15] Janssen, F.; Meijer, R. *Catal. Today* **1993**, *16*, 157–185.

[16] Busca, G.; Lietti, L.; Ramis, G.; Berti, F. *Appl. Catal. B* **1998**, *18*, 1–36.

[17] Forzatti, P. *Appl. Catal. A* **2001**, *222*, 221–236.

[18] Iwasaki, M.; Shinjoh, H. *Appl. Catal. A* **2010**, *390*, 71–77.

[19] Koebel, M.; Madia, G.; Raimondi, F.; Wokaun, A. *J. Catal.* **2002**, *209*, 159–165.

[20] Inomata, M.; Miyamoto, A.; Murakami, Y. *J. Catal.* **1980**, *62*, 140–148.

[21] Wong, W. C.; Nobe, K. *Ind. Eng. Chem. Prod. Res. Dev.* **1984**, *23*, 564–568.

[22] Marangozis, J. *Ind. Eng. Chem. Res.* **1992**, *31*, 987–994.

[23] Pinoy, L.; Hosten, L. *Catal. Today* **1993**, *17*, 151–158.

[24] Wachs, I. E.; Saleh, R. Y.; Chan, S. S.; Chersich, C. C. *Appl. Catal.* **1985**, *15*, 339–352.

[25] Bulushev, D. A.; Kiwi-Minsker, L.; Zaikovskii, V. I.; Renken, A. *J. Mol. Catal.* **2000**, *193*, 145–153.

[26] Avila, P.; Montes, M.; Miró, E. E. *Chem. Eng. J.* **2005**, *109*, 11–36.

[27] Went, G. T.; Leu, L.-J.; Rosin, R. R.; Bell, A. T. *J. Catal.* **1992**, *134*, 492–505.

[28] Bond, G. C.; Tahir, S. F. *Appl. Catal.* **1991**, *71*, 1–31.

[29] Chen, J.; Yang, R. *Appl. Catal. A* **1992**, *80*, 135–148.

[30] Gao, R.; Zhang, D.; Liu, X.; Shi, L.; Maitarad, P.; Li, H.; Zhangb, J.; Cao, W. *Catal. Sci. Technol.* **2013**, *3*, 191–199.

[31] Sato, S.; Yu.u, Y.; Yahiro, H.; Mizuno, N.; Iwamoto, M. *Appl. Catal.* **1991**, *70*, L1–L5.

[32] Putluru, S. S. R.; Kristensen, S. B.; Due-Hansen, J.; Riisager, A.; Fehrmann, R. *Catal. Today* **2012**, *184*, 192–196.

[33] Brandenberger, S.; Kröcher, O.; Tissler, A.; Althoff, R. *Catal. Rev.* **2008**, *50*, 492–531.

[34] Sohn, J. R.; Kim, H. W. *J. Mol. Catal.* **1989**, *52*, 361–374.

[35] Morterra, C.; Cerrato, G.; Pinna, F.; Signoretto, M. *J. Catal.* **1995**, *157*, 109–123.

[36] Ramis, G.; Busca, G.; Bergani, F.; Forzatti, P. *Appl. Catal.* **1990**, *64*, 259–278.

[37] Topsoe, N. Y. *Science* **1994**, *265*, 1217.

[38] Ramis, G.; Busca, G.; Turco, M.; Kontur, E.; Willey, R. J. *J. Catal.* **1995**, *157*, 523–535.

[39] Ramis, G.; Yi, L.; Busca, G. *Catal. Today* **1996**, *28*, 373–380.

[40] Ramis, G.; Busca, G.; Bergani, F.; Forzatti, P. *Appl. Catal.* **1990**, *64*, 243–257.

[41] Topsøe, N.; Topsøe, H.; Dumesic, J. *J. Catal.* **1995**, *151*, 226–240.

[42] Busca, G.; Centi, G.; Marchetti, L.; Trifiro, F. *Langmuir* **1986**, *2*, 568–577.

[43] Lietti, L.; Alemany, J.; Forzatti.; Busca, G.; Ramis, G.; Giamello, E.; Bregani, F. *Catal. Today* **1996**, *29*, 143–148.

[44] Busca, G.; Saussey, H.; Saur, O.; Lavalley, J. C.; Lorenzelli, V. *Appl. Catal.* **1985**, *14*, 245–260.

[45] Arata, K.; Hino, M. *Mater. Chem. Phys.* **1990**, *26*, 213–237.

[46] Hu, S.; Apple, T. M. *J. Catal.* **1996**, *158*, 199–204.

[47] Topsøe, N.; Topsøe, H.; Dumesic, J. *J. Catal.* **1991**, *128*, 499–511.

[48] Tronconi, E.; Lietti, L.; Forzatti, P.; Malloggi, S. *Chem. Eng. Sci.* **1996**, *51*, 2965–2970.

[49] Lietti, L.; Nova, I.; Camurri, S.; Tronconi, E.; Fonatti, P. *AIChE J.* **1997**, *43*, 2559–2570.

[50] Takagi, M.; Kawai, T.; Soma, M.; Onishi, T.; Tamaru, K. *J. Catal.* **1977**, *50*, 441–446.

[51] Oridozola, J.; Heinemann, H.; Somorjai, G. A.; Pereira, J. *J. Catal.* **1989**, *119*, 71–82.

[52] Wachs, I. E.; Deo, G.; Weckhuysen, B. M.; Andreini, A.; Vuurman, M. A.; de Boer, M.; Amiridis, M. D. *J. Catal.* **1996**, *161*, 211–221.

[53] Ozkan, U. S.; Cai, Y.; Kumthekar, M. W. *J. Phys. Chem.* **1995**, *99*, 2363–2371.

[54] Topsøe, N.; Dumesic, J.; Topsøe, H. *J. Catal.* **1995**, *151*, 241–252.

[55] Dumesic, J. A.; Topsøe, N.; Topsøe, H.; Chen, Y.; Slabiak, T. *J. Catal.* **1996**, *163*, 409–417.

[56] Inomata, M.; Miyamoto, A.; Ui, T.; Kobayashi, K.; Murakami, Y. *Ind. Eng. Chem. Prod. Res. Dev.* **1982**, *21*, 424–428.

[57] Inomata, M.; Miyamoto, A.; Murakami, Y. *Ind. Eng. Chem. Prod. Res. Dev.* **1981**, *85*, 2372–2377.

[58] Janssen, F. J. J. G.; Kerkhof, F. M. G.; Bosch, H.; Ross, J. R. H. *J. Phys. Chem.* **1987**, *91*, 5921–5927.

[59] Janssen, F. J. J. G.; Kerkhof, F. M. G.; Bosch, H.; Ross, J. R. H.

*J. Phys. Chem.* **1987**, *91*, 6633–6638.

[60] Rajadhyaksha, R. A.; Knözinger, H. *Appl. Catal.* **1989**, *51*, 81–92.

[61] Miyata, H.; Nakagawa, Y.; Ono, T.; Kubokawa, Y. *Chem. Lett.* **1983**, *8*, 1141–1144.

[62] Y. V. Belokopytov, K. M. K.; Gerei, S. V. *J. Catal.* **1979**, *60*, 1–7.

[63] Farber, M.; Harris, S. P. *J. Phys. Chem.* **1984**, *88*, 680–682.

[64] Calatayud, M.; Minot, C. *J. Phys. Chem. B* **2004**, *108*, 15679–15685.

[65] Gilardoni, F.; Weber, J.; Baiker, A. *Int. J. Quant. Chem.* **1997**, *61*, 683–688.

[66] Gilardoni, F.; Weber, J.; Baiker, A. *J. Phys. Chem.* **1997**, *101*, 6069–6079.

[67] Katada, N.; Tsubaki, T.; Niwa, M. *Appl. Catal. A* **2008**, *340*, 76–86.

[68] Anstrom, M.; Dumesic, J. A.; Topsøe, N. Y. *Catal. Lett.* **2002**, *78*, 281–289.

[69] Anstrom, M.; Topsøe, N. Y.; Dumesic, J. A. *J. Catal.* **2003**, *213*, 115–125.

[70] Engel, T. *Quantum Chemestry;* Pearson Education, first ed., 2006.

[71] Soyer, S.; Uzun, A.; Senkan, S.; Onal, I. *Catal. Today* **2006**, *118*, 268–278.

[72] Vittadini, A.; Casarin, M.; Selloni, A. *J. Phys. Chem. B* **2005**, *109*, 1652–1655.

[73] Gottwald, U.; Monkhouse, P.; Wulgaris, N.; Bonn, B. *Fuel Process. Technol.* **2002**, *75*, 215–226.

[74] Oleschko, H.; Schimroczyk, A.; Lippert, H.; Müller, M. *Fuel* **2007**, *86*, 2275–2282.

[75] Wiles, C. C. *J. Hazard. Mater.* **1996**, *47*, 325–344.

[76] Zheng, Y.; Jensen, A. D.; Johnsson, J. E. *Appl. Catal. B* **2005**, *60*, 253–264.

[77] Kling, Å.; Andersson, C.; Myringer, Å.; Eskilsson, D.; Järås, S. G. *Appl. Catal. B* **2007**, *69*, 240–251.

[78] Gulyurtlu, I.; Crujeira, T.; Lopes, M. H.; Abelha, P.; Boavida, D.; Seabra, J.; Goncalves, R.; Sargaco, C.; Cabrita, I. *J. Energy Resour. Technol.* **2002**, *128*, 123–127.

[79] Forzatti, P.; Lietti, L. *Catal. Today* **1999**, *52*, 165–181.

[80] Kamata, H.; Ohara, H.; Takahashi, K.; Yukimura, A.; Seo, Y. *Catal. Lett.* **2001**, *73*, 79–83.

[81] Lisi, L.; Lasorella, G.; Malloggi, S.; Russo, G. *Appl. Catal. B* **2004**, *50*, 251–258.

[82] Chen, J.; Yang, R. T. *J. Catal.* **1990**, *125*, 411–420.

[83] Calatayud, M.; Minot, C. *J. Phys. Chem. C* **2007**, *111*, 6411–6417.

[84] Martín, C.; Martín, I.; del Moral, C.; Rives, V. *J. Catal.* **1994**, *146*, 415–421.

[85] Due-Hansen, J.; Boghosian, S.; Kustov, A.; Fristrup, P.; Tsilomelekis, G.; StÅhl, K.; Christensen, C. H.; Fehrmann, R. *J. Catal.* **2007**, *251*, 459–473.

[86] Lietti, L.; Forzatti, P.; Ramis, G.; Busca, G.; Bregani, F. *Appl. Catal. B* **1993**, *3*, 13–35.

[87] Kamata, H.; Takahashi, K.; Odenbrandb, C. I. *J. Mol. Catal. A* **1999**, *139*, 189–198.

[88] Kroöcher, O.; Elsener, M. *Appl. Catal. B* **2008**, *75*, 215–227.

[89] Zheng, Y.; Jensen, A. D.; Johnsson, J. E.; Thøgersen, J. R. *Appl. Catal. B* **2008**, *83*, 186–194.

[90] Castellino, F.; Jensen, A. D.; Johnsson, J. E.; Fehrmann, R. *Appl. Catal. B* **2009**, *86*, 196–205.

[91] Castellino, F.; Jensen, A. D.; Johnsson, J. E.; Fehrmann, R. *Appl. Catal. B* **2009**, *86*, 206–215.

[92] Klimczak, M.; Kern, P.; Heinzelmann, T.; Lucas, M.; Claus, P. *Appl. Catal. B* **2010**, *95*, 39–47.

[93] Wieck-Hansen, K.; Overgaard, P.; Larsen, O. *Biomass Bioenergy* **2000**, *19*, 395–409.

[94] Strege, J. R.; Zygarlicke, C. J.; Folkedahl, B. C.; McCollor, D. P. *Fuel* **2008**, *87*, 1341–1347.

[95] van Hengstum, A. J.; Pranger, J.; van Ommen, J. G.; Gellings, P. J. *Appl. Catal.* **1984**, *11*, 317–330.

[96] Zheng, Y.; Jensen, A. D.; Johnsson, J. E. *Ind. Eng. Chem. Res.* **2004**, *43*, 941–947.

[97] Witko, M.; Grybos, R.; Tokarz-Sobieraj, R. *Top. Catal.* **2008**, *38*, 105–115.

[98] Nicosia, D.; Czekaj, I.; Kröcher, O. *Appl. Catal. B* **2008**, *77*, 228–236.

[99] Kiwi-Minsker, L.; Bulushev, D. A.; Rainone, F.; Renken, A. *J. Mol. Catal. A* **2002**, *184*, 223–235.

[100] Lewandowska, A. E.; Calatayud, M.; Lozano-Diz, E.; Minot, C.; Bañares, M. A. *Catal. Today* **2008**, *139*, 209–213.

[101] Due-Hansen, J.; Kustov, A. L.; Rasmussen, S. B.; Fehrmann, R.; Christensen, C. H. *Appl. Catal. B* **2006**, *66*, 161–167.

[102] Du, X.; Gao, X.; Qu, R.; Ji, P.; Luo, Z.; fa Cen, K. *Chem. Cat. Chem.* **2013**, *4*, 2075–2081.

[103] Kristensen, S.; Kunov-Kruse, A.; Riisager, A.; Rasmusen, S.; Fehrmann, R. *Patent Nano-particular metal oxide catalysts (EP 08169238.6)* **2008**.

[104] Kunov-Kruse, A. J.; Kristensen, S. B.; Riisager, A.; Rasmussen, S. B.; Fehrmann, R. *J. Mater. Sci.* **2009**, *44*, 323–327.

[105] Kristensen, S. B.; Kunov-Kruse, A. J.; Riisager, A.; Rasmussen, S. B.; Fehrmann, R. *J. Catal* **2011**, *284*, 60–67.

[106] Huang, Z.; Gu, X.; Wen, W.; Hu, P.; Makkee, M.; Lin, H.; Kapteijn, F.; Tang, X. *Angew. Chem. Int. Ed.* **2013**, *52*, 660–664.

[107] Park, T. S.; Jeong, S. K.; Hong, S. H.; Hong, S. C. *Ind. Eng. Chem. Res.* **2001**, *40*, 4491–4495.

[108] Jin, R.; Liu, Y.; Wu, Z.; Wang, H.; Gu, T. *Catal. Today* **2010**, *153*, 84–89.

[109] Koparde, V. N.; Cummings, P. T. *J. Phys. Chem. B* **2005**, *109*, 24280–24287.

[110] Koparde, V. N.; Cummings, P. T. *J. Nanopart. Res.* **2008**, *10*, 1169–1182.

[111] Moulijn, J. A.; van Diepen, A. E.; Kapteijn, F. *Appl. Catal. A* **2001**, *212*, 3–16.

[112] Jian, L.; Gongbao, S.; Meili, W.; Baoshu, Z. *Chinese journal of high pressure physics* **2006**, *20*, 211–216.

[113] Djerdj, I.; Tonejc, A. *J. Alloys Compd.* **2006**, *413*, 159–174.

[114] Lide, D. R. *Handbook of chemistry and physics - A Ready-reference Book of Chemical and Physical Data;* CRC, 2007.

[115] Scherrer, P. *Göttinger Nachrichten Math. Phys.* **1918**, *2*, 98–100.

[116] Ståhl, K. http://struktur.kemi.dtu.dk/kenny/kshome.html, **2012**.

[117] Fogler, H. S. *Elements of chemical reaction engineering;* Prentice Hall PTR, 1999.

[118] Wong, W. C.; Nobe, K. *Ind. Eng. Chem. Prod. Res. Dev.* **1986**, *25*, 179–186.

[119] Long, R. Q.; Yang, R. T. *J. Catal.* **2000**, *196*, 73–85.

[120] Hari-Bala.; Zhao, J.; Jiang, Y.; Ding, X.; Tian, Y.; Yu, K.; Wang, Z. *Mater. Lett.* **2005**, *59*, 1937–1940.

[121] Hari-Bala.; Zhao, J.; Jiang, Y.; Ding, X.; Tian, Y.; Yu, K.; Wang, Z. *Mater. Lett.* **2006**, *60*, 494–498.

[122] Prandtl, W.; Hess, L. *Anorg. Allg. Chem.* **1913**, *82*, 103–129.

[123] Glifiski, M. *Appl. catal. A* **1997**, *164*, 205–209.

[124] Lachowicz, V. A.; Höbold, W.; Thiele, K. H. *Z. Anorg. Allg. Chem.* **1975**, *434*, 65–71.

[125] Toxicology and carcinogesis studies of vanadium pentoxide NTP technical report, NTP, **2002**.

[126] Vanadium pentoxide Monographs on the evaluation of carcinogenic risks to humans 86, IARC, **2006**.

[127] Livage, J.; Sanches, C. *J. Non-Cryst. Solids* **1992**, *145*, 11–19.

[128] Sanches, C.; Livage, J.; Henry, M.; Babonneau, F. *J. Non-Cryst. Solids* **1988**, *100*, 65–76.

[129] Livage, J. *Chem. Mater.* **1991**, *3*, 578–593.

[130] Harris, M. T.; Byers, C. H. *J. Non-Cryst. Solids* **1988**, *103*, 49–64.

[131] Chen, H. C.; Wang, L.; Chiu, W. Y. *J. Non-Cryst. Solids* **1992**, *145*, 11–19.

[132] Ding, X. Z.; Liu, X. H. *Mater. Sci. Eng.* **1997**, *224*, 210–215.

[133] Pruckmayr, G.; Wu, T. K. *Macromolecules* **1978**, *11*, 662–668.

[134] Jiang, J.; Oberdörster, G.; Biswas, P. *J. Nanopart Res.* **2009**, *11*, 77–89.

[135] Mpandou, A.; Siffert, B. *J. Colloid Interface Sci.* **1984**, *102*, 138–145.

[136] Shahini, S.; Askari, M.; Sadrnezhaad, S. K. *Bull. Mater. Sci.* **2011**, *34*, 1189–1195.

[137] Sakvaoati, G. S.; Ramanamurty, K. V.; Janardanarao, M. *J. Mol. Catal.* **1989**, *54*, 9–30.

[138] Mujumdar, A. *Handbook of Industrial Drying*, number vb. 1 in Handbook of Industrial Drying; Dekker, 1995.

[139] Lietti, L.; Nova, I.; Forzatti, P. *Appl. Catal. A* **2000**, *11-12*, 111–122.

[140] Forzatti, P.; Ballardini, D.; Sighicelli, L. *Catal. Today* **1998**, *41*, 87–94.

[141] Boger, T.; Heibel, A. K.; Sorensen, C. M. *Ind. Eng. Chem. Res.* **2004**, *43*, 4602–4611.

[142] Sarup, B.; Nielsen, P. E. H.; Hansen, V. L.; Johansen, K. *U.S. Patent 5,217,936,* **1992**.

[143] Suárez, S.; Yates, M.; Avila, P.; Blanco, J. *Catal. Today* **2005**, *105*, 499–506.

[144] Santos, A.; Bahamonde, A.; Avila, P.; García-Ochoa, F. *Appl. Catal. B* **1996**, *8*, 299–314.

[145] Knapp, C.; Gil-Llambías, F. J.; Gulppi-Cabra, M.; Avila, P.; .; Blanco, J. *J. Mater. Chem.* **1997**, *7*, 1641–1645.

[146] Bahamonde, A.; Beretta, A.; Avila, P.; Tronconi, E. *Ind. Eng. Chem. Res.* **1996**, *35*, 2516–2521.

[147] Odenbrand, C. U. I.; Bahamonde, A.; Avila, P.; Blanco, J. *Appl. Catal. B* **1994**, *5*, 117–131.

[148] Sanabria, N.; Ávila, P.; Yates, M.; Rasmussen, S.; Molina, R.;

Moreno, S. *Appl. Clay. Sci.* **2010**, *47*, 283–289.

[149] Frost, R. L.; Kristóf, J.; Horváth, E. *J. Therm. Anal. Calorim.* **2009**, *98*, 423–428.

[150] Yebra-Rodríguz, A.; Martín-Ramos, J. D.; del Rey, F.; Viseras, C.; López-Galindo, A. *Clay Minerals* **2003**, *38*, 353–360.

[151] Tartaglione, G.; Tabuani, D.; Camino, G. *Microporous Mesoporous Mater.* **2008**, *107*, 161–168.

[152] Nagata, H.; Shimoda, S.; Sudo, T. *Clays Clay Miner.* **1974**, *22*, 285–293.

[153] Clarence, R. S.; Earl, S. V. *J. Am. Ceram. Soc.* **1926**, *9*, 77–96.

[154] Orolínová, Z.; ciaková, A. M. *Mater. Chem. Phys.* **2009**, *114*, 956–961.

[155] Turco, M.; Lisi, L.; Pirone, R. *Appl. Catal. B* **1994**, *3*, 133.

[156] Topsøe, N.-Y.; Slabiak, T.; Clausen, B. S.; Srnak, T. Z.; Dumesic, J. *J. Catal.* **1992**, *134*, 742–746.

[157] Matsuda, S.; Kamo, T.; Kato, A.; Nakajima, F. *Ind. Eng. Chem. Prod. Res. Develop.* **1982**, *21*, 48–52.

[158] Forzatti, P. *Catal. Today* **2000**, *62*, 51–65.

[159] Ivanov, A.; Balzhinimaev, B. *React. Kin. Catal. Lett.* **1987**, *35*, 413–424.

[160] Tronconi, E.; Beretta, A.; Elmi, A.; Forzatti, P.; Malloggi, S.; Baldacci, A. *Chem. Eng. Sci.* **1994**, *49*, 4277–4287.

[161] Reger, D. L.; Goode, S. R.; Ball, D. W. *Chemistry: Principles and Practice;* Mary Finch, first ed., 2009.

[162] Putluru, S. S. R.; Jensen, A. D.; Riisager, A.; Fehrmann, R. *Catal. Commun.* **2012**, *18*, 41–46.

[163] Rasmussen, S. B.; Perez-Ferreras, S.; Bañares, M. A.; Bazin, P.; .; Daturi, M. *J. Phys. Chem. B* **2013**, *3*, 86–94.

[164] Hausinger, G.; Schmelz, H.; Knözinger, H. *Appl. Catal.* **1988**, *39*, 267–283.

[165] Saur, O.; Bensitel, M.; Saad, A. M.; Lavalley, J. C. *J. Catal.* **1986**, *99*, 104–110.

[166] Waqif, M.; Bachelier, J.; Saur, O.; Lavalley, J.-C. *J. Mol. Catal.* **1992**, *72*, 127–138.

[167] Desmartin-Chomel, A.; Flores, J. L.; Bourane, A.; Clacens, J. M.; Figueras, F.; Delahay, G.; Fendler, A. G.; Lehaut-Burnouf, C. *J. Phys. Chem. B* **2006**, *110*, 858–863.

[168] Cornaglia, L.; Lombardo, E.; Andersen, J.; Fierro, J. G. *Appl. Catal. A* **1993**, *1*, 37–50.

[169] Lewandowska, A. E.; Calatayud, M.; Tielens, F.; Bãnares, M. A. *J. Phys. Chem. C* **2011**, *115*, 24133–24242.

[170] Went, G. T.; Leu, L. J.; Bell, A. T. *J. Catal.* **1992**, *134*, 479–491.

[171] Went, G. T.; Leu, L.-J.; Lombardo, S. J.; Bell, A. T. *J. Phys. Chem.* **1992**, *96*, 2235–2241.

[172] Tongelen, M. V. *J. Catal.* **1966**, *5*, 535–537.

[173] Bensitel, M.; Saur, O.; Lavalley, J. C. *Mater. Chem. Phys.* **1988**, *19*, 147–156.

[174] Hofmann, A.; Sauer, J. *J. Phys. Chem. B* **2004**, *108*, 14652–14662.

[175] Kanougi, T.; Atoguchi, T.; Yao, S. *J. Mol. Catal. A* **2002**, *177*, 289–298.

[176] Haase, F.; Sauer, J. *J. Am. Chem. Soc.* **1998**, *120*, 13503–13512.

[177] Giakoumelou, I.; Fountzoula, C.; Kordulis, C.; Boghosian, S. *J. Catal.* **2006**, *239*, 1–12.

[178]   Wachs, I. E.; Weckhuysen, B. M. *Appl. Catal. A* **1997**, *157*, 67–90.

[179]   Wachs, I. E. *Catal. Today* **1996**, *27*, 437–455.

[180]   Christodoulakis, A.; Machli, M.; Lemonidou, A. A.; Boghosian, S. *J. Catal.* **2004**, *222*, 293–306.

[181]   Brázdováand, V; Ganduglia-Pirovano, M. V; Sauer, J. *J. Phys. Chem. B* **2005**, *109*, 394–400.

# A

## Detailed experimental

### A.1. Synthesis

For synthesis of approx. 1.5 g of optimised nano-catalyst a mixture 0.489 g $NH_4Cl$ and 4.935 g $H_2O$ was added drop wise to a 0 °C solution under stirring comprising 4.25 g of titanium iso-propoxide, 0.668 g vanadium ethoxide, 25 g ethanol and 0.0250 g $H_2SO_4$. After gelation the sol-gel is aged at room temperature for 4 hours and then transferred to 10 cm petridish and dried in a ventilated oven at 85°C for 100 hours. Every ca. 25 hours the powder is ground to a fine powder. After the 100 hours the powder is calcined at 400 °C for 2 hours with a heating rate of 33 $°C/_{hour}$.

### A.2. Synthesis of promoted catalysts

Tungsten promoted catalysts was synthesised by incipient wetness impregnation of a 15 wt.% $V_2O_5/TiO_2$ catalyst using an aqueous solution of ammonium meta tungstenate (Sigma-Aldrich 98%) with the appropriate concentration.

Molebdenum promoted catalysts was synthesised by adding an ethanolic solution of Bis (acety-lacetonato) dioxomolybdenum(VI) (99% Sigma-Aldrich) after synthesis step ⑤.

### A.3. Activity measurements

Activity measurements under realistic conditions with a flue gas comprising NO, $NH_3$, $O_2$, $SO_2$ and He as carrier, was performed using a Perkin Elmer Lambda 1000 UV/VIS spectrophotometer. In Figure A.1 on the next page the spectra of $NH_3$, NO and a combination of the two
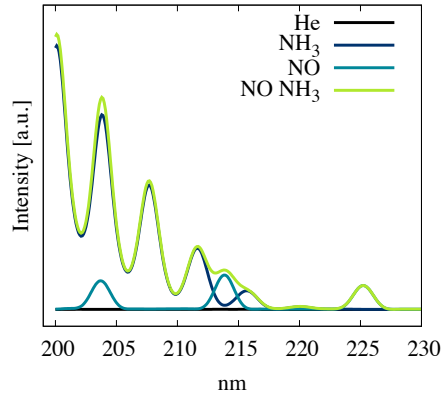
**Figure A.1.:** *UV-VIS spectrum of different SCR gases, band at 225.4 nm is used to measure the concentration of NO and the 208 nm band as a measure for NH$_3$*

depicted, for conveniance the determination of the NO concentration the band at 225 nm was used, because it is not interfering with the NH$_3$ bands.

# B

## Supplementary figures

Supplementary figures, see Figure text for explanation.

## Vanadium precuorsor
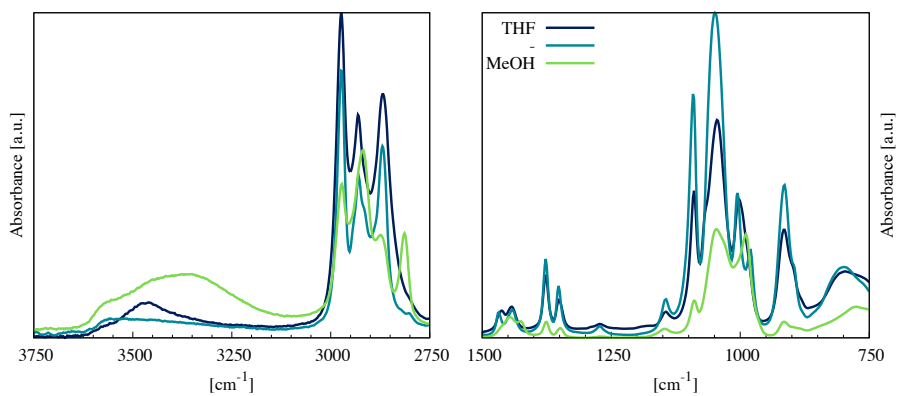


**Figure B.1.:** *Liquid ATR FTIR of vanadium ethoxide in two different solvents.*

## FTIR studies
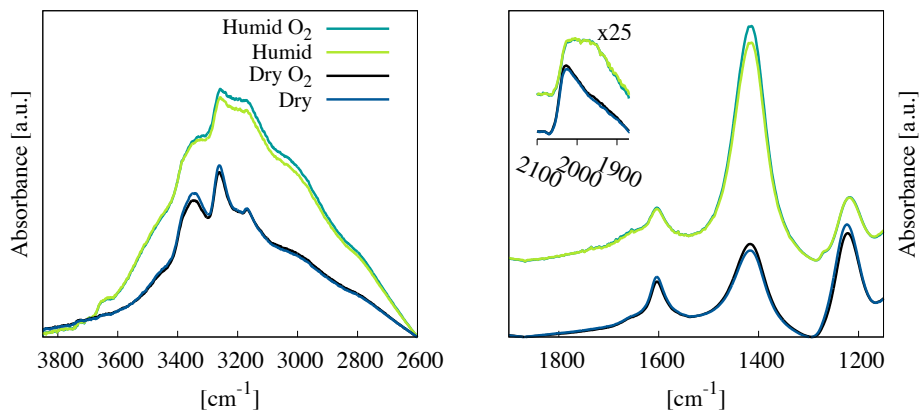


**Figure B.2.:** *In-situ steady state adsorption spectra of NH$_3$ with and without present O$_2$*
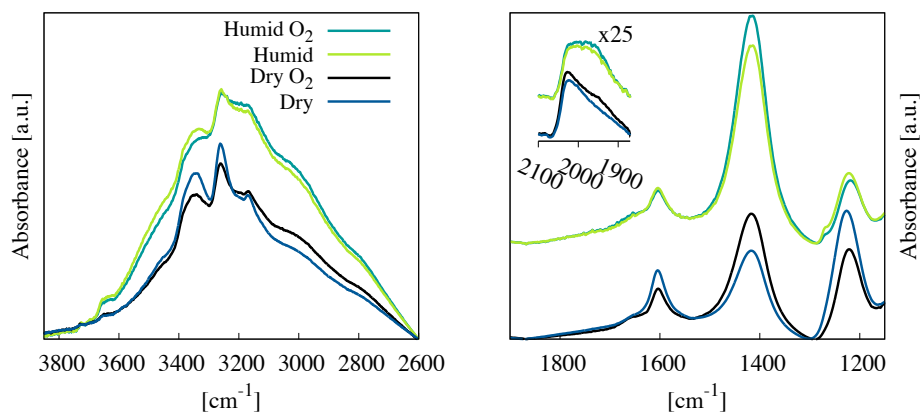


**Figure B.3.:** *In-situ FTIR spectra of a 20 wt.% V$_2$O$_5$/TiO$_2$ under working conditions at 250 °C. Two spectra are measured under humid conditions and two under dry conditions with and without O$_2$.*
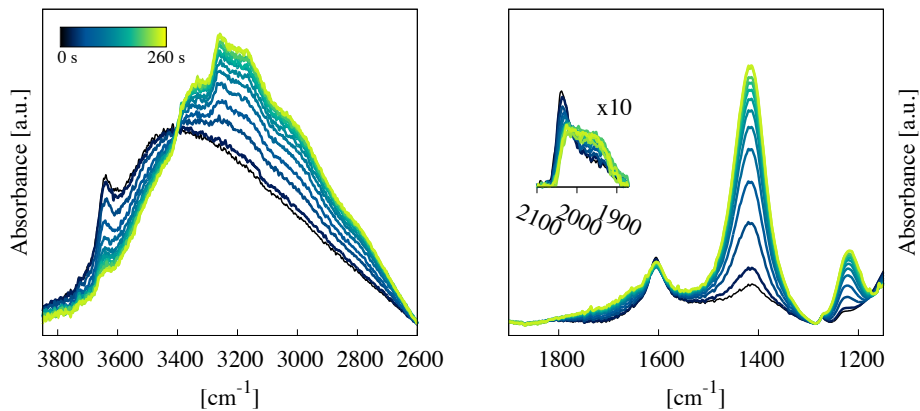
**Figure B.4.:** *In-situ FTIR spectra of NH$_3$ adsorption on a unsulphated 20 wt.% V$_2$O$_5$/TiO$_2$ , under humid conditions (∼2% H$_2$O). Time resolution is 1 spectrum pr. 20 second.*
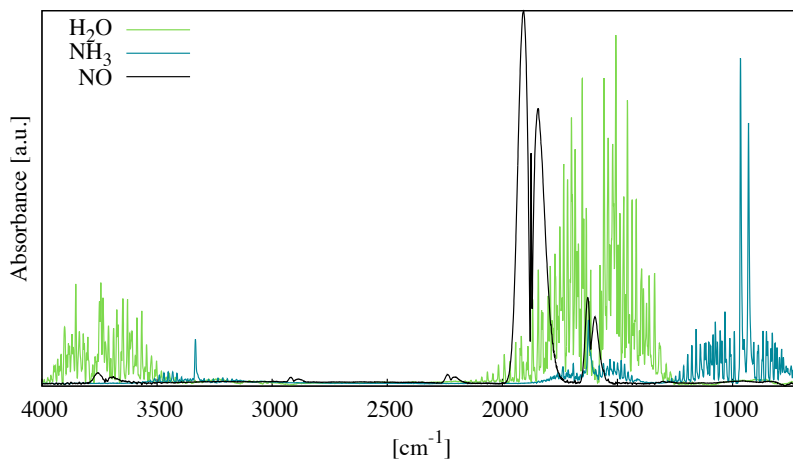


**Figure B.5.:** *Background FTIR spectra of NH$_3$, H$_2$O and NO gases.*

## Raman studies
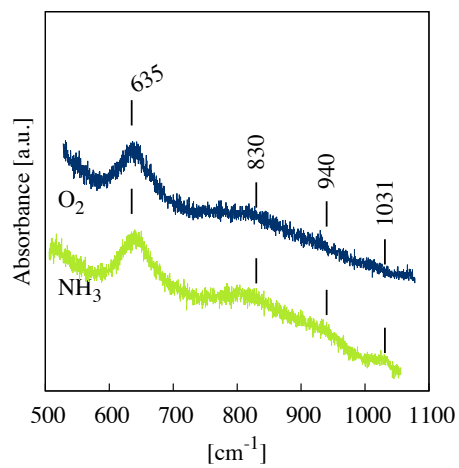


**Figure B.6.:** *In-situ Raman spectra of a 20 wt.% $V_2O_5/TiO_2$ catalyst synthesised with $HNO_3$, $NH_4Cl$ and THF. Measured under flowing $O_2$ and $NH_3/N_2$ at 250 °C.*

## Potassium deactivation
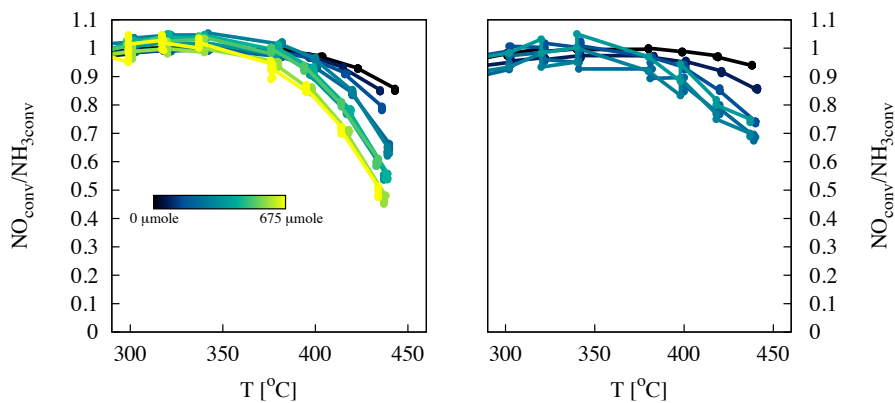


**Figure B.7.:** *Selectivity of potassium doped catalysts (0-675 μmole/g in steps of 75 μmole/g), expressed as $[NO_{conv.}]/[NH_{3conv.}]$ of a 20 wt.% $V_2O_5/TiO_2$ **(left)** and an industrial reference **(right)***
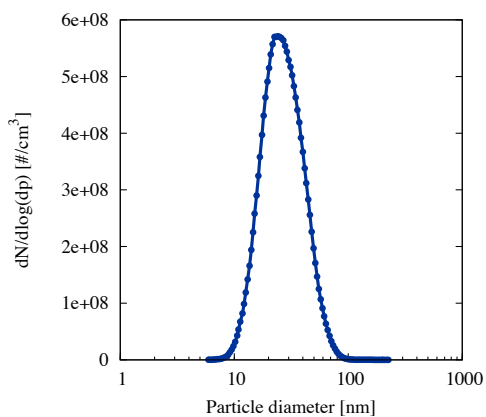


**Figure B.8.:** **(Left)** *reactor without heating element and with cassette for catalyst plates.* **(Right)** *particle distribution of potassium aerosols.*

## Sepiolite ekstrudates



*(a)*



*(b)*



*(c)*
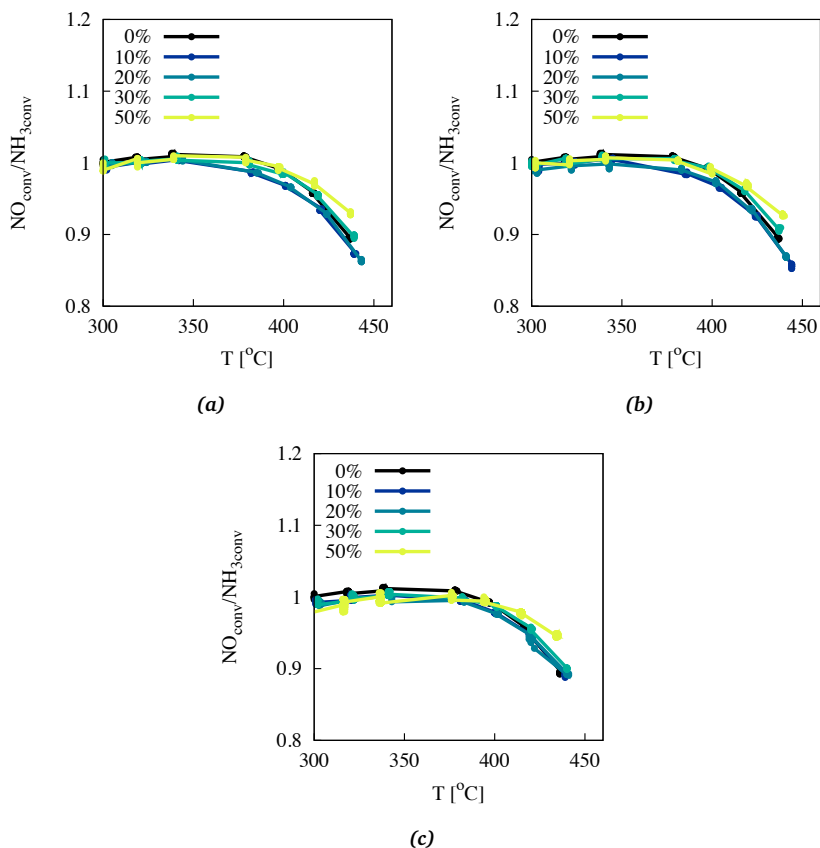
**Figure B.9.:** *Selectivity of sepiolite extrudates comprising 10, 20, 30, 50, 100 wt.% sepiolite and 20 wt.% $V_2O_5/TiO_2$ (optimised) extruded using **(a)** water, **(b)** aqueous solution of 0.05M $H_2SO_4$, **(c)** aqueous solution of 0.25M $H_2SO_4$. Selectivity is expressed as $[NO_{conv}]/[NH_{3conv}]$ of a 20 wt.%*



**Figure B.10.:** *Composite plate catalyst comprising a $SiO_2$ mesh and a 20 wt.% sepiolite / $V_2O_5/TiO_2$ mixture.*
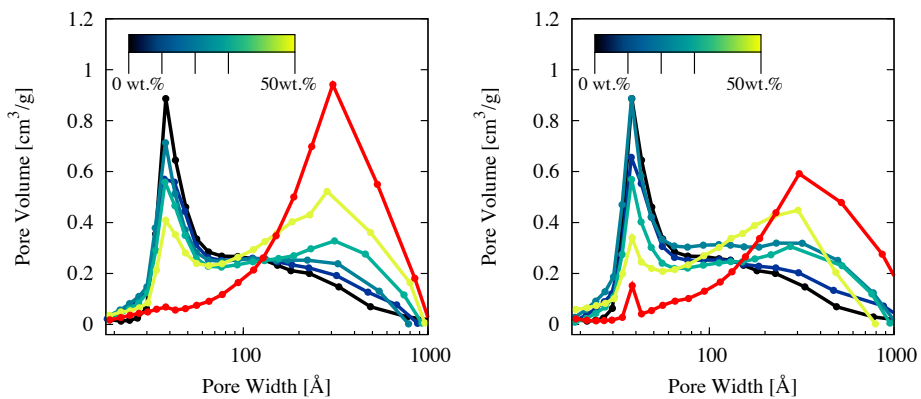
**Figure B.11.:** *Pore distribution of extrudates made using 10, 20, 30, 50, 100 wt.% sepiolite and 20 wt.% $V_2O_5/TiO_2$ catalyst (optimised) extruded using water, 0.05M* **(left)** *and 0.25M* **(right)** *$H_2SO_4$.*

## C

## Published articles

### Project related articles (enclosed in the document)

1 Kunov-Kruse, A.J.; Kristensen, S.B.; Riisager, A.; Rasmussen, S.B.; Fehrmann, R. "Seed-assisted sol-gel synthesis and characterization of nanoparticular $V_2O_5$/anatase" *J. Mater. Sci.* **2009**, *44*, 323-327.

2 Kristensen, S.B.; Kunov-Kruse, A.J.; Riisager, A.; Rasmussen, S.B.; Fehrmann, R. "High performance vanadia-anatase nanoparticle catalysts for the Selective Catalytic Reduction of NO by ammonia" *J. Catal* **2011**, *284*, 60-67.

3 Putluru, S.S.R.; Kristensen, S.B.; Due-Hansen, J.; Riisager, A.; Fehrmann, R. "Alternative alkali resistant deNO$_x$ catalysts" *Catal. Today* **2012**, *184*, 192-196

### Other published articles

4 Kunov-Kruse, A.J.; Kristensen, S.B.; Liu, C.; Berg, R.W. "Experimental and ab initio DFT calculated Raman spectrum of Sudan I, a red dye" *J. Raman Spectrosc.* **2011**, *42*, 1470-1478

5 Berg, R.W.; Riisager, A.; Buu, O.N.V.; Kristensen, S.B.; Fehrmann, R.; Harris, P.; Brunetti, A.C. "X-ray crystal structure, Raman spectroscopy, and ab initio density functional theory calculations on 1,1,3,3-tetramethylguanidinium bromide" *J. Phys. Chem. A* **2010**, *114*, 13175-13181

**Seed-assisted sol-gel synthesis and characterization of nanoparticular $V_2O_5$/anatase**

Kunov-Kruse, A.J.; Kristensen, S.B.; Riisager, A.; Rasmussen, S.B.; Fehrmann, R.

*J. Mater. Sci.* **2009**, *44*, 323-327

# Article

# 1

# Seed-assisted sol–gel synthesis and characterization of nanoparticular $V_2O_5$/anatase

Andreas J. Kruse · Steffen B. Kristensen ·
Anders Riisager · Søren B. Rasmussen ·
Rasmus Fehrmann

**Abstract** Nanoparticular supported vanadia materials with crystalline anatase support with a narrow size distribution around 12 nm have been synthesized by a new facile sol–gel, co-precipitation method using decomposable ammonium chloride seed crystals. The materials have been characterized by means of X-ray powder diffraction, transmission electron microscopy and nitrogen physisorption. The synthesized high-surface area anatase particles allowed a loading of up to 15 wt.% vanadia without exceeding monolayer coverage of $V_2O_5$ in contrast to typical analogous industrial catalysts which only can accommodate 3–5 wt.% vanadia. These materials are promising candidates for improved catalysts for, e.g., oxidation reactions and selective catalytic reduction of $NO_X$ in flue gases.

## Introduction

Vanadium oxides on inorganic support materials constitute the most important supported metal oxide catalysts in both heterogeneous and homogeneous industrial applications [1]. In these catalysts, the amount of active vanadium species exposed to the reactants vary with the type of support (typically $SiO_2$, $Al_2O_3$, $ZrO_2$, and $TiO_2$) and the loading of vanadium oxide on the carrier [2]. Here both the surface area and the oxide type (i.e., textural and surface properties) dictate the maximum amount that can be loaded before surpassing the monolayer coverage leading to crystalline $V_2O_5$ formation [3]. The prefered choice of support usually depends on the reactive environment of the catalyst during operation as well as the particular reaction in focus. Thus, it is well known that $TiO_2$, especially in the anatase form, is an excellent support for vanadium oxides making highly active materials for the selective catalytic reduction (SCR) of nitrogen oxides (i.e. deNO$_X$) by injection of ammonia in power plant flue-gases and other industrial off-gases [4]. The activity of the industrial $VO_X$/$TiO_2$-based SCR catalyst is limited by the surface area of the anatase carrier, since only up to one monolayer of the vanadium oxide species can be accepted corresponding to a vanadia loading of 3–5 wt.%. Increased loading results in decreased deNO$_X$ activity and increased ability to oxidize $NH_3$ and possibly also $SO_2$ in the flue gas [5]. One approach to improve the efficiency of catalytic materials is to prepare them as nano-sized particles (mean diameter, <100 nm), which in many reactions have shown to be far more reactive than bulk materials [6]. Hence, it is very likely that small catalyst particles of $VO_X$/$TiO_2$ will be able to reduce $NO_X$ with increased efficiency to comply with the demand for sufficiently activity during prolonged operation.

In this study, nano-sized particular vanadium oxide/anatase catalysts with vanadia loadings up to 25 wt.% and relatively high-surface areas are synthesized by a sol–gel, co-precipitation procedure involving concomitant hydrolysis of titanium(IV) and vanadium(V) alkoxides in presence of ammonium chloride seed crystals. The materials are further characterized by X-ray powder diffraction

A. J. Kruse · S. B. Kristensen · A. Riisager · R. Fehrmann (✉)
Department of Chemistry and Center for Sustainable and Green Chemistry, Technical University of Denmark, Building 207, 2800 Kgs. Lyngby, Denmark
e-mail: rf@kemi.dtu.dk

S. B. Rasmussen
Instituto de Catálisis y Petroleoquimica (ICP), Consejo Superior de Investigaciones Cientificas (CSIC), Marie Curie 2, Campus de UAM, 28020 Madrid, Spain

(XRPD), transmission electron microscopy (TEM), and nitrogen adsorption. To the best of our knowledge, this is the first report in the literature of sol–gel preparation of nano-sized metal oxide/$TiO_2$ using seed crystallization, while metal/$TiO_2$ catalyst materials have been synthesized previously, e.g. Pt/$TiO_2$ catalysts [7]. Analogous $VO_X$/$TiO_2$ materials have also earlier been prepared by hydrothermal methods [8, 9], mechanical blending [10], and flame synthesis [11, 12], and the latter evaluated for SCR deNO$_X$.

## Experimental

### Preparation of $VO_X$/anatase materials

Nano-sized particular vanadium oxide/anatase materials having a $V_2O_5$ content of 0–25 wt.% were obtained by calcination of materials prepared by a modified new sol–gel procedure [13, 14] involving concomitant hydrolysis of titanium(IV) isopropoxide (97%, Lancaster) and vanadium(V) oxytriethoxide (95%, Aldrich) in acidic ethanol solution in presence of ammonium chloride ($\geq$99.5%, Fluka) as crystallization germ.

In a typical preparation (here exemplified for a material containing 5.2 wt.% $V_2O_5$), a solution of 1.40 g $NH_4Cl$ (26.2 mmol) in 4 mL deionized water was added dropwise to a stirred, ice-cooled solution of 3.70 g Ti($i$-$C_3H_7O$)$_4$ (13.0 mmol), 0.72 g VO($C_2H_5O$)$_3$ (0.63 mmol), and 2.43 g glacial acetic acid (40.5 mmol) in 10 mL abs. ethanol. After addition of the aqueous solution, a yellowish gel was formed, which subsequently was aged 20 h under stirring before ethanol, liberated propanol, acetic acid, and excess water were removed under reduced pressure (0.2 mbar, 70–100 °C). Finally, the material was calcined (400 °C, 6 h) in an air stream (300 mL min$^{-1}$) to decompose the ammonium chloride template and convert the amorphous titania support into crystalline anatase.

### Characterization of $VO_X$/anatase materials

XRPDs of the prepared materials were recorded using Cu-K$\alpha$ radiation ($\lambda$ = 1.54056 nm) in the $2\theta$ interval 5–100° with a Huber G670 Guinier camera.

TEM was performed on a JEM 2000FX apparatus with an accelerating voltage of 300 kV. A suspension of about 2 mg of the powdered samples in 2 mL ethanol was sonicated for 1 h and allowed to settle for 15 min, before a drop was distributed on a 300-mesh copper grid coated with a carbon film with holes.

Nitrogen sorption data were obtained at liquid nitrogen temperature by using a Micromeritics ASAP 2020 apparatus. Before determination of nitrogen adsorption–desorption isotherms, the samples (ca. 0.4 g) were outgassed for 2 h at

200 °C under vacuum. The apparent specific surface areas ($S_{BET}$) were evaluated by two-parameter linear BET plots in the range $p/p_0$ = 0.065–0.2. The external areas ($S_{ext}$) were determined with the $t$-plot method [15, 16]. Due to perculation effects on the desorption branches [17] mesopore size distributions were obtained using data from the adsorption branches by assuming open nonintersecting cylindrical pores [18]. The thickness of the adsorbed layer at each relative pressure was obtained from the classical equation of Harkins and Jura.

## Results and discussion

XRPD analysis of the prepared vanadia-titania materials after calcination at 400 °C revealed only crystalline anatase support phase with no peaks originating from residual ammonium chloride template or crystalline $V_2O_5$ (Fig. 1). This also included the materials with high vanadia loadings $\geq$15 wt.% corresponding to more than a monolayer (see Table 1), thus indicating a high dispersion of an amorphous vanadia phase as typically found for oxide supported vanadia catalysts [15] due to the relatively low $V_2O_5$ Tammann temperature ($T_m$ = 209 °C). Likewise, broadening of the peaks indicated presence of relatively small anatase particles. Notable, however, less intensive peaks (e.g., at $2\theta$ = 28, 33, 43, 45, and 58°), possibly originating from an undisclosed mixed crystalline vanadia-titania phase, were observed for the materials with high vanadia loading. Vanadium cation promoted formation of $V_xTi_{1-x}O_2$ phases
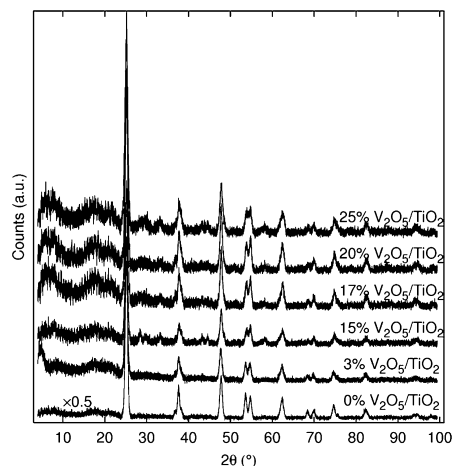


**Fig. 1** XRPDs of crystalline $VO_X$/anatase materials

**Table 1** Characteristics of VO$_X$/anatase materials

| V$_2$O$_5$ (wt.%) | S$_{BET}$ (m$^2$ g$^{-1}$) | S$_{ext}$ (m$^2$ g$^{-1}$) | $d_{particle}$ (nm) | | $n_s^c$ (V atoms nm$^{-2}$) |
|---|---|---|---|---|---|
| | | | BET$^a$ | XRPD$^b$ | |
| 0.0 | 73 | – | 21.1 | 15.0 | – |
| 3.0 | 108 | 106 | 14.2 | 14.4 | 1.8 |
| 5.2 | 64 | 57 | 24.2 | 15.8 | 5.4 |
| 7.0 | 75 | 65 | 20.7 | 17.8 | 6.2 |
| 11 | 95 | 91 | 16.4 | 15.4 | 8.2 |
| 15 | 127 | 127 | 12.4 | 15.6 | 7.7 |
| 20 | 110 | 106 | 14.4 | 15.2 | 12.0 |
| 25 | 126 | 121 | 12.7 | 11.3 | 13.3 |

$^a$ Crystallite sizes calculated as $d = 6 \cdot ((X_{TiO_2} \cdot \rho_{TiO_2} + X_{V_2O_5} \cdot \rho_{V_2O_5}) \cdot S_{BET})^{-1}$ with $\rho_{V_2O_5} = 3350 \, kg \, m^{-3}$ and $\rho_{TiO_2} = 3900 \, kg \, m^{-3}$ assuming spherical particle shape [21]

$^b$ Crystallite sizes calculated by Scherrer's equation as $\Phi = K \cdot \lambda \cdot (B_d \cdot \cos\theta)^{-1}$ with $\lambda_{CuK\alpha} = 1.54056$ nm, the peak form factor $K = 0.9$, the peak width at half hight $B_d$, and angle ($2\theta = 25.3°$) of the peak corresponding to the (101) reflections

$^c$ Surface density of vanadium atoms calculated as $n_s = m_{V_2O_5} \cdot 2 \cdot N_A (m_{total} \cdot M_{V_2O_5} \cdot S_{BET} \cdot 10^{18})^{-1}$ [22]

incorporating rutile has previously [19, 20] been observed when vanadia-anatase materials were heated to temperatures higher than 500 °C. Also vanadium/titanate composite nanorods have been reported [8] to form under hydrothermal conditions. Further studies towards identifying the minor crystalline phase and its possible effect on catalytic activity in, e.g. SCR of NO$_X$, are in progress.

The size of the formed oxide crystallites was calculated by Scherrer's equation (using the peak angle $2\theta = 25.3°$) to be in the range of 11–18 nm (see Table 1) with no obvious correlation to the vanadia content. Sequential measurements of the samples during calcination further revealed that anatase crystallization was initiated around 300 °C followed by crystal growth until the particles reached the equilibrium size after 1–2 h.

TEM images of the materials confirmed the high degree of crystallinity of the anatase support and average particle sizes of about 10 nm, as exemplified in Fig. 2 for pure anatase, 7 and 25 wt.% samples. Additionally, the (101) lattice plan of anatase with a distance of 0.35 nm between the atomic layers was clearly identified [23]. In the vanadia-containing samples, an amorphous layer surrounding the nano-sized anatase crystallites with no distinctive structure and a thickness around ca. 0.5 nm could further be attributed to vanadia, while indication of V$_2$O$_5$ crystallite formation only became apparent in the 25 wt.% sample (Fig. 2c).

Crystallite sizes comparable to those measured by TEM were also deduced from the measured S$_{BET}$ areas of the materials assuming a spherical shape of particles (see Table 1), thus indicating no significant intra particulate crystal porosity. However, in contrast to the particle size dependency established from the XRPD measurements, a clear tendency towards decreasing crystallite size with increasing vanadia loading was observed from the specific surface area calculations, suggesting significant differences in the texture of the mixed materials depending on the oxide composition.

The pore size distributions of the materials were calculated from nitrogen physisorption isotherms to be relatively well defined with pore diameters in the range of 3–5 nm, increasing with the vanadium loading. Representative size distribution plots are shown for the 3 and 20 wt.% materials in Fig. 3.

For the material with 20 wt.% vanadia loading a shoulder appeared, however, at 8–9 nm suggesting a slightly bimodal pore structure for the catalysts with high loadings of vanadium. For comparison, the pore size distribution of a conventional TiO$_2$ sample exposed to similar thermal treatment is also shown in Fig. 3. An obvious shift in pore size distribution towards smaller pores is obtained by the new seed-assisted sol–gel method. Thus, the new
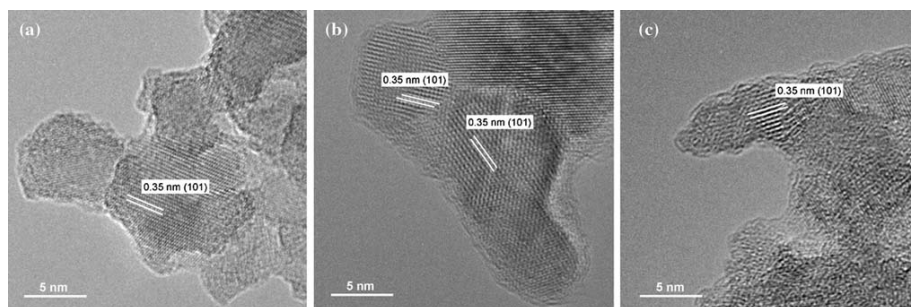


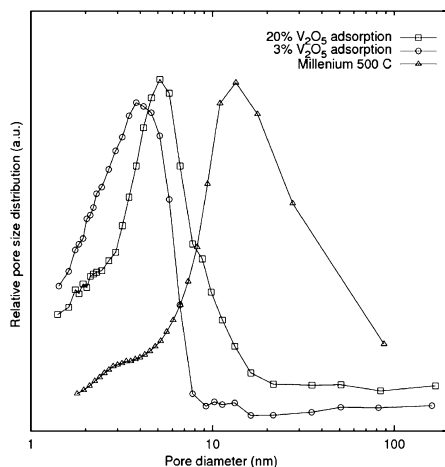**Fig. 2** TEM micrographs of prepared (**a**) anatase, (**b**) 7 wt.% VO$_X$/anatase and (**c**) 25 wt.% VO$_X$/anatase materials

**Fig. 3** Pore size distributions obtained from nitrogen sorption data for 3 and 20 wt.% VO$_X$/anatase materials and a commercial pure anatase support (TIONA-G5, Millennium Co.), respectively

materials have a pore structure which can be characterized as being between micro- and meso-pores. Microporosity as such is not desirable for catalyst materials, due to possible diffusion limitations to the less accessible surface. However, calculations of the external surface areas by the *t*-plot method yielded values virtually identical to those derived from the BET equation (see Table 1). This confirmed that essentially all surface area originated from none microporous structures, yielding readily accesible surface vanadia species for gas-phase molecules. The observed increase in pore sizes combined with the increased areas is not observed for vanadia/TiO$_2$ materials synthesized by conventional impregnation methods. Here a decrease is usually observed along with the filling of the pore system [24]. The phenomenon observed here can be explained by the induced added distance between the anatase particles by the vanadium salt during the co-precipitation step. After calcination, the precursor transforms to mobile oxo-vanadium species, which disperse over the high-surface area of TiO$_2$, leaving the framework with increased porosity, wider pores and added surface roughness.

## Conclusions

Nano-particle VO$_X$/TiO$_2$ materials have for the first time been prepared by co-precipitation of vanadia and titania by a seed-assisted sol–gel, co-precipitation method. The calcined material consisted of crystalline anatase particles covered with amorphous vanadia with a very uniform size distribution of around 12 nm. The small particle size of the anatase support (due to the corresponding high-surface area) allowed high loading of up to 15 wt.% vanadia without exceeding monolayer coverage of V$_2$O$_5$ in contrast to typical industrial catalysts which only can accommodate 3–5 wt.%.

Recently, comprehensive studies of the activity of these nano-VO$_X$/TiO$_2$ catalysts for both oxidation reactions and SCR of NO$_X$ in flue-gases by NH$_3$ have been initiated. Preliminary results here indicate a superior activity compared to traditional catalysts, thus suggesting that the nano-materials might prove useful where small catalyst bed volumes or SCR catalysts with prolonged life on steam are desired. This is especially the case for biomass-fired power plants (or co-fired with fossil fuels), where the aggressive K-containing flue-gas rapidly decreases the activty of the traditional deNO$_X$ catalysts [25–28].

## References

1. Weckhuysen BM, Van Der Voort P, Catana G (eds) (2000) Spetroscopy of transition metal ions on surfaces. Leuven University Press, Leuven
2. Gao X, Wachs IE (2002) Top Catal 18:243. doi:10.1023/A:1013842722877
3. Weckhuysen BM, Keller DE (2003) Catal Today 78:25. doi:10.1016/S0920-5861(02)00323-1
4. Parvulescu VI, Grange P, Delmon B (1998) Catal Today 46:233. doi:10.1016/S0920-5861(98)00399-X
5. Busca G, Lietti L, Ramis G, Berti F (1998) Appl Catal 18:1. doi:10.1016/S0926-3373(98)00040-X
6. Astruc D, Lu F, Aranzaes JR (2005) Angew Chem Int Ed 44:7852. doi:10.1002/anie.200500766
7. Wang X, Landau MV, Rotter H, Vradman L, Wolfson A, Erenburg A (2004) J Catal 222:565. doi:10.1016/j.jcat.2003.12.003
8. Yu L, Zhang X (2004) Mater Chem Phys 87:168. doi:10.1016/j.matchemphys.2004.05.022
9. Mohamed MM, Bayoumy WA, Khairy M, Mousa MA (2006) Microporous Mesoporous Mater 97:66. doi:10.1016/j.micromeso.2006.07.028
10. Liu G, Wang K, Zhou Z (2006) Mater Sci Forum 510–511:86
11. Stark WJ, Wegner K, Pratsinis SE, Baiker A (2001) J Catal 197:182. doi:10.1006/jcat.2000.3073
12. Schimmoeller B, Schulz H, Pratsinis SE, Bareiss A, Reitzmann A, Kraushaar-Czarnetzki B (2006) J Catal 243:82. doi:10.1016/j.jcat.2006.07.007
13. Hari-Bala, Zhao J, Jiang Y, Ding X, Tian Y, Yu K, Wang Z (2005) Mater Lett 59:1937

327

14. Hari-Bala, Guo Y, Zhao X, Zhao J, Fu W, Ding X, Jiang Y, Yu K, Lv X, Wang Z (2006) Mater Lett 60:494 doi:10.1016/j.matlet.2005.09.030
15. Lippens BC, de Boer JH (1965) J Catal 4:319. doi:10.1016/0021-9517(65)90307-6
16. Rouquerol F, Rouquerol J, Sing K (1999) Adsorption by powders and porous solids—principles, methodology and applications. Academic Press, London
17. Groen JC, Pérez-Ramírez J (2004) Appl Catal A 268:121. doi:10.1016/j.apcata.2004.03.031
18. Mellqvist J, Rosén A (1996) J Quant Spectrosc Radiat Transfer 56:87
19. Hausinger G, Schmelz H, Knözinger H (1988) Appl Catal 39:267. doi:10.1016/S0166-9834(00)80954-9
20. Grzybowska-Świerkosz B (1997) Appl Catal A 157:263. doi:10.1016/S0926-860X(97)00015-X
21. Lide DR (ed) (2007) CRC handbook of chemistry and physics, 87th edn. Taylor and Francis, Boca Raton, FL
22. Kamata H, Takahashi K, Odenbrand CUI (1999) J Mol Catal A 139:189. doi:10.1016/S1381-1169(98)00177-0
23. Dmitri A, Kiwi-Minsker L, Zaikovskii V, Renken A (2000) J Catal 193:145. doi:10.1006/jcat.2000.2872
24. Yates M, Martín JA, Martín-Luengo JA, Suarez S, Blanco J (2005) Catal Today 107–108:120. doi:10.1016/j.cattod.2005.07.015
25. Kustov AL, Kustova MY, Fehrmann R, Simonsen P (2005) Appl Catal B 58:97. doi:10.1016/j.apcatb.2004.11.016
26. Zheng Y, Jensen AD, Johnsson JE (2005) Appl Catal B 60:253. doi:10.1016/j.apcatb.2005.03.010
27. Due-Hansen J, Kustov AL, Rasmussen SB, Fehrmann R, Christensen CH (2006) Appl Catal B 66:161. doi:10.1016/j.apcatb.2006.03.006
28. Due-Hansen J, Boghosian S, Kustov AL, Fristrup P, Tsilomelekis G, Ståhl K et al (2007) J Catal 251:459. doi:10.1016/j.jcat.2007.07.016

**High performance vanadia-anatase nanoparticle catalysts for the Selective Catalytic Reduction of NO by ammonia**

Kristensen, S.B.; Kunov-Kruse, A.J.; Riisager, A.; Rasmussen, S.B.; Fehrmann, R.

*J. Catal* **2011**, *284*, 60-67

# Article

# 2

# High performance vanadia–anatase nanoparticle catalysts for the Selective Catalytic Reduction of NO by ammonia

Steffen B. Kristensen [a], Andreas J. Kunov-Kruse [a], Anders Riisager [a], Søren B. Rasmussen [b], Rasmus Fehrmann [a,*]

[a] Department of Chemistry and Centre for Catalysis and Sustainable Chemistry, Building 207, Technical University of Denmark, DK-2800 Kgs. Lyngby, Denmark
[b] Instituto de Catálisis y Petroleoquimica, Consejo Superior de Investigaciones Científicas, Marie Curie 2, Campus de UAM, 28020 Madrid, Spain

ABSTRACT

Highly active nanoparticle SCR deNO$_X$ catalysts composed of amorphous vanadia on crystalline anatase have been prepared by a sol–gel, co-precipitation method using decomposable crystallization seeds. The catalysts were characterized by means of XRPD, TEM/SEM, FT-IR, nitrogen physisorption and NH$_3$-TPD. Due to the high-surface area anatase particles, loading of 20 wt% vanadia could be obtained without exceeding monolayer coverage of V$_2$O$_5$. This resulted in unprecedented high deNO$_X$ SCR activity corresponding to a factor of two compared to an industrial reference and to other V$_2$O$_5$/TiO$_2$ catalysts reported in the literature in the examined temperature range of 200–400 °C. The catalysts showed very high resistivity towards potassium poisoning maintaining a 15–30 times higher activity than the equally poisoned industrial reference catalyst, upon impregnation by 280 µmole potassium/g of catalyst.

© 2011 Elsevier Inc. All rights reserved.

## 1. Introduction

The catalytic cleaning of flue gases for nitrogen oxides (NO$_X$) in stationary industrial sources, like power plants, is most often done using V$_2$O$_5$/TiO$_2$-based SCR (Selective Catalytic Reduction) catalysts (promoted by WO$_3$ or MoO$_3$) which reduce NO$_X$ to nitrogen and water by injected ammonia. The efficiency of state-of-the-art catalysts is high when applied to flue gases from fossil fuels like oil and coal. However, the use of biomass (straw, wood) alone or as co-fuel is of increasing importance because this type of fuel is considered CO$_2$ neutral. Unfortunately, the flue gas becomes very poisonous towards the V$_2$O$_5$/TiO$_2$ catalyst due to increased content of alkaline potassium salts (i.e., KCl, K$_2$SO$_4$ and K$_2$O) originating from the biomass combustion. These salts, as particles or aerosols, are considered to eliminate Brønsted acid sites on vanadium (V–OH) by substituting the protons of OH-groups with potassium ions forming V–O–K groups [1–4]. Since the Brønsted acid sites are essential for the activation of ammonia [5], the catalyst deactivates rapidly in biomass flue gases, demanding replacement and/or cleaning of the catalyst within intervals of less than 2000 h on stream [6]. This procedure requires inconvenient and expensive shut down of the power plant.

In the present work, we have focused on improving the activity of the traditional V$_2$O$_5$/TiO$_2$ SCR catalyst as a way to prolong the time on stream where the catalyst retains sufficiently high activity.

The activity of the industrial V$_2$O$_5$/TiO$_2$-based SCR catalyst is limited by the surface area and acidity of the anatase carrier. Since only up to one monolayer of the vanadium oxide species, i.e., a theoretical maximum of 7–8 Vanadium atoms/nm$^2$ [7,8], shows high activity and selectivity, commercial catalysts only accommodate a vanadia loading of 3–5 wt% due to the low surface area of the support. Exceeding the monolayer capacity of the carrier with a high vanadia loading leads to formation of crystalline V$_2$O$_5$, which exhibits decreased deNO$_X$ activity and increased ability to oxidize NH$_3$ and possibly also SO$_2$ in the flue gas [9]. One approach to improve the efficiency of catalytic materials is to prepare them as very small nanosized particles. Smaller particles have an increased surface area compared with the same mass of larger particles, which allows them to accommodate more of the catalytic active monolayer. Hence, it is very likely that a catalyst based on tiny nanocrystals of TiO$_2$ with a monolayer of amorphous V$_2$O$_5$ will be able to reduce NO$_X$ with increased efficiency and lifetime in biomass fired applications, thus complying with demand for sufficient activity during prolonged operation.

Another parameter that limits activity in traditional V$_2$O$_5$/TiO$_2$ SCR catalysts and further makes them very sensitive to alkali poisoning is the relatively poor acidic properties of anatase. Pure

anatase has only moderate acidity ($H_0$ = +1.5 on the Hammett acid scale [10]), whereas sulphated anatase prepared from sulphated amorphous TiO$_2$ exhibits super acidity ($H_0 > -11.93$ [10]). Introduction of additional strong acidic sites through sulphation promotes the overall catalyst activity by increasing the amount of adsorbed, activated ammonia. Even more importantly, the acidic sites can host the alkali ions during operation avoiding elimination of the active vanadia sites. Furthermore, sulphation of the carrier prior to calcination can stabilize small nanocrystals when formed and increase the specific surface area significantly [11].

The use of promoters such as Ce to increase the acidity of the catalyst is also a solution [12]. Another solution to the problem could be the use of alternative transition metal-based catalysts and support materials for SCR deNO$_X$ catalysis, which are less sensitive to the presence of alkali salts in the flue gas [13–15]. This approach is currently under investigation.

In this work, vanadia–anatase catalysts with a narrow nanosize distribution and high-surface area were synthesized by a modified novel sol–gel procedure [16–18]. Involving concomitant hydrolysis of titanium(IV) and vanadium(V) alkoxides in the presence of ammonium salt crystallization seeds followed by sulphation with sulphuric acid [19]. The prepared materials were characterized by X-ray Powder Diffraction (XRPD), Transmission and Scanning Electron Microscopy (TEM and SEM), Fourier-Transform Infrared Spectroscopy (FT-IR), Temperature Programmed Desorption of Ammonia (TPD) and nitrogen sorption methods (BET). The resulting V$_2$O$_5$/TiO$_2$ catalysts with vanadia loading in the range 5–25 wt% were tested for SCR deNO$_X$ activity and compared to an industrial state-of-the-art reference catalyst. Analogous vanadia/TiO$_2$ materials have also been previously prepared by flame synthesis [20,21], hydrothermal methods [22,23] and mechanical blending [24] and the former evaluated for SCR deNO$_X$. Notably, none of these catalysts have shown the same promising properties as the catalysts reported in this work.

## 2. Experimental

### 2.1. Catalyst preparation

Nanoparticular vanadia/anatase catalysts were prepared by hydrolysis of an acetous ethanol solution, containing titanium(IV) isopropoxide (97%, Lancaster) and vanadium(V) oxytriethoxide (95%, Aldrich), with an aqueous solution of ammonium nitrate (99.0%, Aldrich) forming solid seed crystals. In a typical preparation the Ti(OC$_3$H$_7$)$_4$, VO(OC$_2$H$_5$)$_3$ and acetic acid mixture was first diluted in absolute ethanol and then cooled to 0 °C in an ice bath. The aqueous ammonium nitrate solution was then added dropwise to the ethanolic solution under magnetic stirring to form a sol–gel. The molar ratio of the reactants was adjusted to Ti/V/acetic acid/water/ethanol/ammonium salt = 1:$x$:2:15:30:2, where $x$ was varied according to the desired amount of vanadium required to obtain catalysts with vanadia loading between 5 and 25 wt%. Subsequently, the sol–gel was aged at room temperature for 48 h under stirring. In some cases, sulphuric acid was added to sulphate the titania and simultaneously remove acetic acid by esterification. Next, excess ethanol, water, acetic acid and liberated isopropanol were removed under reduced pressure (12 mbar, 70 °C). Finally, the remaining powder was calcined at 380 °C in an air stream (300 mL min$^{-1}$) to decompose the ammonium template and convert amorphous titania into crystalline anatase [19]. The calcination temperature was chosen to match normal maximum operating temperature of the SCR unit in a power plant. Potassium doping of catalysts was done by incipient wetness impregnation using an aqueous solution of KNO$_3$ (99%, Riedel-de Haën), followed

by drying (100 °C) and dehydration at 250 °C to ensure formation of K$_2$O. All poisoned samples were impregnated with 280 μmole of potassium/g catalyst.

### 2.2. Catalyst characterization

BET surface areas of samples were determined by physical adsorption of nitrogen using a Micromeritics ASAP 2020 analyzer. XRPD diffractograms were obtained by collecting data for 60 min with a Huber Guinier G670 camera at 25 °C using Cu Kα radiation. FT-IR spectra were recorded using wafers comprising 1 mg of sample mixed with 100 mg KBr using a Perkin-Elmer 1710 Infrared Fourier-Transform Spectrophotometer. The spectra were measured under ambient conditions using 30 scans. TEM micrographs were obtained using a Titan Analytical 300 kV transmission electron microscope, and SEM images were recorded using an Inspect 'S' scanning electron microscope with a tungsten filament electron source. The ammonia temperature programmed desorption was performed on a Micromeritics Autochem II Chemisorption analyzer with TCD detector. The samples were outgassed at 100 °C for 1 h in helium (99.999%, AGA), saturated with ammonia in a 50 mL min$^{-1}$ flow of 1% NH$_3$ in He (AGA) and flushed with helium for 1 h, and finally, the TPD experiment was performed with a heating rate of 10 °C min$^{-1}$. Influence of desorbed SO$_2$ from the sulphated samples on the TPD profiles was eliminated by carrying out a NH$_3$-TPD experiment using He instead of NH$_3$.

### 2.3. Catalytic activity tests

Prior to the activity measurements, powdered samples were made into pellets (pressurized by 2.5 kbar), which were crushed and sieved to obtain particle fractions of 0.150–0.300 mm. SCR activity measurements were performed in a fixed-bed reactor using 8 mg catalyst diluted in 142 mg of SiO$_2$ (Quartz, Merck) with the same particle size. The mixture was loaded between the two layers of quartz wool in a quartz tube with an inner diameter of 5 mm. These conditions ensured isothermal plug-flow conditions, as previously described [25]. The reactant gas composition used in all the activity tests was 1000 ppm NO, 1100 ppm NH$_3$, 3% O$_2$ and balance He obtained from mixing of 1 vol% NO in He (±0.05% abs.), 1 vol% NH$_3$ in He (±0.05% abs.), O$_2$ (⩾99.95%) and helium (99.999%) (all from AGA) with a total flow rate of 700 mL min$^{-1}$. These conditions resulted in a gas hourly space velocity of 1,240,000 h$^{-1}$ calculated from the volume of the active catalyst particles. The SCR reaction is known to be first order with respect to NO on vanadia catalysts under stoichiometric NH$_3$ conditions [26,27]. By assuming plug-flow conditions in the reactor, the performance can be expressed as the apparent first-order rate constant: $k = -F_0 \cdot [NO]_0^{-1} \cdot m_{cat}^{-1} \cdot \ln(1 - X)$, were $F_0$ is the molar NO feed rate, $[NO]_0$ the molar NO concentration at the inlet, $X$ the NO conversion fraction and $m_{cat}$ the mass of the catalyst [28]. The use of first-order rate constants as a measure of catalytic activity allows a direct comparison with other studies using different experimental conditions, e.g., catalyst masses and gas flows. NO and ammonia concentrations were measured at steady-state gas outlet concentrations with NO conversions ⩽75% by online UV–VIS spectrophotometry using a Perkin Elmer Lambda 11 spectrometer (10 cm gas cell). SO$_2$ oxidation tests were performed with 80 mg catalyst exposed to 2000 ppm SO$_2$, 4.5% O$_2$ and He as balance ensuring a flow rate of 400 mL min$^{-1}$. Exposure time were 7200 min at 340–420 °C. Oxidized SO$_2$ was collected in a absorption column heated to 80 °C. Formed SO$_3$ were collected by a 20 wt% aqueous in isopropanol solution, and the amount of SO$_3$ was determined by titration with Ba(ClO$_4$)$_2$ using Thorin indicator.

127

## 3. Results and discussion

### 3.1. X-Ray powder diffraction

XRPD analysis of previously prepared, nanoparticular vanadia–titania catalysts using $NH_4Cl$ as a crystallization seed [18] revealed only crystalline anatase as support phase with no peaks originating from residual crystalline $NH_4Cl$ or $V_2O_5$. However, the samples did show a new phase suggesting either a crystalline vanadium-titania phase or a vanadium chloride phase. Catalysts in this work prepared with $NH_4NO_3$ as crystallization seed even with amounts of vanadia surpassing the monolayer limit of 8 V atoms/nm$^2$ showed likewise no crystalline $V_2O_5$. This indicates a high dispersion of an amorphous vanadia phase as typically found for oxide-supported vanadia catalysts [7,8]. However, the samples did contain a new phase originating from either a crystalline vanadia–titania phase or a more likely brookelite phase. This was observed only for unsulphated catalysts confirming that the $H_2SO_4$ acts as a crystal structure directing agent, which has been concluded before [29].

However, the vanadia–titania catalysts prepared in this work using $NH_4NO_3$ as the crystallization seed did not show the unidentified phase (see Fig. 1). This supports the vanadia–chloride phase hypothesis proposed in previous work [18] when using $NH_4Cl$ as seed crystal. Hence, vanadium appeared to be dispersed on the surface of small anatase crystallites as amorphous vanadia–chloride or as pure vanadia depending on the selected crystallization seed. In accordance with this, no shifts of XRD reflections were observed, indicating no incorporation of vanadia into the anatase framework.

The size of the oxide crystallites formed was calculated by Scherrer's equation (using the peak at angle $2\theta = 25.3°$) to be in the range 7–15 nm, with no direct correlation with the vanadia content (see Table 2). But sulphation of catalysts as a last step in the preparation procedure before drying decreased the crystallite size, as shown in Table 2. Sequential measurements of the samples during calcination revealed that anatase crystallization was initiated around 300 °C followed by crystal growth until the particles reached the reported equilibrium size after 4 h. BET measurements (Table 2) of the catalysts revealed a correlation between increased vanadia loading and increased surface area. This could be explained by formation of amorphous $V_2O_5$ "islands" on the surface, which decreases the surface smoothness but increases the surface area. BET surface areas were also found to increase approx. 20 m$^2$/g



**Fig. 1.** Selected powder diffractograms of prepared vanadia–titania catalysts, with numbers indicating wt% $V_2O_5$ and $SO_4^{2-}$ sulphated catalysts. All reflections indicate anatase crystal structure except reflections indicated with ∗, which originate from the brookelite crystal form.

upon sulphation, compared to the analogous non-sulphated catalysts.

### 3.2. TEM and SEM

TEM images of the 15 wt% vanadia–titania catalysts synthesized with sulphuric acid confirmed the high degree of crystallinity of the anatase support (Fig. 2). The crystal sizes were estimated by size measurement of 70 crystals, and the results agreed well with the XRPD results. The sample also exhibited a very narrow crystal size distribution ranging from 4 to 9 nm with a mean size of 6 nm. No evidence of crystalline $V_2O_5$ was found despite the fact that crystallization is well known to occur in heavily loaded catalysts [30]. This indicates that the nanoparticle-based catalysts can accommodate much more vanadium than conventional catalysts without forming crystalline vanadia.

A single crystal from the sample was investigated by Fast Fourier-Transformation (FFT) to determine the crystal planes and thereby the crystal type. The FFT showed that the interplanar spacing of the (101) and (1̄01) planes were 3.5 Å and that the intersecting angle of the planes was 124°. The (004) interplanar spacing was measured to be 2.4 Å, and the angle between plane (101) and (104) was 27°. These results were identical to previous results obtained by XRPD and TEM on anatase in the literature [31,32]. SEM investigations confirmed nanocrystal agglomerates, but these particles showed a high degree of porosity, hence the maintained high-surface area.

### 3.3. Fourier-Transform Infrared Spectroscopy

The V═O stretch in crystalline $V_2O_5$ gives rise to a sharp and intense band at 1020 cm$^{-1}$ [7,8]. When $V_2O_5$ is bound to anatase, the V═O band is weakened and the IR signal shifts to a broad band at 980 cm$^{-1}$ [7,8] and is thus easily distinguished from the crystalline $V_2O_5$ phase. The recorded IR spectra of selected catalysts (Fig. 3) revealed a shoulder or a broad band at around 970 cm$^{-1}$ due to the V═O stretch, while no peak at 1020 cm$^{-1}$ was found in any of the spectra. The shift of the band, i.e., weakening of the V═O band, indicated a stronger interaction between $VO_x$ species and the anatase [7,8].

Broadening of the band around 970 cm$^{-1}$ was observed at loadings of 25 wt.% $V_2O_5$. Though the amorphous and strongly bonded $V_2O_5$ phase was still dominant, the broadening towards higher wave numbers indicated other species with a slightly increased V═O band strength originating from amorphous $V_2O_5$ phases with weaker or no bonding to the anatase surface. Thus, even far above the monolayer capacity of 8 vanadium atoms/nm$^2$, no presence of crystalline vanadia was indicated by TEM, XRPD or FT-IR. This further suggests that the new concomitant seed-assisted hydrolysis of titanium(IV)isopropoxide and vanadium(V)oxoethoxide results in a much more dispersed vanadia phase than is normally observed with more traditional impregnation methods. Several models for the formation of acidic sites due to sulphate species have been proposed [33,34], and it is well known that sulphating of anatase induces both Brønsted and Lewis sites of medium to strong acid strength [10]. The FT-IR spectra of catalysts with $H_2SO_4$ added before drying and calcination showed several new peaks at 1215, 1135 and 1043 cm$^{-1}$. These are all characteristic vibrations from monomeric sulphate species bound bidentately to anatase [34–37]. A sharp band at 1380 cm$^{-1}$ associated with anhydrous sulphates is normally reported in the literature for sulphated $TiO_2$ [34,35]. In the present samples, this band was absent most probably due to hydration of the species, which is known to occur at lower temperatures and under humid conditions [34]. Furthermore, the weak peak at 1405 cm$^{-1}$ could originate from small amounts of pyrosulphate dimers [38]. Though, it was more likely to originate
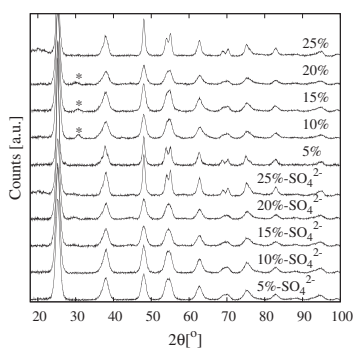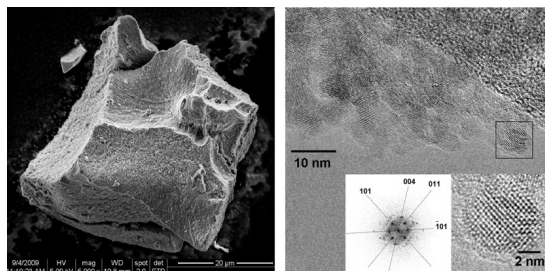
**Fig. 2.** TEM micrograph of 15 wt% $V_2O_5$/TiO$_2$ single crystal, zoom (framed area) and FFT of this area (right). SEM micrograph of a particle from the same sample (left).
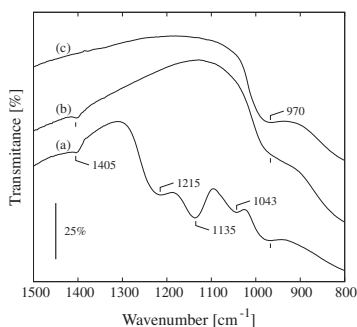


**Fig. 3.** Transmission FT-IR spectra of 1 mg catalyst in 100 mg KBr at ambient conditions. (a) 15 wt% $V_2O_5/SO_4^{2-}$–TiO$_2$, (b) 15 wt% $V_2O_5$/TiO$_2$, (c) 25 wt% $V_2O_5$/TiO$_2$.



**Fig. 4.** NH$_3$-TPD profiles of catalysts. Baseline measured without saturation with NH$_3$ of a 15 wt% $V_2O_5/SO_4^{2-}$–TiO$_2$ catalyst, TV05-25: Sulphated 5–25 wt%$V_2O_5$/TiO$_2$ catalysts, TV05-25 u: Unsulphated 5–25 wt% a $V_2O_5$/TiO$_2$ catalysts.

from traces of ammonium ions [29] since it was found in both sulphated and unsulphated samples. For metal oxide-supported sulphates, it is well known that Brønsted acidity is more dominant at lower temperatures and humid conditions whereas Lewis acidity is more dominant at higher temperatures and dry conditions [10]. Due to this fact, no further attempts have been made currently to characterize the type of acidic surface sites, because all spectra were recorded under ambient conditions. However, a more thorough spectroscopic investigation of the catalytic surface sites will be presented in future work.

### 3.4. Temperature programmed desorption

NH$_3$-TPD profiles of the catalysts, the calculated corresponding total adsorbed ammonia and the specific acidities are illustrated in Fig. 4 and Table 1, respectively. The specific acidity was, as expected for the unsulphated catalysts, very similar to the industrial reference catalyst, although the strength of the acidic sites in the reference catalyst seemed to be slightly weaker. The total amount of acidic sites in all the nanoparticle catalysts was higher due to the higher surface areas and $V_2O_5$ content.

By sulphation of the carrier, a significant increase in the amount of acidic sites of varying strength was observed corresponding to a total acidity of up to three times that of the unsulphated samples. A background was also performed to exclude decomposition products originating from adsorbed sulphate. A peak at around 380 °C

**Table 1**
Ammonia TPD of the catalysts.

| $V_2O_5$ (wt%) | Desorbed ammonia[a] (cm$^3$/g) | Specific acidity[a] (NH$_3$/nm$^2$) |
|---|---|---|
| 5[b] | 38 | 7.3 |
| 10[b] | 48 | 8.4 |
| 15[b] | 55 | 8.9 |
| 20[b] | 48 | 6.3 |
| 25[b] | 24 | 4.1 |
| 5[c] | 10 | 3.7 |
| 10[c] | 18 | 3.5 |
| 15[c] | 24 | 4.9 |
| 20[c] | 30 | 4.7 |
| 25[c] | 15 | 4.5 |
| Ref.[d] | 12 | 4.5 |

[a] The acidity was calculated only on the basis of acidic sites with intermediate strength (<500 °C) since higher and super acidic sites are not likely to take part in the SCR-reaction.
[b] Sulphated 5–25 wt% $V_2O_5$/TiO$_2$.
[c] Unsulphated 5–25 wt% $V_2O_5$/TiO$_2$.
[d] Industrial reference catalyst with 3 wt% $V_2O_5$-7 wt% WO$_3$ on TiO$_2$.

in the TPD profile indicated that the sulphation of the carrier induced sites with relatively high acid strength. These stronger sites are expected to be crucial to the SCR activity of the catalysts, as weaker acidic sites will be unable to adsorb ammonia at the typical operating temperatures of around 350–400 °C. A small part of the

acidic sites generated on both sulphated an unsulphated catalysts seemed to be very strong with peak values as high as 500, 670 and 700 °C. These sites could be strongly acidic or even super acidic undercoordinated titanium atoms on the carrier surface, created by the strong inducing effect of the sulphate species, as suggested by both experimental [32,33,39] and quantum mechanics studies [40,41] of similar sulphated metal oxides. A strong Lewis acid is characterized by a strong polarizing power. This polarization of the ammonia molecule results in a strengthening of the N—H band. This is directly observed with FT-IR as an upward shift of the symmetric N—H bending wave number [42]. A crucial step for the SCR mechanism is the activation of ammonia, which can be either a complete or a partial transfer of hydrogen from ammonia to a redox centre [5,9,43–46]. Accordingly, it is considered doubtful that the ammonia adsorbed on the very acidic sites associated with the peaks 500, 670 and 700 °C in the TPD profile plays any significant role in the SCR reaction, as the activation of this ammonia would require breakage of a significantly stronger N—H bond compared to the majority of the ammonia species associated with desorption peaks around the catalyst's working temperature (350–400 °C). Therefore, these peaks are excluded in the calculations in Table 1. However, the strong acidic sites may still be able to host alkali compounds and thereby preserve activity in case of alkali poisoning.

Table 1 shows that the amount of desorbed ammonia increases with increasing $V_2O_5$ content until an optimum is reached at 15–20 wt%. The specific acidity, by contrast, follows no clear trend other than that sulphation increases the acidity. Indicating that sulphation increases the acidity whereas the $V_2O_5$ content has no direct influence on specific acidity, but total acidity increases due to the increase in surface area.

### 3.5. Catalytic activity measurements

Catalytic activity was measured at temperatures from 200 to 450 °C to find activity maxima. The prepared catalysts exhibited remarkable SCR activities, as illustrated in the plot of the measured rate constants $k$ vs. temperature in Fig. 5 (catalysts synthesized without added sulphuric acid).

The optimum vanadium loading was observed at 20 wt% vanadia by comparing the activity maxima where a rate constant almost twice as high as the commercial reference catalyst was observed.

It should be noted that the commercial reference catalyst has been calcined at a somewhat higher temperature, i.e., around 450 °C, than the catalysts studied here. The increased sintering expected at increased temperature leads to agglomeration of the vanadium oxide species resulting in somewhat increased deNOx and SO2 oxidation activity as observed previously for industrial catalysts [47]. However, we find it more useful to compare our results with this industrial catalyst employed at 380 °C, rather than a less active conventional $V_2O_5/TiO_2$-based catalyst prepared by impregnation of a $TiO_2$ carrier with ammonium metavanadate and calcined at 380 °C.

From Fig. 5 it is also clear that the maximum activity temperature was gradually shifted from higher temperatures (around 480 °C) to lower temperatures (around 380 °C) with increasing vanadium loading. Since the maximum activity is reached where the competitive oxidation of $NH_3$ becomes more pronounced, the $NH_3$ oxidation must increase with increasing vanadium content. This trend is also observed for more traditionally prepared catalysts, due to formation of more active, but less selective, polymeric vanadia species [9,48]. The activity increases even further through adding sulphuric acid to the sol–gel before drying and calcinations (Fig. 6), allowing a rate constant above 2000 $cm^3\,g^{-1}\,s^{-1}$ to be obtained. Comparing the catalysts at ideal SCR temperatures (350–380°) reveals the vanadium loading of choice to be 20 wt%, which is remarkably high compared to usual SCR catalyst loadings.

Working with nanoparticles always raises the question of sintering. Long-term stability tests of a 15 wt% $V_2O_5/TiO_2$ catalyst at 380 °C (industrial operational temperature) is in progress, however, a previous test of such catalyst doped with a small and probably insignificant amount of Au (1 wt%), indicated thermal stability for 500 h. Hysteresis was observed after heating to 460 °C possible due to sintering and evaporation of $SO_4^{2-}$ acid sites, corresponding to an activity loss of 20% for the sulphated 20 wt% catalyst. This temperature is comparable with the calcination temperature for the industrial reference catalyst of 450 °C. Keeping the temperature below 420 °C only deactivated the catalyst 10%, and no deactivation was observed at 400 °C and temperatures below. A sulphated 15 wt% catalyst was calcined at 450 °C in air for 4 h in order to investigate possible reasons for the activity loss and hysteresis.



**Fig. 5.** Activity of unsulphated catalysts with varying $V_2O_5$ content: (■) 5 wt%, (□) 10 wt%, (○) 15 wt%, (●) 20 wt%, (▲) 25 wt%, (···) industrial reference 3 wt% $V_2O_5$ 7 wt% $WO_3$ on $TiO_2$ catalyst.



**Fig. 6.** Activity of sulfated catalysts with varying $V_2O_5$ content: (■) 5 wt%, (□) 10 wt%, (○) 15 wt%, (●) 20 wt%, (▲) 25 wt%, (···) industrial reference 3 wt% $V_2O_5$ 7 wt% $WO_3$ on $TiO_2$ catalyst.

**Table 2**
Characteristics of the prepared vanadia–anatase catalysts.

| $V_2O_5$ (wt%) | $k_{max}(T_{max})$ ($cm^3/g\,s$) (°C)) | $E_a$ (kJ/mol) | $S_{BET}$ ($m^2/g$) | $d_{particle}$[a] (nm) | $n_s$[b] ($V/nm^2$) |
|---|---|---|---|---|---|
| 5[c] | 948 (426) | 54 | 129 | 7.5 | 2.6 |
| 10[c] | 1711 (424) | 53 | 144 | 7.7 | 4.6 |
| 15[c] | 2097 (426) | 52 | 151 | 7.1 | 6.5 |
| 20[c] | 2091 (405) | 49 | 189 | 7.7 | 7.0 |
| 25[c] | 1422 (393) | 51 | 89 | 13.9 | 18.6 |
| 5[d] | 644 (450) | 44 | 67 | 15.6 | 4.9 |
| 10[d] | 1327 (451) | 53 | 126 | 8.1 | 5.3 |
| 15[d] | 1677 (424) | 44 | 121 | 8.8 | 8.2 |
| 20[d] | 1772 (423) | 46 | 156 | 8.0 | 8.2 |
| 25[d] | 1277 (373) | 50 | 82 | 14.9 | 20.2 |
| Ref.[e] | 993 (446) | 52 | 68 | 29.6 | 2.9 |

[a] Calculated by Scherrer's equation [52] (using the peak angle $2\theta = 25.3°$).
[b] Surface density of vanadium atoms calculated as $n_s = m_{V_2O_5} \cdot 2 \cdot N_A \cdot (m_{cat} \cdot M_{V_2O_5} \cdot S_{BET} \times 10^{18})^{-1}$.
[c] Synthesized using the $NH_4NO_3$ template followed by sulphation with sulphuric acid.
[d] Synthesized using the $NH_4NO_3$ template without sulphation.
[e] Industrial reference catalyst with 3 wt% $V_2O_5$-7 wt% $WO_3$ on $TiO_2$.

XRPD of this sample showed as for all the other catalyst samples only peaks from anatase and no indication of crystalline $V_2O_5$. However, the average anatase crystal size increased from 7.1 nm obtained for the very same 15 wt% catalyst calcined at 380 °C for 4 h (Table 2) to 15.6 nm pointing to agglomeration of the carrier particles as cause for the activity loss and hysteresis observed when the catalyst is calcined above 400 °C. Unsulphated catalysts suffered only slight deactivation upon heating, indicating that the thermal deactivation of sulphated catalysts are almost entirely due to evaporation of acid sites.

The advantage of the nanoparticle catalysts was even more pronounced when comparing resistance towards potassium poisoning, as clearly illustrated in Figs. 7 and 8. The six catalysts were all impregnated with 280 μmole potassium per gram of catalyst. All the non-sulphated catalysts maintained a relatively high activity at 380 °C, with the exception of the catalyst with 5 wt% loading that showed approximately the same deactivation as the reference catalyst. The most alkaline-resistant unsulphated catalyst was obtained with 20 wt% $V_2O_5$, which had an activity of approx. 600 $cm^3\,g^{-1}\,s^{-1}$. This corresponds to an activity 15 times higher



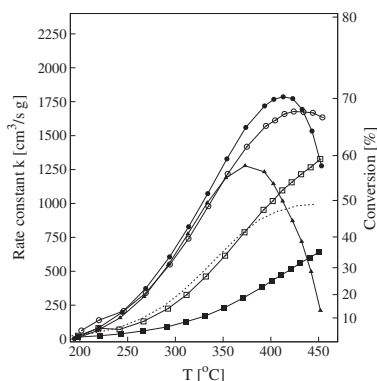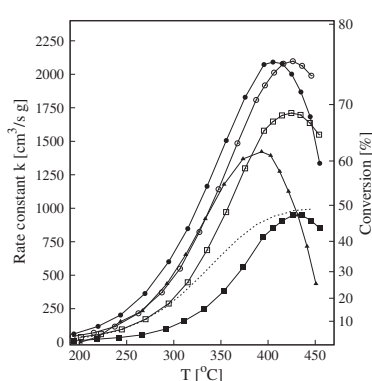**Fig. 8.** Activity of potassium deactivated (280 μmole K/g) unsulphated catalysts with varying $V_2O_5$ content: (■) 5 wt%, (□) 10 wt%, (○) 15 wt%, (●) 20 wt%, (▲) 25 wt%, (···) industrial reference 3 wt% $V_2O_5$ 7 wt% $WO_3$ on $TiO_2$ catalyst.

than the industrial reference catalyst at 380 °C. Upon sulphation, the resistance increased even more and the 20 wt% catalyst only deactivated by 40% resulting in an activity more than 30 times the potassium deactivated reference catalyst. All the catalysts revealed increased deactivation upon heating due to surface diffusion of potassium to the active sites above the $K_2O$ Tamman temperature [49]. Furthermore, decomposition of formed sulphate-potassium species leads to liberation of potassium oxide as previously reported with sulphated catalysts [13].

### 3.6. Selectivity and stability

To investigate the activity at more realistic conditions, additional activity measurements were performed with $H_2O$ and $SO_2$ in the flue gas, see Fig. 9. The first segment confirms the activity as previously illustrated at 380 °C in Fig. 6. In accordance with



**Fig. 7.** Activity of potassium deactivated (280 μmole K /g) sulphated catalysts with varying $V_2O_5$ content: (■) 5 wt%, (□) 10 wt%, (○) 15 wt%, (●) 20 wt%, (▲) 25 wt%, (···) industrial reference 3 wt% $V_2O_5$ 7 wt% $WO_3$ on $TiO_2$ catalyst.



**Fig. 9.** Activity measurements of 20 wt% $V_2O_5$ sulphated and an industrial reference 3 wt% $V_2O_5$ 7 wt% $WO_3$ on $TiO_2$ catalyst. Gas flow and composition 730 ml/min, dry: 1000 ppm NO, 1100 ppm $NH_3$, 3% $O_2$ and He balance, $H_2O$: additional 2.4% $H_2O$, $SO_2$: additional 2000 ppm $SO_2$ and $H_2O$, $SO_2$: the two combined.
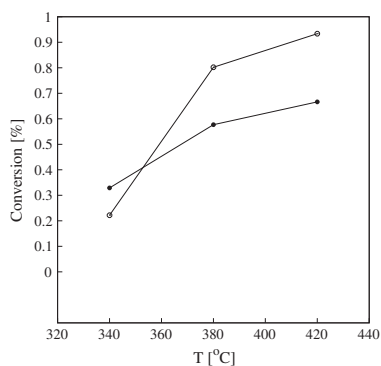
**Fig. 10.** SO$_2$ oxidation, (●) 20 wt% V$_2$O$_5$ sulphated, (○) the industrial reference 3 wt% V$_2$O$_5$ 7 wt% WO$_3$ on TiO$_2$ catalyst. Gas flow composition 2000 ppm SO$_2$, 4.5% O$_2$ and He as carrier.

Turco et. al [50], the activity decreased in the presence of water, see second segment, where 2.4% H$_2$O is added and the activity decreased 10–12%. Introducing 2000 ppm of SO$_2$ and removing water increased the activity of the 20 wt% catalyst to conversions just above the initial. Activity of the industrial reference also increases in activity resulting in conversions just below the initial. By adding water, the activity decreased again 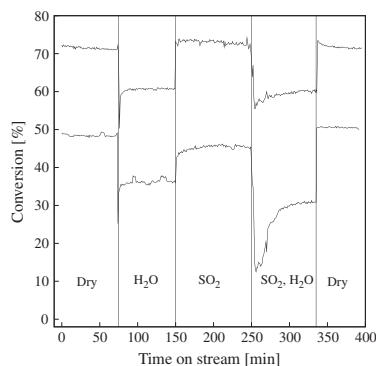by the same amount as before going from dry to wet gas, 10–12%. Last segment shows the initial activity again in dry flue gas demonstrating the high thermal and chemical stability of the 20 wt% V$_2$O$_5$ catalyst, displaying no activity loss due to H$_2$O or SO$_2$ treatment. SO$_3$ formation is a major concern due to fouling of the catalyst and heat exchangers downstream by NH$_4$HSO$_4$. Comparison of SO$_2$ oxidation between the industrial reference and the 20 wt% catalyst can be seen in Fig. 10. From this, it is clear that the 20 wt% V$_2$O$_5$ catalyst is exhibiting the same SO$_2$ oxidation properties as the industrial reference, despite the high V$_2$O$_5$ loading. Like wise selectivity measurements showed that the 15 wt% sulphated catalyst formed less N$_2$O in dry flue gas at 350–420 °C than the industrial reference catalyst, respectively, 13–62 and 33–146 ppm N$_2$O formed. But the formation vastly decreased in wet gas for both catalysts as expected from previous selectivity measurements in literature [51].

## 4. Conclusions

New types of highly active SCR deNO$_X$ catalysts based on nano-sized crystalline anatase has been synthesized. The synthesis method involved hydrolysis of titanium(IV) and vanadium(V) in ethanol solution with added acetic acid in the presence of a NH$_4$NO$_3$ crystallization template followed by sulphation with sulphuric acid. Different parameters in the synthesis protocol were investigated. XRPD and BET experiments revealed that NH$_4$NO$_3$ seeds gave smaller anatase crystals (6–8 nm) and larger surface areas (up to 189 m$^2$/g) than when using NH$_4$Cl in earlier studies [18]. Moreover, the use of NH$_4$NO$_3$ yielded samples of pure anatase without impurities from mixed phases (determined by XRPD and TEM). Sulphation with sulphuric acid increased the surface area, but more importantly it also increased the total acidity of the catalyst by a factor of approximately three and induced a significant increase in the strength of the acidic sites.

The optimal V$_2$O$_5$ content in the catalysts was found to be around 20 wt%, which is very close to one theoretical monolayer

formed on the carrier surface. The surface species characterized by the V=O stretch with FT-IR showed a larger shift towards lower wave numbers than reported elsewhere in the literature, indicating a stronger bond between the anatase support and the active vanadia phase. When the theoretical monolayer was exceeded, no sign of crystalline V$_2$O$_5$ was detected by XRD, FT-IR or TEM, although the formation of weaker bonding species was indicated by FT-IR. Activity of the 20 wt% V$_2$O$_5$/SO$_4^{2-}$−TiO$_2$ catalyst had a maximum around 420 °C with the rate constant $k$ = 2100 cm$^3$ s$^{-1}$ g$^{-1}$, which is more than twice the value for the industrial state-of-the-art catalyst used as reference. The catalysts showed decrease in deNOx activity after heating to 420 °C and above. It is well known that the addition of tungsten oxide increases the thermal stability of industrial catalysts. Optimization of the thermal stability of the catalysts prepared here by addition of tungsten oxide will be the subject of studies in the near future. The new catalysts also demonstrated a large increase in resistance towards potassium poisoning. Thus, the deactivation by potassium poisoning of the commercial catalyst was 96% compared to only 64% and 40% for the 20 wt% V$_2$O$_5$−TiO$_2$ and 20 wt% V$_2$O$_5$/SO$_4^{2-}$−TiO$_2$ catalysts respectively at 380 °C. This means that the new catalysts maintained a 15-30 times higher activity than the industrial reference catalyst under SCR conditions after poisoning. These features make them highly attractive as promising SCR catalysts in power plants fired with CO$_2$ neutral biomass fuels.

## References

[1] J. Chen, R. Yang, J. Catal. 25 (2006) 411.
[2] H. Kamata, K. Takahashi, C.U.I. Odenbrand, J. Mol. Catal. A: Chem. 139 (1999) 189.
[3] I.E. Wachs, B.M. Weckhuysen, Appl. Catal. A 157 (1997) 67.
[4] D. Bulushev, F. Rainone, L. Kiwi-Minsker, Langmuir 17 (2001) 5276.
[5] N. Topsøe, H. Topsøe, J. Dumesic, J. Catal. 151 (1995) 226.
[6] P. Overgaard, K. Wieck-Hansen, O. Larsen, Biomass Bioenergy 19 (2000) 395.
[7] G. Busca, G. Centi, L. Marchetti, F. Trifiro, Langmuir 2 (1986) 568.
[8] G.C. Bond, S.F. Tahir, Appl. Catal. 71 (1991) 1.
[9] G. Busca, L. Lietti, G. Ramis, F. Berti, Appl. Catal. B 18 (1998) 1.
[10] J.R. Sohn, J. Ind. Eng. Chem. 10 (2004) 1.
[11] L. Baraket, A. Ghorbel, P. Grange, Appl. Catal. B 72 (2007) 37.
[12] L. Chen, J. Li, M. Ge, J. Phys. Chem. C 113 (2009) 21177.
[13] A. Kustov, M.Y. Kustov, R. Fehrmann, P. Simonsen, Appl. Catal. B 58 (2005) 97.
[14] A. Kustov, S. Rasmussen, R. Fehrmann, P. Simonsen, Appl. Catal. B 76 (2007) 9.
[15] J. Due-Hansen, S. Boghosian, A. Kustov, P. Fristrup, G. Tsilomelekis, K. Ståhl, C.H. Christensen, R. Fehrmann, J. Catal. 251 (2007) 459.
[16] Y. Hari-Bala, J. Zhao, Y. Jiang, X. Ding, Y. Tian, K. Yu, Z. Wang, Mater. Lett. 59 (2005) 1937.
[17] Y. Hari-Bala, J. Zhao, Y. Jiang, X. Ding, Y. Tian, K. Yu, Z. Wang, Mater. Lett. 60 (2006) 494.
[18] A. Kruse, S. Kristensen, A. Riisager, S. Rasmussen, R. Fehrmann, J. Mater. Sci. 44 (2009) 323.
[19] A. Kruse, S. Kristensen, A. Riisager, S. Rasmussen, R. Fehrmann, Patent Application 08169238.6-2104 (DTU), 2008.
[20] W. Stark, K. Wegner, S. Pratsinis, A. Baiker, J. Catal. 197 (2001) 182.
[21] B. Schimmoeller, H. Schulz, S. Pratsinis, A. Bareiss, A. Reitzmann, B. Kraushaar-Czarnetzki, J. Catal. 243 (2006) 82.
[22] L. Yu, X. Zhang, Chem. Phys. 87 (2004) 168.
[23] M. Mohamed, W. Bayoumy, M. Khairy, M. Mousa, Micropor. Mesopor. Mater. 97 (2006) 66.
[24] G. Liu, K. Wang, Z. Zhou, Mater. Sci. Forum 86 (2006) 510.
[25] C. Perego, S. Peratello, Catal. Today 52 (1999) 133.
[26] M. Inomata, A. Mlyamoto, T. Ui, K. Kobayashl, Y. Murakami, Ind. Eng. Chem. Prod. Res. Dev. 21 (1982) 424.
[27] H. Bosch, F. Janssen, Catal. Today 46 (1988) 217.
[28] R.Q. Long, R.T. Yang, J. Catal. 196 (2000) 73.
[29] M. Kanna, S. Wongnawa, Mater. Chem. Phys. 110 (2008) 166.
[30] D.A. Bulushev, L. Kiwi-Minsker, V.I. Zaikovskii, A. Renken, J. Mol. Catal. 193 (2000) 145.
[31] C. Su, B. Hong, C. Tseng, Catal. Today 96 (2004) 119.
[32] T. Akita, K. Tanaka, S. Tsubota, M. Haruta, J. Electron Microsc. 49 (2000) 657.
[33] J.R. Sohn, H.W. Kim, J. Catal. 101 (1986) 428.

[34] O. Saur, M. Bensitel, A.M. Saad, J.C. Lavalley, J. Catal. 99 (1986) 104.
[35] M. Waqif, J. Bachelier, O. Saur, J. Lavalley, J. Mol. Catal. 72 (1992) 127.
[36] S. Samantaray, P. Mohapatra, K.J. Parida, J. Mol. Catal. A 198 (2003) 277.
[37] J.R. Sohn, H.W. Kim, J. Mol. Catal. 52 (1989) 361.
[38] A. Desmartin-Chomel, J.L. Flores, A. Bourane, J.M. Cladens, F. Figueras, G. Delahay, J. Phys. Chem. B 110 (2006) 858.
[39] M. Hino, K. Arata, Mater. Chem. Phys. 26 (1990) 213.
[40] T. Kanougi, T. Atoguchi, S. Yao, J. Mol. Catal. A 177 (2002) 289.
[41] A. Hofmann, J. Sauer, J. Phys. Chem. B 108 (2004) 15679.
[42] G. Busca, Catal. Today 41 (1998) 191.
[43] M. Calatayud, C. Minot, J. Phys. Chem. B 108 (2004) 15679.
[44] A. Vittadini, M. Casarin, A. Selloni, J. Phys. Chem. B 109 (2005) 19560.
[45] S. Soyer, A. Uzun, S. Senkan, I. Onal, Catal. Today 118 (2006) 268.
[46] M. Anstrom, N. Topsøe, J. Dumesic, J. Catal. 213 (2003) 115.
[47] A. Forzatti, P. Nova, I. Beretta, Catal. Today 56 (2000) 431.
[48] G. Went, L. Leu, R.R. Rosin, A.T. Bell, J. Catal. 143 (1992) 492.
[49] D.R. Lide, Handbook of Chemistry and Physics, CRC, 2007.
[50] M. Turco, L. Lisi, R. Pirone, Appl. Catal. B 3 (1994) 133.
[51] N. Topsøe, T. Slabiak, B.S. Clausen, T.Z. Srnak, J.A. Dumesic, J. Catal. 134 (1992) 742.
[52] A.L. Patterson, Phys. Rev. 56 (1939) 978.

**Alternative alkali resistant deNO$_x$ catalysts**

Putluru, S.S.R.; Kristensen, S.B.; Due-Hansen, J.;
Riisager, A.; Fehrmann, R.

*Catal. Today* **2012**, *184*, 192-196

Article

3

# Alternative alkali resistant deNO$_x$ catalysts

Siva Sankar Reddy Putluru, Steffen Buus Kristensen, Johannes Due-Hansen, Anders Riisager, Rasmus Fehrmann*

*Centre for Catalysis and Sustainable Chemistry, Department of Chemistry, Building 207, Technical University of Denmark, DK-2800 Kgs Lyngby, Denmark*

### ARTICLE INFO

### ABSTRACT

Alternative alkali resistant deNO$_x$ catalysts were prepared using three different supports ZrO$_2$, TiO$_2$ and Mordenite zeolite. The majority of the catalysts were prepared by incipient wetness impregnation of a commercial support, with vanadium, copper or iron precursor, one catalyst was prepared by onepot sol–gel method. All catalysts were characterized by BET, XRPD and NH$_3$-TPD. Initial SCR activities of 8 out of 9 catalysts showed higher NO conversion at least at one temperature in the temperature range 300–500 °C compared to the conventional V$_2$O$_5$-WO$_3$/TiO$_2$ catalyst. After potassium poisoning (100–130 µmol of K/g of catalyst) the relative drop in SCR activity and acidity was lower for all the alternative catalysts compared to the industrial V$_2$O$_5$-WO$_3$/TiO$_2$ catalyst. Furthermore, Cu/MOR and Nano-V$_2$O$_5$/Sul-TiO$_2$ catalysts showed 8–16 times higher SCR activities than the conventional even after high potassium doping (250 and 280 µmol of K/g, respectively). The increased poisoning resistance was due to high substrate acidity (sulphated, heteropoly acid promoted and zeolite supports), substituting the active species of the catalyst (other than vanadium species, i.e. Cu, Fe) and new catalyst synthesis methods (Nano-V$_2$O$_5$/Sul-TiO$_2$ catalyst prepared by sol–gel method).

© 2011 Elsevier B.V. All rights reserved.

## 1. Introduction

Nitrogen oxides (NO$_x$) emitted from combustion and high temperature processes have been regarded, during the last three decades, as a major environmental concern. Selective catalytic reduction (SCR) applied to fossil fuel combustion is the best developed and worldwide applied [1,2]. In this process, the NO$_x$ fraction of the flue gas is reduced to nitrogen by ammonia on a catalyst surface. Conventional SCR catalysts are normally composed of V$_2$O$_5$ (the active phase) supported on high surface TiO$_2$. WO$_3$ and MoO$_3$ are the most common compounds added to the catalysts in order to improve its activity and thermal stability. The surface area of the conventional catalysts is around 50–100 m$^2$/g, with a V$_2$O$_5$ content of 0.5–3 wt.% and WO$_3$ or MoO$_3$ loading of 5–10 wt.%. Vanadia, especially as crystallites, is responsible for the undesired oxidation of SO$_2$, hence vanadia content is generally kept low in the presence of high SO$_2$ concentrations [3,4].

The efficiency of conventional state-of-the-art catalyst (V$_2$O$_5$-WO$_3$/TiO$_2$) is high when applied to flue gases from fossil fuels like oil and coal. However, use of biomass (straw, wood, etc.) alone or as co-fuel is of increasing importance since they are part of the carbon eco-cycle on earth, and therefore regarded as sustainable energy source with zero – or at least "neutral" CO$_2$ emissions.

Despite the above mentioned positive effect, biomass combustion introduces several different issues, which may reduce the efficiency of the process and make its operation rather complicated. In particular, the flue gas becomes very poisonous towards the SCR catalyst due to increased content of alkaline potassium salts originating from the biomass combustion. Several authors [5–10] have reported the deactivation effect of alkaline metals on the activity of V$_2$O$_5$/TiO$_2$ catalysts. The majority conclude that poisonous additives (e.g. potassium, barium) are affecting the Brønsted acid sites, which are responsible for the ammonia adsorption, thus decreasing both their number and activity in NO reduction. Relative decrease in catalytic activity after doping with potassium is well correlated with decrease in total acidity of the catalysts [5–10]. Zheng et al. [9] suggested an early mechanism, based on a substitution reaction on the Brønsted acid site, whereby the reactive site is blocked by potassium, as outlined in Eq. (1).

$$\text{V–OH} + \text{KCl} \rightarrow \text{V–O–K} + \text{HCl} \tag{1}$$

This mechanism requires an equimolar ratio of vanadium and potassium to completely deactivate the catalyst. Although the model provides a very intuitive understanding of the deactivation, several groups report of almost complete loss of catalyst activity already at K/V ≈ 0.3–0.5 mol/mol [7,11]. Recent DFT studies suggest a mechanisms in better agreement with experimental findings and show that the poisonous elements preferentially occupy non-atomic hole sites of the (0 1 0) V$_2$O$_5$ surface, thereby inhibiting both Brønsted and V$^{5+}$=O sites [12]. According to this model one

* Corresponding author. Tel.: +45 45252389; fax: +45 45883136.
*E-mail address:* rf@kemi.dtu.dk (R. Fehrmann).

# Appendix C

potassium metal atom can deactivate up to four active vanadium atoms. Lewandowska et al. [13] proposed a model including the alkali effect on the support with atomic ratio of M:V:Ti$_{surface}$ = 1:2:4 using Raman spectroscopy and DFT calculations. The combination of theoretical and experimental studies describes alkali interaction with both the surface vanadium and the support.

The key issue is that the alkaline potassium is blocking the Brønsted V$_2$O$_5$ acid sites of the working SCR catalyst permanently. By now there is no commercial catalyst available for biomass fired flue gas NO$_x$ treatment. This motivates searching for alternative deNO$_x$ catalysts, which are less, affected by alkali salts from the fuel. Several approaches has been applied in the present work to design alkali-resistant catalysts:

1. Increase of substrate acidity, since alkali species would interact stronger with the support than the active vanadia [5,6,14–17].
2. Substituting the active species of the catalyst. A crucial part of the SCR mechanism is the Brønsted acid sites of vanadia, which is much more affected than the Lewis acid sites by potassium doping. Hence, by using metal oxides, which mainly possess Lewis acidity, the catalyst could avoid deactivation by alkali. Cu and Fe are attractive under these conditions, since they are well known Lewis acids and have also exhibited NH$_3$-SCR activity [14,18–21].
3. Improving the activity of the existing V$_2$O$_5$/TiO$_2$ formulation by preparing nano-sized vanadia-particles (being significantly more active than bulk vanadia) on a high surface area TiO$_2$ anatase support. Thereby it is possible to prolong the catalyst time on stream by increasing the amount of initial active sites [22].

In the present work, we have studied alkali resistance of promising SCR catalysts mentioned in the above three classifications. All the catalysts were characterized by various techniques to allow detailed discussion of the SCR performance.

## 2. Experimental

### 2.1. Catalyst preparation and characterization

Various alkali-resistant catalysts were synthesized by different methods. Nano-V$_2$O$_5$/Sul-TiO$_2$ catalyst was prepared by onepot sol–gel method using titanium isopropoxide and vanadium ethoxide as precursors and sulphating with a small amount of H$_2$SO$_4$ [22], Fe/MOR was prepared by ion-exchange method [21] and V$_2$O$_5$-TPA/TiO$_2$ [17], V$_2$O$_5$/Sul-ZrO$_2$ [6], V$_2$O$_5$/MOR [16], Cu-TPA/TiO$_2$, Fe-TPA/TiO$_2$ [19], Cu/MOR [20] catalysts were prepared by incipient wetness impregnation method. Potassium doping was done by incipient wetness impregnation with a solution of KNO$_3$ (Aldrich, 99.99%) to obtain potassium loadings of 100–280 μmol/g of catalyst. Each impregnated catalyst was dried at 120 °C for 12 h followed by calcination at reported temperatures. For the comparison a conventional V$_2$O$_5$-WO$_3$/TiO$_2$ catalyst was also impregnated with potassium.

X-ray powder diffraction (XRPD) measurements were performed on a Huber G670 powder diffractometer using Cu Kα radiation within a 2θ range of 10–80° in steps of 0.02°. BET surface area of the samples was determined from nitrogen physisorption measurements on about 100 mg sample at liquid nitrogen temperature with a Micromeritics ASAP 2010 instrument. Prior to measurements samples were heated to 200 °C for 1 h. NH$_3$-TPD experiments were conducted on a Micromeritics Autochem-II instrument. In a typical TPD experiment, 100 mg of dried sample was placed in a quartz tube and pretreated in flowing He at 200 °C for 2 h. Then, the temperature was lowered to 100 °C and the sample was treated with anhydrous NH$_3$ gas for one hour (Air Liquide,

1% NH$_3$ in He). After NH$_3$ adsorption, the sample was flushed with He (50 ml/min) for 30 min at 100 °C. Finally, the TPD measurement was carried out by heating the sample from 100 to 600–700 °C (10 °C/min) under a flow of He (25 ml/min).

### 2.2. Catalytic activity measurements

SCR activity measurements were carried out at atmospheric pressure in a fixed-bed quartz reactor loaded with 8–20 mg of fractionized (180–300 μm) catalyst samples positioned between two layers of inert quartz wool. The reactant gas composition was adjusted to 1000 ppm NO, 1100 ppm NH$_3$, 3.5% O$_2$, 2.3% H$_2$O and balance N$_2$ by mixing 1% NO/N$_2$ (±0.1% abs.), 1% NH$_3$/N$_2$ (0.005% abs.), O$_2$ (≥99.95%) and balance N$_2$ (≥99.999%) (Air Liquide) with a total flow of 500 ml/min using Bronkhorst EL-Flow F-201C/D mass-flow controllers. During the experiments the temperature was increased stepwise from 300 °C while the NO and NH$_3$ concentrations were continuously monitored by a Thermo Electron Model 17C chemiluminescence NH$_3$-NO$_x$ gas analyzer. All measurements were recorded after steady state was obtained (approximately after 45–60 min).

The catalytic activity is represented as the first-order rate constant (cm$^3$/g s), since the SCR reaction is known to be first-order with respect to NO under stoichiometric NH$_3$ conditions [23]. The first-order rate constants under plug flow conditions were thus obtained from Eq. (2):

$$k = -\left(\frac{F_{NO}}{m_{cat} \cdot C_{NO}}\right) \ln(1-X) \tag{2}$$

where $F_{NO}$ denotes the molar feed rate of NO (mol/s), $m_{cat}$ the catalyst weight (g), $C_{NO}$ the NO concentration (mol/cm$^3$) in the inlet gas and $X$ the fractional conversion of NO. The catalyst amount was kept sufficient low to secure that the measured conversions were well below 90% at all temperatures.

## 3. Results and discussion

Metal content, K/M molar ratio and N$_2$-BET surface area measurements are summarized in Table 1 for fresh and K-doped catalysts. Optimum metal content (wt.%) varies depending on method of preparation and type of support. On vanadium formulations except Nano-V$_2$O$_5$/Sul-TiO$_2$ and V$_2$O$_5$/MOR all catalysts are loaded with 1.7 wt.% of vanadium. Nano-V$_2$O$_5$/Sul-TiO$_2$ and V$_2$O$_5$/MOR catalysts are loaded with 8.4 and 6.7 wt.% of vanadium, respectively. Even with high content of vanadium, Nano-V$_2$O$_5$/Sul-TiO$_2$ and V$_2$O$_5$/MOR catalysts did not show any crystalline phases (Fig. 1) and only pure support patterns were observed in the XRPD. The most intense crystalline V$_2$O$_5$ phases are expected at 2θ = 20.15°, 26.10° and 31.06°. Moreover, all vanadium catalysts were highly dispersed and well below the V$_2$O$_5$ monolayer surface coverage. To exceed monolayer capacity a surface density above 8 VO$_x$/nm$^2$ is needed [24]. On Cu and Fe catalysts optimum loadings are 3–4 wt.% of the metal regardless of the type of support. Surface areas of the fresh catalysts were measured to be between 68 and 348 m$^2$/g. Among all the catalysts the V$_2$O$_5$-WO$_3$/TiO$_2$ catalyst had the lowest surface area (68 m$^2$/g), while V$_2$O$_5$/MOR catalyst exhibited the highest surface area (348 m$^2$/g). Potassium-doped catalysts showed slight decrease in surface area, possibly due to pore blocking.

The total acidity of the fresh and potassium-doped catalysts were measured with NH$_3$-TPD. The total amount of adsorbed ammonia corresponds to molecular adsorbed ammonia or ammonium ions on Lewis or Brønsted acid sites. Even though the applied technique does not allow distinguishing between Lewis and Brønsted acid sites, it still provides valuable information about changes in acidity of the catalysts due to alkali deactivation. Since

*S.S.R. Putluru et al. / Catalysis Today 184 (2012) 192–196*

**Table 1**
Surface area and NH$_3$-TPD of catalysts.

| Catalyst | Metal content (wt.%)[a] | K/M ratio (mol/mol)[b] | Surface area (m$^2$/g) | | Acidity (μmol/m$^2$) | | $T_{max}$ of NH$_3$ desorption (°C) | |
|---|---|---|---|---|---|---|---|---|
| | | | Fresh | K-doped | Fresh | K-doped | Fresh | K-doped |
| V$_2$O$_5$-WO$_3$/TiO$_2$ | 1.7 | 0.3 | 68 | 63 | 9.64 | 2.55 | 260 | 210 |
| Nano-V$_2$O$_5$/Sul-TiO$_2$ | 8.4 | 0.05 | 159 | 150 | 19.9 | 15 | 349 | 265 |
| V$_2$O$_5$-TPA/TiO$_2$ | 1.7 | 0.3 | 112 | 102 | 7.49 | 4.93 | 416 | 338 |
| V$_2$O$_5$/Sul-ZrO$_2$ | 1.7 | 0.4[c] | 72 | 66 | 7.16 | 4.42 | 390 | 330 |
| V$_2$O$_5$/MOR | 6.7 | 0.076 | 348 | 322 | 4.58 | 4.56 | 410 | 396 |
| Cu-TPA/TiO$_2$ | 3 | 0.21 | 108 | 102 | 6.9 | 5.25 | 386 | 341 |
| Cu/MOR | 4 | 0.16 | 336 | 330 | 5.67 | 4.96 | 580 | 540 |
| Fe-TPA/TiO$_2$ | 3 | 0.19 | 100 | 94 | 6.13 | 5.37 | 412 | 347 |
| Fe/MOR | 3 | 0.19 | 322 | 318 | 5.70 | 5.15 | 463 | 440 |

[a] Metal content with respect to V, Cu or Fe.
[b] Catalysts are doped with 100 μmol K/g.
[c] Catalysts are doped with 130 μmol K/g.

the specific surface areas of the catalysts are ranging from 68 to 348 m$^2$/g, it is not possible to compare the total amount of acid sites directly. Therefore a comparison of normalized acid site density (number of acid sites per m$^2$) is used [15,16].

For fresh and K-doped catalysts the total amount of desorbed ammonia per m$^2$ is listed in Table 1. Among all fresh catalysts Nano-V$_2$O$_5$/Sul-TiO$_2$ catalyst has the highest acid site density of 19.9 μmol/m$^2$ and V$_2$O$_5$/MOR catalyst has the lowest value of 4.58 μmol/m$^2$. The conventional V$_2$O$_5$-WO$_3$/TiO$_2$ catalyst showed acid site density of 9.64 μmol/m$^2$. Potassium-doped catalysts showed a lower acid site density compared to the fresh catalysts. The decrease of acid sites is due to occupation of potassium on the strongest acid sites, which could possible decrease the strength of the remaining acid sites through electron donation. Among all the potassium deactivated catalysts K-V$_2$O$_5$-WO$_3$/TiO$_2$ has the lowest acid site density of 2.6 μmol/m$^2$ and Nano-V$_2$O$_5$/Sul-TiO$_2$ catalyst has still a higher acid site density, i.e. 15.0 μmol/m$^2$ after doping with potassium. Especially K-V$_2$O$_5$-WO$_3$/TiO$_2$ catalyst showed an acidity drop of 61% and alternative catalysts showed moderate loss of 2–42% upon potassium-doping. The difference in relative change of acidity (%) might be due to partly coordination of K$_2$O to the active metal (V or Cu or Fe) along with interaction with promoters and support. On the K-V$_2$O$_5$-WO$_3$/TiO$_2$ catalyst, potassium seems to coordinate preferably to the vanadium sites making them inactive for NH$_3$ adsorption, while alternative catalysts host the potassium on dense acid sites of the support with less acidity drop.

The NH$_3$-TPD measurements also provide useful information about the strength of the acid sites. The relative strength of the

acid sites are reflected by the temperature of maximum ammonia desorption as listed in Table 1. Among all fresh catalysts the Cu/MOR catalyst has the highest acid strength (580 °C) and V$_2$O$_5$-WO$_3$/TiO$_2$ catalyst has the lowest value (260 °C). The acid strength of the fresh catalysts follows the order: Cu/MOR > Fe/MOR > V$_2$O$_5$-TPA/TiO$_2$ > Fe-TPA/TiO$_2$ > V$_2$O$_5$/MOR > V$_2$O$_5$/Sul-ZrO$_2$ > Nano-V$_2$O$_5$/Sul-TiO$_2$ > V$_2$O$_5$-WO$_3$/TiO$_2$. All the potassium-doped catalysts showed a lower acid strength compared to the fresh catalysts. Among all the potassium deactivated catalysts K-V$_2$O$_5$-WO$_3$/TiO$_2$ has the lowest acid strength (210 °C) and Cu/MOR catalyst has still the highest acid strength (540 °C), after doping with potassium. Overall, the alternative catalysts showed high acid strength compared to the V$_2$O$_5$-WO$_3$/TiO$_2$ catalyst.

The SCR activity of the fresh catalysts was measured in the temperature range 300–500 °C. In Fig. 2 the measured catalytic activities are reported as first-order rate constants $k$ (cm$^3$/g s). The catalytic activity is generally increasing with catalyst temperature until an optimum temperature is reached between 350 and 500 °C. Upon further increase in temperature the SCR activity decreases due to predominant ammonia oxidation [25,26]. Generally, SCR catalysts can be broadly classified based on operating temperature as; low temperature (150–300 °C), medium temperature (260–425 °C) and high temperature catalysts (345–590 °C) [26]. Low temperature formulations are Mn and Pt-based catalysts, medium temperature catalysts are Cu and V$_2$O$_5$ based and high temperature catalysts are Fe based [2,26,27]. In majority of the cases medium temperature SCR catalysts are *chosen* because of the sulphur tolerance, selectivity and design options in the power plant.

Cu-TPA/TiO$_2$, Nano-V$_2$O$_5$/Sul-TiO$_2$, V$_2$O$_5$-WO$_3$/TiO$_2$, V$_2$O$_5$/Sul-ZrO$_2$, V$_2$O$_5$-TPA/TiO$_2$, Fe-TPA/TiO$_2$, V$_2$O$_5$/MOR and Fe/MOR catalysts showed SCR $T_{max}$ performance at 400, 420, 421, 425, 440, 460, 480, 500 and 500 °C, respectively. Based on $T_{max}$ performance the catalysts could be classified as medium temperature (Cu-TPA/TiO$_2$, V$_2$O$_5$-WO$_3$/TiO$_2$, Nano-V$_2$O$_5$/Sul-TiO$_2$, Cu/MOR, V$_2$O$_5$/Sul-ZrO$_2$ and V$_2$O$_5$-TPA/TiO$_2$) and high temperature (Fe-TPA/TiO$_2$, V$_2$O$_5$/MOR and Fe/MOR) SCR catalysts. Overall Cu/MOR, Nano-V$_2$O$_5$/Sul-TiO$_2$, Fe/MOR, V$_2$O$_5$/MOR, V$_2$O$_5$-TPA/TiO$_2$, V$_2$O$_5$-WO$_3$/TiO$_2$, Fe-TPA/TiO$_2$, V$_2$O$_5$/Sul-ZrO$_2$ and Cu-TPA/TiO$_2$ catalysts showed maximum rate constant ($k_{max}$) values of 2542, 2008, 1550, 1052, 965, 908, 810, 645 and 616 cm$^3$/g s, respectively, at their $T_{max}$ operating temperatures. At $T_{max}$ temperatures, the analogous conversion values are 84, 75, 85, 87, 76, 86, 73 and 77% using 8–20 mg of catalyst. The rate constants observed for Cu/MOR, Nano-V$_2$O$_5$/Sul-TiO$_2$, Fe/MOR, V$_2$O$_5$/MOR, V$_2$O$_5$-TPA/TiO$_2$ catalysts are higher than those for the conventional V$_2$O$_5$-WO$_3$/TiO$_2$ catalyst. Previous studies on the effect of sulphation, acidified supports with promoters and zeolites showed enhanced SCR activity, increasing the activity up to 50% compared with that of the conventional V$_2$O$_5$-WO$_3$/TiO$_2$ catalyst [5,6]. Especially, Cu/MOR and
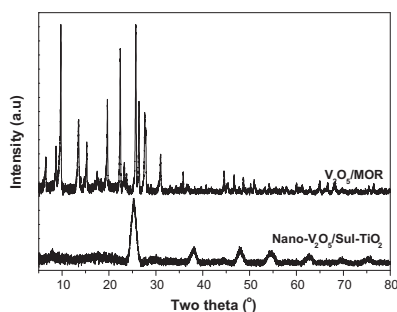


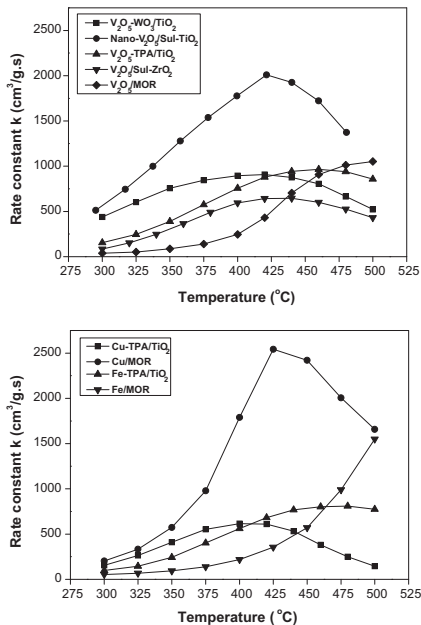**Fig. 1.** XRPD patterns of V$_2$O$_5$/MOR and Nano-V$_2$O$_5$/Sul-TiO$_2$ catalysts.

**Fig. 2.** Temperature dependency of first-order rate constant for SCR of NO with fresh catalysts. Reaction conditions: 1000 ppm NO, 1100 ppm $NH_3$, 3.5% $O_2$, 2.3% $H_2O$, balance $N_2$.
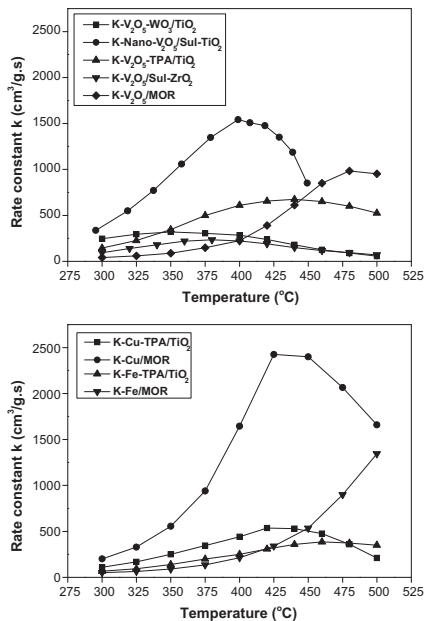


**Fig. 3.** Temperature dependency of first-order rate constant for SCR of NO with K-doped catalysts. Reaction conditions: 1000 ppm NO, 1100 ppm $NH_3$, 3.5% $O_2$, 2.3% $H_2O$, balance $N_2$.

Nano-$V_2O_5$/Sul-$TiO_2$ catalysts could be used at same temperature as the conventional $V_2O_5$-$WO_3$/$TiO_2$ catalyst, which could further indicate that these alternative catalysts are easily replaceable in the existing power plants. Hence comparison with the rate constant and $T_{max}$ performance gives clear idea about the potential ability of the alternative catalysts for SCR of NO.

The SCR activity of the potassium-doped catalysts was measured in the temperature range 300–500 °C (Fig. 3). K-$V_2O_5$-$WO_3$/$TiO_2$, K-Nano-$V_2O_5$/Sul-$TiO_2$, K-$V_2O_5$/Sul-$ZrO_2$, K-$V_2O_5$-TPA/$TiO_2$, K-Fe-TPA/$TiO_2$ and K-$V_2O_5$/MOR catalysts showed lower $T_{max}$ (order of 20–40 °C less compared to fresh catalysts) and that of K-Cu/MOR, K-Fe/MOR catalysts showed similar $T_{max}$ whereas K-Cu-TPA/$TiO_2$ catalyst showed high $T_{max}$ compared to the fresh catalyst. A possible explanation for such a temperature shift is that the potassium loading reduced the activity of the main NO-SCR reaction while the rate of side reaction of ammonia oxidation remained constant or even increased. Potassium poisoned catalysts also showed decreased SCR activity. K-Cu/MOR, K-Nano-$V_2O_5$/Sul-$TiO_2$, K-Fe/MOR, K-$V_2O_5$/MOR, K-$V_2O_5$-TPA/$TiO_2$, K-Cu-TPA/$TiO_2$, K-Fe-TPA/$TiO_2$, K-$V_2O_5$-$WO_3$/$TiO_2$, and K-$V_2O_5$/Sul-$ZrO_2$ catalysts showed maximum rate constant ($k_{max}$) values of 2425, 1542, 1345, 983, 675, 537, 385, 320 and 235 $cm^3$/g s, respectively, at their $T_{max}$ operating temperatures.

The decrease in activity after doping with 100–130 μmol potassium/g catalyst is represented as relative activity (%) (Fig. 4) at 400 °C, which is a normal operation temperature in commercial stationary SCR units. Among all the catalysts $V_2O_5$-$WO_3$/$TiO_2$ catalyst possessed a relative activity of 31.8%, whereas Fe/MOR, Cu/MOR,

$V_2O_5$/MOR, Nano-$V_2O_5$/Sul-$TiO_2$, $V_2O_5$-TPA/$TiO_2$, Cu-TPA/$TiO_2$, Fe-TPA/$TiO_2$ and $V_2O_5$/Sul-$ZrO_2$ catalysts showed 97.7, 92, 90.9, 86.8, 80.7, 71.8, 44.6 and 37%, respectively. Notably, these relative activity values are significantly higher compared to those of conventional $V_2O_5$-$WO_3$/$TiO_2$ SCR catalysts.

The catalytic activity of potential catalysts (i.e. $V_2O_5$-$WO_3$/$TiO_2$, Cu/MOR and Nano-$V_2O_5$/Sul-$TiO_2$) at 400 °C with 280 μmole potassium/g of catalyst is shown in Fig. 5. By increasing the potassium concentration a further decrease in the catalytic activity was observed. The initial activity of the catalysts at 400 °C
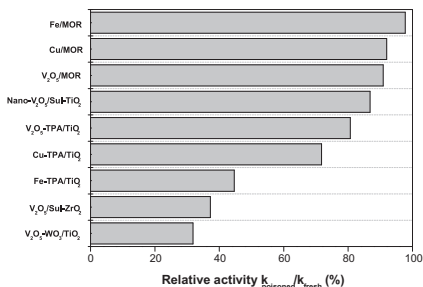


**Fig. 4.** Relative activity of the catalysts at 400 °C with the potassium concentration values mentioned in Table 1.
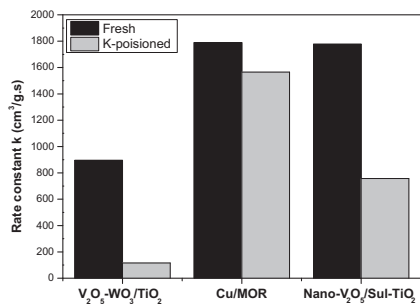
**Fig. 5.** Rate constant values of potential catalysts with high potassium concentration at 400 °C. $V_2O_5$-$WO_3$/$TiO_2$, Cu/MOR catalysts are doped with 250 $\mu$mol K/g and Nano-$V_2O_5$/Sul-$TiO_2$ catalyst doped with 280 $\mu$mol K/g.

were in decreasing order, Cu/MOR (1789 cm$^3$/g s) > Nano-$V_2O_5$/Sul-$TiO_2$ (1777 cm$^3$/g s) > $V_2O_5$-$WO_3$/$TiO_2$ (895 cm$^3$/g s). After doping with potassium the former catalysts performed surprisingly good (Cu/MOR, 1565 cm$^3$/g s and Nano-$V_2O_5$/Sul-$TiO_2$, 757 cm$^3$/g s) while the conventional performed rather poor ($V_2O_5$-$WO_3$/$TiO_2$, 116 cm$^3$/g s).

Overall characterization and SCR results reveal that all catalysts showed high SCR activity and appreciable acidity site density in comparison with conventional $V_2O_5$-$WO_3$/$TiO_2$. Potassium doped $V_2O_5$-$WO_3$/$TiO_2$ catalyst showed little decrease in surface area but substantial loss of acidity site density and SCR activity. The alternative deNO$_x$ catalysts showed a slight decrease of acidity and SCR activity after potassium doping. Among the alternative deNO$_x$ catalysts Cu/MOR and Nano-$V_2O_5$/Sul-$TiO_2$ catalysts maintained high initial activity and superior alkali resistivity compared to that of conventional $V_2O_5$-$WO_3$/$TiO_2$ catalyst.

## 4. Conclusions

The developed SCR deNO$_x$ catalysts are attractive alternatives to conventional state of the art catalysts due to higher activities and higher potassium resistance. Depending on the conditions like pure biomass combustion/biomass and coal co-combustion or medium/high temperature it is possible to select the alternative catalysts for the particular flue gas cleaning demand. We believe that these results provide new insight for further development of alkali resistant deNO$_x$ catalysts for use in biomass fired stationary sources.

## References

[1] H. Bosch, F. Janssen, Catal. Today 2 (1988) 369.
[2] V.I. Pârvulescu, P. Grange, B. Delmon, Catal. Today 46 (1998) 233.
[3] P. Forzatti, Appl. Catal. A 222 (2001) 221–236.
[4] J.P. Dunn, P.R. Koppula, H.G. Stenger, I.E. Wachs, Appl. Catal. B 19 (1998) 103.
[5] A.L. Kustov, M.Yu. Kustova, R. Fehrmann, P. Simonsen, Appl. Catal. B 58 (2005) 97.
[6] J. Due-Hansen, S. Boghosian, A. Kustov, P. Fristrup, G. Tsilomelekis, K. Ståhl, C.H. Christensen, R. Fehrmann, J. Catal. 251 (2007) 459.
[7] J. Chen, R. Yang, J. Catal. 125 (1990) 411.
[8] L. Lisi, G. Lasorella, S. Malloggi, G. Russo, Appl. Catal. B 50 (2004) 251.
[9] Y. Zheng, A.D. Jensen, J.E. Johnsson, Ind. Eng. Chem. Res. 43 (2004) 941.
[10] H. Kamata, K. Takahashi, C.I. Odenbrand, J. Mol. Catal. A: Chem. 139 (1999) 189.
[11] R. Khodayari, C.U.I. Odenbrand, Appl. Catal. B 30 (2001) 87.
[12] D. Nicosia, I. Czekaj, O. Kröcher, Appl. Catal. B 77 (2008) 228.
[13] A.E. Lewandowska, M. Calatayud, E. Lozano-Diz, C. Minot, M.A. Bañares, Catal. Today 139 (2008) 209.
[14] A.L. Kustov, S.B. Rasmussen, R. Fehrmann, P. Simonsen, Appl. Catal. B 76 (2007) 9.
[15] J. Due-Hansen, A.L. Kustov, S.B. Rasmussen, R. Fehrmann, C.H. Christensen, Appl. Catal. B 66 (2006) 161.
[16] S.S.R. Putluru, A. Riisager, R. Fehrmann, Appl. Catal. B 97 (2010) 333.
[17] S.S.R. Putluru, A.D. Jensen, A. Riisager, R. Fehrmann, Catal. Sci. Technol. 1 (2011) 631.
[18] G. Busca, L. Lietti, G. Ramis, F. Berti, Appl. Catal. B 18 (1998) 1.
[19] S.S.R. Putluru, S. Mossin, A. Riisager, R. Fehrmann, Catal. Today 176 (2011) 292.
[20] S.S.R. Putluru, A. Riisager, R. Fehrmann, Appl. Catal. B 101 (2011) 183.
[21] S.S.R. Putluru, A.D. Jensen, A. Riisager, R. Fehrmann, 14th Nordic Symposium on Catalysis, Marienlyst, Denmark, August, 2010.
[22] A.J. Kruse, S.B. Kristensen, A. Riisager, S.B. Rasmussen, R. Fehrmann, J. Mater. Sci. 44 (2009) 323.
[23] R.Q. Long, R.T. Yang, J. Catal. 196 (2000) 73.
[24] H. Tian, E.I. Ross, I.E. Wachs, J. Phys. Chem. B 110 (2006) 9593.
[25] G. Ramis, L. Yi, G. Busca, M. Turco, E. Kotur, R.J. Willey, J. Catal. 157 (1995) 523.
[26] R.M. Heck, Catal. Today 53 (1999) 519.
[27] S. Roy, M.S. Hegde, G. Madras, Appl. Energy 86 (2009) 2283.

.